Nanoscale

PAPER

View Article Online
View Journal | View Issue

Cite this: *Nanoscale*, 2022, **14**, 10176

Rational design of amphiphilic fluorinated peptides: evaluation of self-assembly properties and hydrogel formation†

Suvrat Chowdhary,[a] Robert Franz Schmidt,[b] Anil Kumar Sahoo,[c,d] Tiemo tom Dieck,[a] Thomas Hohmann,[a] Boris Schade,[e] Kerstin Brademann-Jock,[f] Andreas F. Thünemann,[f] Roland R. Netz,[c] Michael Gradzielski[b] and Beate Koksch*[a]

Advanced peptide-based nanomaterials composed of self-assembling peptides (SAPs) are of emerging interest in pharmaceutical and biomedical applications. The introduction of fluorine into peptides, in fact, offers unique opportunities to tune their biophysical properties and intermolecular interactions. In particular, the degree of fluorination plays a crucial role in peptide engineering as it can be used to control the characteristics of fluorine-specific interactions and, thus, peptide conformation and self-assembly. Here, we designed and explored a series of amphipathic peptides by incorporating the fluorinated amino acids (2*S*)-4-monofluoroethylglycine (**MfeGly**), (2*S*)-4,4-difluoroethylglycine (**DfeGly**) and (2*S*)-4,4,4-trifluoroethylglycine (**TfeGly**) as hydrophobic components. This approach enabled studying the impact of fluorination on secondary structure formation and peptide self-assembly on a systematic basis. We show that the interplay between polarity and hydrophobicity, both induced differentially by varying degrees of side chain fluorination, does affect peptide folding significantly. A greater degree of fluorination promotes peptide fibrillation and subsequent formation of physical hydrogels in physiological conditions. Molecular simulations revealed the key role played by electrostatically driven intra-chain and inter-chain contact pairs that are modulated by side chain fluorination and give insights into the different self-organization behaviour of selected peptides. Our study provides a systematic report about the distinct features of fluorinated oligomeric peptides with potential applications as peptide-based biomaterials.

Received 25th March 2022,
Accepted 21st June 2022

DOI: 10.1039/d2nr01648f

rsc.li/nanoscale

Introduction

Self-assembling peptides (SAPs) are often composed of an amphiphilic structure motif based on alternating arrangements of hydrophobic and hydrophilic residues.[1–4] More than two decades ago the first and most prominent variants **EAK16-II** H_2N-(Ala–Glu–Ala–Glu–Ala–Lys–Ala–Lys)$_2$-OH and **RADA16-II** H_2N-(Arg–Ala–Arg–Ala–Asp–Ala–Asp–Ala)$_2$-OH were discovered by Zhang *et al.*[5] These peptides served as essential motifs to study the hierarchical construction of β-sheet-based macroassemblies.[2,5–8] Since then, SAPs have attracted paramount interest in biomedical research for their biocompatibility, biodegradability, and biofunctionality. They were utilized in the field of tissue engineering by functioning as extracellular matrix mimics for cell proliferation and wound healing.[9–14] Their self-assembly is driven by non-covalent interactions such as hydrogen bonding, electrostatic interactions, hydrophobic interactions, aromatic interactions (π–π stacking) and van der Waals forces.[15–18] A promising approach to produce novel functional peptide-based biomaterials consists of the systematic incorporation of fluorinated amino acids. These non-natural building blocks turned out to be a powerful tool to fine-tune biophysical and chemical properties of peptides and proteins.[19] Fluorine possesses unique properties including a strong inductive effect combined with high electronegativity. The replacement of a single C–H bond with C–F is generally

[a]*Institute of Chemistry and Biochemistry, Freie Universität Berlin, Arnimallee 20, 14195 Berlin, Germany. E-mail: beate.koksch@fu-berlin.de*
[b]*Institute of Chemistry, Technische Universität Berlin, Straße des 17. Juni 124, 10623 Berlin, Germany*
[c]*Department of Physics, Freie Universität Berlin, Arnimallee 14, 14195 Berlin, Germany*
[d]*Max Planck Institute of Colloids and Interfaces, Am Mühlenberg 1, 14476 Potsdam, Germany*
[e]*Institute of Chemistry and Biochemistry and Core Facility BioSupraMol, Freie Universität Berlin, Fabeckstraße 36a, 14195 Berlin, Germany*
[f]*Federal Institute for Materials Research and Testing (BAM), Unter den Eichen 87, 12205 Berlin, Germany*
† Electronic supplementary information (ESI) available. See DOI: https://doi.org/10.1039/d2nr01648f

considered to be isosteric.[20,21] Investigations of the effects of fluorinated amino acids on hydrophobicity,[22,23] secondary structure formation,[24,25] protein–protein interactions,[26,27] amyloid folding kinetics,[28,29] proteolytic stability,[30] the chemical and biological properties of fluorinated peptide-based materials,[31] and the integration of fluorine into bacteria[32,33] have been reported by our group. The vast majority of previous studies including our own efforts examining fluorinated amino acids in the context of peptide and protein chemistry were limited to the incorporation of one or only a few of these building blocks. Moreover, the chemical nature and biological features of polyfluorinated peptides with a large proportion of fluorinated aliphatic amino acids have not yet been studied. Thus, we were motivated to address the question of the impact that several of such building blocks would have on fluorine-specific interactions in peptide self-assembly.

The fabrication of polyfluorinated peptides obviously requires generous amounts of fluorinated amino acids.[34] Thus, we have recently reported an improved synthetic strategy to obtain the fluorinated amino acid (2*S*)-4-monofluoroethylglycine (**MfeGly**) at the gram scale.[35] Moreover, Soloshonok *et al.* developed a general and practical synthetic process to obtain enantiomerically pure Fmoc-protected fluorinated amino acid through an asymmetric and Ni(II)-complex mediated stereoselective synthesis (see Scheme S1 in the ESI†).[36–39] In current attempts, we have extended this strategy to the synthesis of a diverse range of aliphatic fluorinated amino acids with different side chain patterns.[40]

In this work, we designed an amphipathic motif including lysine and the well-studied non-proteogenic amino acid α-aminobutyric acid (**Abu**), which has been reported as a suitable hydrophobic building block for SAPs.[41,42] The varying degree of fluorination was adjusted by the iterative incorporation of its derivatives (2*S*)-4-monofluoroethylglycine (**MfeGly**), (2*S*)-4,4-difluoroethylglycine (**DfeGly**) and (2*S*)-4,4,4-trifluoroethylglycine (**TfeGly**). With this peptide library we assessed the impact of fluorine-specific interactions on the intrinsic hydrophobicity, secondary structure formation, self-assembling properties, the morphology of amyloid-like aggregates and the formation of peptide hydrogels. Molecular simulations of the different fluorinated peptides demonstrate that the peptide–peptide interactions are finely tuned by the ability of fluorine atoms to form electrostatic contact pairs with positively partially charged atoms on the backbone and side chains. This ability in turn depends critically on the number of fluorinated substituents, based on which we explain how the fluorination degree controls peptide structure formation.

Results and discussion

Peptide design: estimation of sequence length, hydrophobicity, and fluorine-induced polarity

Our rational design is based on a cationic Abu–Lys repeating unit. A π-system derived from 4-aminobenzoic acid (**[4]Abz**, PABA) was placed on the C-terminus; this building block is a widely used fluorescent probe and enables precise control over peptide stock concentrations.[43] To determine a chain length sufficient for β-sheet formation, we characterized a series of **AbuK**-derived peptides with repeating units ranging from five to eight alternating residues and studied their ability to form secondary structures under physiological conditions *via* CD spectroscopy (Fig. 1a). High peptide concentrations (2 wt%) were chosen to induce peptide self-assembly. As can be seen from the CD spectra, only **AbuK14** (Ac-(Abu–Lys)$_7$-**[4]Abz**-NH$_2$) and **AbuK16** (Ac-(Abu–Lys)$_8$-**[4]Abz**-NH$_2$) formed β-sheet structures (λ_{min} = 214–220 nm), whereas the remaining variants (**AbuK10–13**, **AbuK15**) tend to form polyproline type II helices (PPII). This is proven by the characteristic positive and negative maxima at λ_{max} = 218–228 nm and λ_{min} = 198–205 nm. The PPII helix comprises an extended left-handed helical structure and was also found for similar Ala–Lys derived SAPs.[44,45] A further minimum at λ_{min} = 228–230 nm could hint for a minor population of β-turn like conformations through intramolecular hydrophobic interactions between the **Abu** residues.[46,47] As the 16-meric **AbuK16** was shown to form β-sheets, we synthesized the polyfluorinated amphipathic peptides **MfeGlyK16** (Ac-(MfeGly-Lys)$_8$-**[4]Abz**-NH$_2$), **DfeGlyK16** (Ac-(DfeGly-Lys)$_8$-**[4]Abz**-NH$_2$) and **TfeGlyK16** (Ac-(TfeGly-Lys)$_8$-**[4]Abz**-NH$_2$) by substitution of **Abu** with each fluorinated derivative according to the eight repeating unit pattern (Fig. 1b).

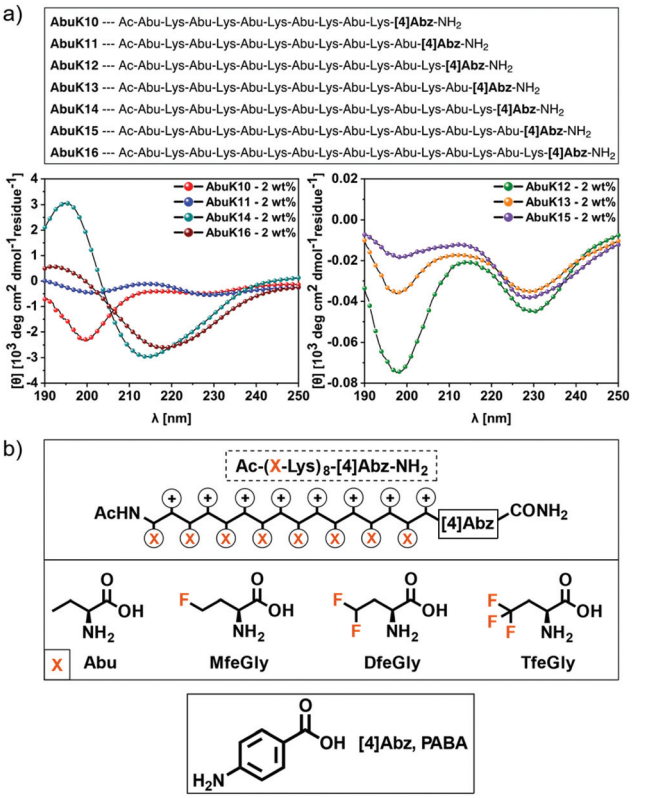

Fig. 1 (a) CD spectra of 2 wt% **AbuK10–AbuK16** in 50 mM Bis-tris propane + 150 mM NaCl, pH 7.4 recorded at 37 °C. (b) Peptide motif (**AbuK16**, **MfeGlyK16**, **DfeGlyK16**, **TfeGlyK16**) and chemical structures of **Abu** and its derivatives **MfeGly**, **DfeGly** and **TfeGly** as well was **[4]Abz**.

Rational design applying fluorinated amino acids in peptide scaffolds crucially depends on a reliable determination of their hydrophobic nature. Estimation of the intrinsic hydrophobicity is indispensable to discuss fluorine-specific interactions for each oligopeptide. In this work, the hydrophobic properties of peptides were determined through a RP-HPLC based assay (Fig. 2a). In general, the hydrophobicity of the peptides increases with the number of fluorine substituents on the individual amino acids. However, **MfeGlyK16** is more polar than **AbuK14** and **AbuK16**, which is in accordance with prior observed trends in fluorine-induced hydrophobicity with this particular amino acid series.[28,48] We thus conclude that the origin of the decrease in non-polar character of **MfeGlyK16** lies rather in the physicochemical properties of its side chain than in its overall fluorine content.

a)

Peptide	Retention time ϱ [min]
AbuK14	(15.333 ± 0.0173)
MfeGlyK16	(15.285 ± 0.075)
AbuK16	(16.368 ± 0.087)
DfeGlyK16	(18.780 ± 0.044)
TfeGlyK16	(23.054 ± 0.031)

b)

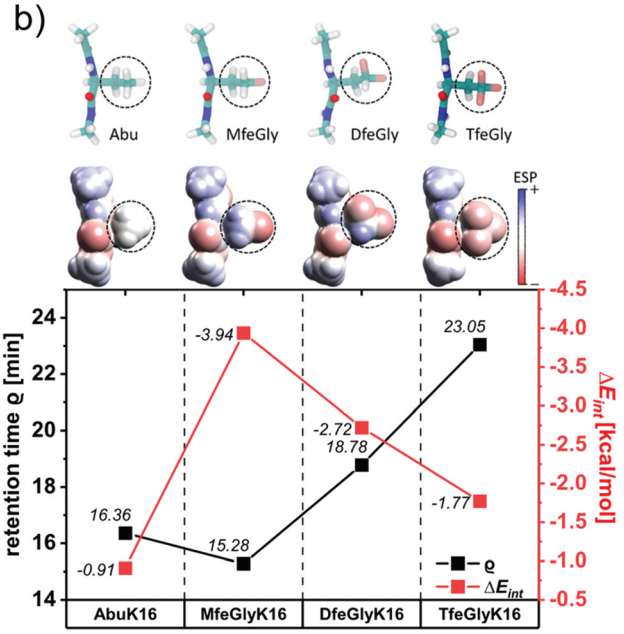

Fig. 2 (a) Retention times ϱ of **AbuK14**, **AbuK16**, **MfeGlyK16**, **DfeGlyK16** and **TfeGlyK16** as experimental index of intrinsic hydrophobicity. An increase in ϱ corresponds to an enhanced non-polar character of respective peptide. The eluents were (A) H_2O + 0.1% (v/v) TFA and (B) ACN + 0.1% (v/v) TFA by applying a gradient of 5% → 40% (B) over 30 min. (b) Geometry optimized structures of different amino acid residues marked with dashed circles with the N-terminal acetyl cap and the C-terminal *N*-methylamide cap obtained from quantum mechanical (MP2/6-31G*) calculations are shown in the ball-stick representation (top row). Atoms are colored according to atom types: carbon (cyan), nitrogen (blue), oxygen (red), hydrogen (white), and fluorine (pink). The corresponding space-filling models are colored according to the calculated electrostatic potential (ESP) showing the varying polarities for the different side chains. The calculated interaction energies ΔE_{int} (HF/6-31G*) of water with an **Abu**, **MfeGly**, **DfeGly** and **TfeGly** side chain are plotted against retention times ϱ of **AbuK16**, **MfeGlyK16**, **DfeGlyK16** and **TfeGlyK16**. For comparison, we also calculated the change in ΔE_{int} for water–water interactions (−5.85 kcal mol^{-1}).

Theoretical approaches to determining the hydrophobic nature of fluorinated amino acids emphasized a change in apparent non-polar character through side chain-based interactions in aqueous conditions triggered by fluorination.[49] To gain deeper insights into the impact of fluorine-specific interactions, we used quantum mechanical (QM) calculations for the residues of **Abu**, **MfeGly**, **DfeGly** and **TfeGly**-derived motifs. The QM geometry optimized structures, their electrostatic potential (ESP) maps and water interaction energies ΔE_{int} for the different types of amino acids are shown in Fig. 2b. The ESP maps reveal different degrees of side chain polarities, the lowest for **Abu** and the highest for **MfeGly**. Interestingly, with further increase in fluorination (**DfeGly**, **TfeGly**), the polarity decreases again. To quantify the hydrophobicity of the side chains, we calculated ΔE_{int} for the different types of amino acids by many initial configurations of an amino acid–water complex for each amino acid type. ΔE_{int} is found to be the smallest for **Abu** (−0.91 kcal mol^{-1}) and the largest for **MfeGly** (−3.94 kcal mol^{-1}). Like the side chain polarity, ΔE_{int} decreases with further increase of fluorination: **DfeGly** (−2.72 kcal mol^{-1}) and **TfeGly** (−1.77 kcal mol^{-1}). It should be noted that these ΔE_{int} values are smaller than the water–water interaction energy of −5.85 kcal mol^{-1}, which implies that all these amino acids are hydrophobic. The theoretical values corroborate the experimental trends of peptide hydrophobicity, emphasizing the impact of fluorine-induced polarity changes as seen for **MfeGlyK16**.

Secondary structure formation of amphipathic peptides

All oligopeptides were studied over a wide concentration range (0.1–1 wt%) by means of CD spectroscopy (Fig. 3). Secondary structure formation was investigated under physiologically buffered (pH 7.4) and basic (pH 9.0) conditions. The results at pH 7.4 show for **AbuK16** and **MfeGlyK16** at concentrations of 0.1–1 wt% (Fig. 3a–d) the typical course of absorption of a PPII-like conformation as discussed for **AbuK**-derived peptides above. Interestingly, the formation of β-sheets was not observed for **MfeGlyK16** at the highest concentration of 2 wt% (Fig. 3d), very different from the observations for **AbuK14** and **AbuK16** (see Fig. 1a). Increasing the degree of fluorination triggers β-sheet formation (≥0.25 wt%) for **DfeGlyK16**; for lower concentrations (0.1 wt%) a similar conformation as given for **AbuK16** and **MfeGlyK16** was observed (Fig. 3a–d). A growth in fluorine-content on each individual amino acid increases the hydrophobic nature while, simultaneously, decreasing the polarity and, therefore, promotes β-sheet formation. In this manner, the most fluorinated peptide **TfeGlyK16** was found to form β-sheets at all selected concentrations (Fig. 3a–d).

We further studied these peptides under basic conditions (pH 9.0) (Fig. 3e and f) that promote neutralization of the formal positive charges and, thus, induce β-sheet formation.

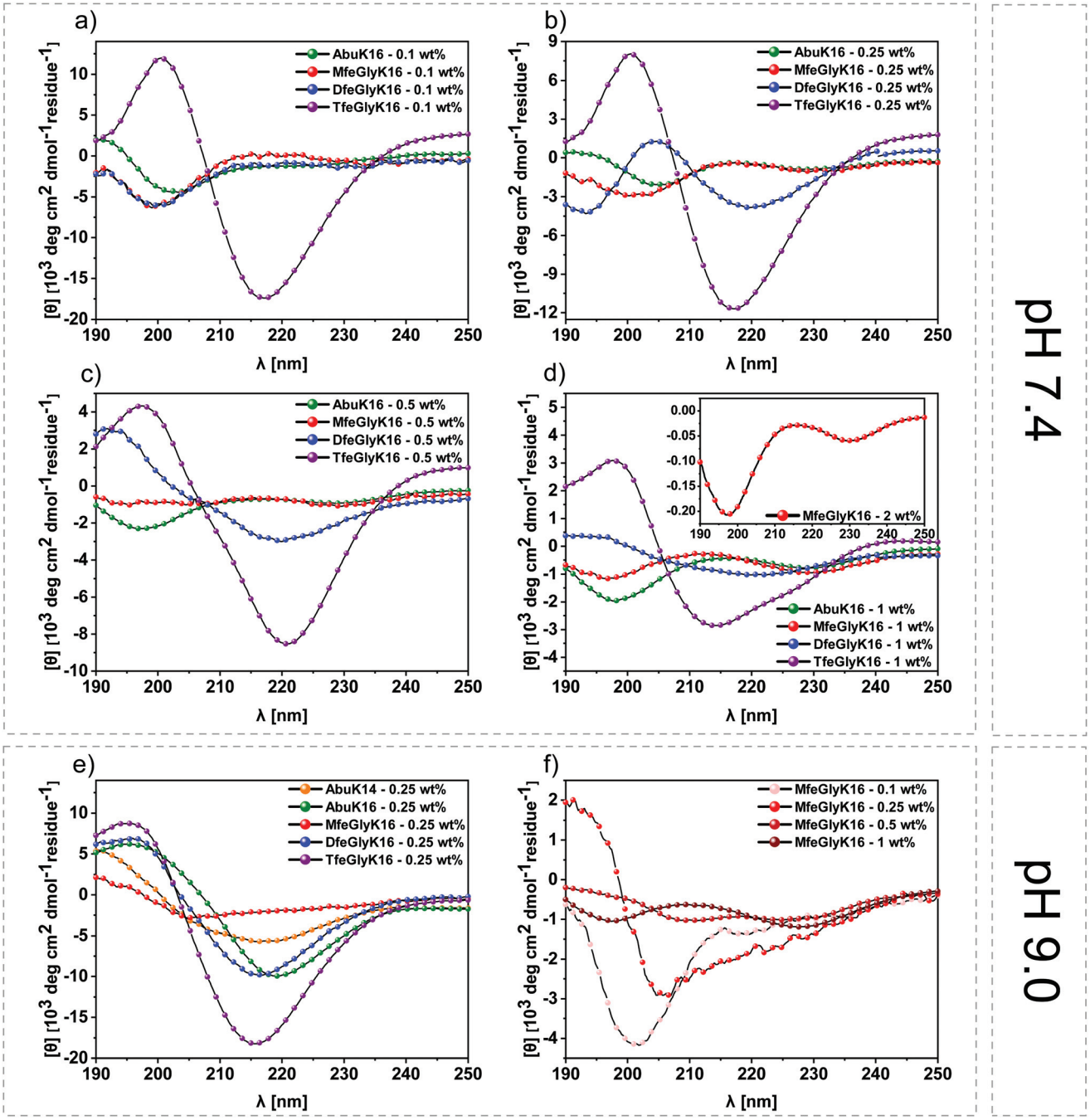

Fig. 3 CD spectra of amphipathic oligopeptides **AbuK16** (green), **MfeGlyK16** (red), **DfeGlyK16** (blue) and **TfeGlyK16** (violet) at (a) 0.1 wt%, (b) 0.25 wt%, (c) 0.5 wt% & (d) 1 wt% (also 2 wt% for **MfeGlyK16**) concentration in 50 mM Bis-tris propane + 150 mM NaCl, pH 7.4 recorded at 37 °C. CD spectra of (e) 0.25 wt% amphipathic oligopeptides **AbuK14**, **AbuK16**, **MfeGlyK16**, **DfeGlyK16** and **TfeGlyK16** and (f) 0.1–1 wt% **MfeGlyK16** in 50 mM Bis-tris propane + 150 mM NaCl, pH 9.0 recorded at 37 °C.

All peptides undergo β-sheet formation at a concentration of 0.25 wt%. Peptides **AbuK14** and **AbuK16** form β-sheets at indicated concentrations at pH 9.0, whereas significantly higher concentrations are necessary under physiological conditions (2 wt%). The only exception in this regard is the variant **MfeGlyK16**, which does not form β-sheets even at higher concentrations of 1 wt% (see Fig. 3f). Comparison of **MfeGlyK16** with **AbuK14**, both possessing similar values of peptide hydrophobicity, underlines the lack of β-sheet assembly for **MfeGlyK16** due to its side chain properties. Likewise, calculated ΔE_{int} values suggests the residue of **MfeGly** to be better accommodated in a water-exposed environment. We propose this circumstance, phenomenologically, as a notable driving force maintaining **MfeGlyK16** in a PPII-like conformation.

Beside the polar effects of each fluorinated side chain, their intrinsic secondary structure propensities are also crucial factors to understand fluorine-driven peptide folding. As reported by Gerling *et al.* the **MfeGly** side chain possesses the highest helical propensity among its fluorinated derivatives **DfeGly** and **TfeGly**.[28] In correlation with the CD data, we suggest a synergistic effect of intrinsic folding propensity and fluorine-induced polarity by multiple incorporation of **MfeGly** causing the folding pattern of **MfeGlyK16**. For this purpose, we executed MD simulations to further elucidate this experimental finding. These theoretical results are discussed below.

Peptide self-assembly and characterization of fluorinated peptide-based hydrogels

Earlier reports demonstrated the supramolecular assemblies of amphipathic peptides to possess similar properties as the cross-β-sheet structure of amyloid fibrils.[50,51] In order to study structural features of these peptides we used thioflavin T (ThT) fluorescence spectroscopy (Fig. 4a). This dye displays a strong fluorescence upon binding to amyloid-like morphologies caused by rotational immobilization, leading to an increase in fluorescence emission with a maximum at 485 nm. All samples were analyzed after 24 h of incubation time. We additionally studied all solutions by cryo-EM to determine the morphology of the formed aggregates (Fig. 4b–e). For **AbuK16** and **MfeGlyK16** we did not observe any increase in fluorescence intensity (FL) (range: 0.01–1 wt%). As discussed above, CD spectroscopy at given concentrations confirms our finding that these peptides do not form β-sheets but instead PPII helices. In contrast, **DfeGlyK16** shows a 9.5-fold enhanced fluorescence emission (1 wt%) compared to the control sample (ThT-dye in buffer without peptide, fluorescence intensity FL_{485nm} = 1.0), indicating the formation of amyloid-like aggregates. A small increase in FL intensity was observed for **DfeGlyK16** at a minimal concentration of 0.25 wt%, which is also the lowest concentration revealing β-sheet structures in the respective CD spectra. **TfeGlyK16** samples show a dramatic enhancement in fluorescence intensity of up to 180-fold at 1 wt%. Furthermore, the presence of amyloid-like fibrils was confirmed by Congo red (CR) staining experiments (see ESI, Fig. S97†). Our results indicate a correlation between the degree of fluorination and the ability to form amyloid-like structures. Cryo-EM studies were performed with those solutions for which a secondary structure pattern or amyloid-like behavior was detected by ThT staining. **DfeGlyK16** (0.25 wt%) (Fig. 4d) and **TfeGlyK16** (0.1 wt%) (Fig. 4e) both form amyloid-like structures. As expected, through CD and ThT staining experiments, **AbuK16** (0.25 wt%) and **MfeGlyK16** (0.25 wt%)

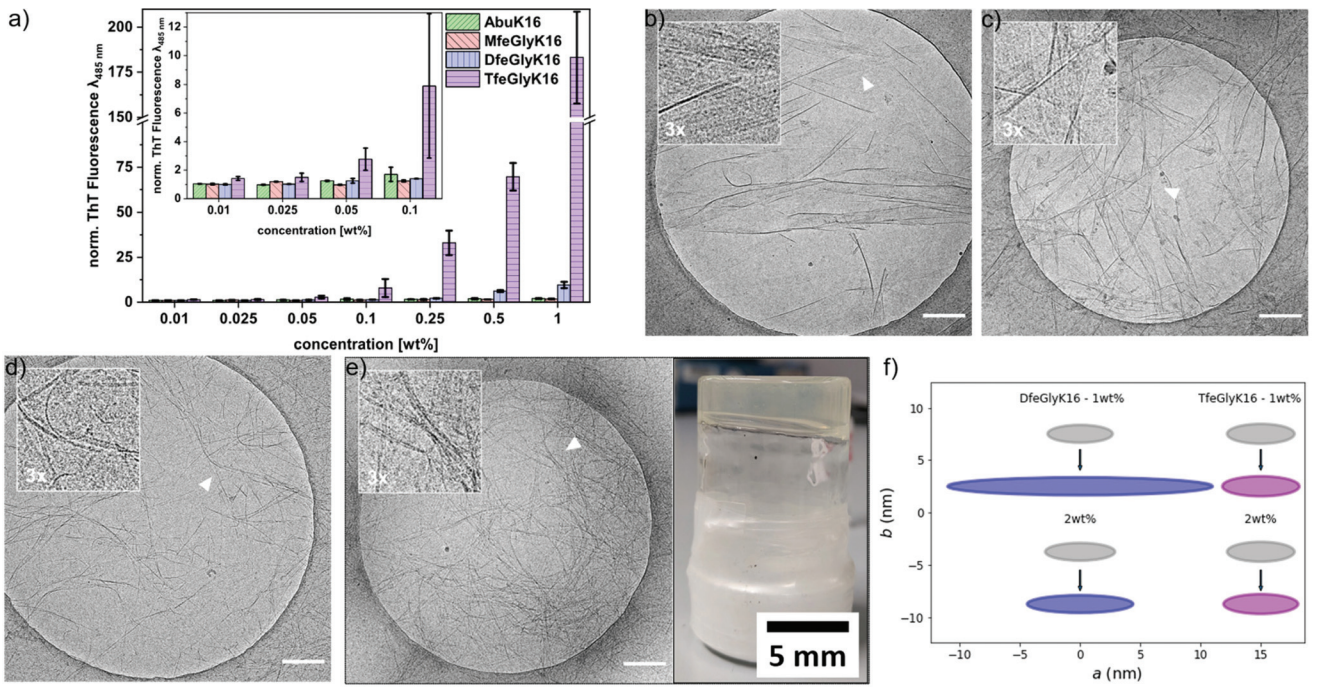

Fig. 4 (a) Thioflavin T assays of **AbuK16** (green), **MfeGlyK16** (red), **DfeGlyK16** (blue) and **TfeGlyK16** (violet) incubated for 24 h at 37 °C in 50 mM Bis-tris propane + 150 mM NaCl containing 20 μM ThT dye, pH 7.4. Fluorescence emission was measured at 485 nm and normalized to a negative control (solely buffer) with a FL intensity of 1.0. Cryo-EM micrographs of (b) **AbuK14** (2 wt%, diluted to 0.2 wt%), (c) **AbuK16** (2 wt%, diluted to 0.2 wt%), (d) **DfeGlyK16** (0.25 wt%) and (e) **TfeGlyK16** (0.1 wt%) + image of a **TfeGlyK16**-based hydrogel at pH 7.4 (0.5 wt%). All samples were dissolved in 50 mM Bis-tris propane + 150 mM NaCl, pH 7.4. Insets display magnified areas of the micrographs indicated by white arrow heads. The scale bar denotes 200 nm for each micrograph. (f) Fibril cross sections corresponding to the SAXS model curves for samples of **DfeGlyK16** and **TfeGlyK16** at concentrations of 1 wt% and 2 wt% obtained through SAXS experiments. The cross-sections are of elliptical shape defined by major and minor semi-axis *a* and *b*, respectively. Plotted are the cross-sections derived from SAXS measurement frames *n* = 1 (after 120 seconds (grey ellipses)) and 50 (after 3000 seconds (colored ellipses)). Fibril growth is illustrated by arrows.

did not form any fibrillary structures (see ESI, Fig. S98–S102†). At elevated concentrations of 2 wt%, however, we detected β-sheet formation for **AbuK14** and **AbuK16** by CD measurements (see prior data in Fig. 1a). Cryo-EM of these **AbuK**-derived sequences at 2 wt% concentration revealed narrow ribbons composed of fibrillar strands in a highly regular line pattern (Fig. 4b and c). A similar morphology from assembled fibrils based on a *de novo* designed coiled coil-based amyloidogenic peptide was studied in prior work.[52] CD data of **MfeGlyK16** at similar concentrations provide a PPII-like structural pattern, and no similar β-sheet assemblies were found in this case. We also applied small-angle X-ray scattering (SAXS) experiments on supposedly amyloid-like fibrils containing solutions of the peptides **AbuK16**, **MfeGlyK16**, **DfeGlyK16** and **TfeGlyK16** over a wide range of concentration (see ESI† for detailed SAXS interpretation). SAXS data from peptides **DfeGlyK16** and **TfeGlyK16** (both 1 wt% and 2 wt%) scale approximately with q^{-1} (**TfeGlyK16**) and q^{-2} (**DfeGlyK16**) at low q-values (see Fig. S111 and S112 in the ESI†). Such scaling behavior indicates a nearly circular cross-section for the fibrils of **TfeGlyK16** (interpreted as circular cylinder) and a flat cross-section for **DfeGlyK16** (interpreted as extended parallelepiped).[29,53] Data evaluation with both theoretical models in terms of time-resolved experiments [with measurement frames of n = 1 (recorded *ca.* 120 s after sample preparation) and n = 50 (recorded 3000 s after sample preparation)] revealed an increase of the major semi axis from a = 2.7 nm to 11.0 nm for **DfeGlyK16** (1 wt%) and from 2.9 nm to 4.4 nm (2 wt%). In contrast, the short semi-axis of the cross section is constant at b = 0.85 nm. For **TfeGlyK16** an increase of the a-axis from 2.8 nm to 3.2 nm and from 2.8 nm to 3.1 nm at 1 wt% and 2 wt%, respectively, was determined. Here, the short semi-axis of the cross section is constant at b = 0.95 nm. An overview on the differences of cross-sections found for both polyfluorinated systems between data frame n = 1 and n = 50 is given in Fig. 4f.

After having characterized the mesoscopic structure of the different systems, we then turned to studying their macroscopic viscoelastic properties. Here, we performed strain-controlled oscillatory shear rheology measurements with the aim of evaluating the influence of fluorination on the mechanical properties of these gel matrices at pH 7.4 and pH 9.0. Amplitude γ (maximum deformation) sweeps at 1 Hz oscillation frequency were performed before the frequency-dependent measurements to ensure that the value γ of the deformation was always chosen such that the experimental conditions remained in the linear viscoelastic (LVE) regime. As a result, the amplitude γ for the oscillatory measurements was fixed at a value of 0.1%. The frequency sweeps were conducted in an angular frequency range of 0.314 to 314 rad s^{-1} to determine the storage and loss moduli G' and G'' (Fig. 5). First, we investigated the peptides **AbuK16**, **MfeGlyK16**, **DfeGlyK16** and **TfeGlyK16** at physiological conditions of pH 7.4 (Fig. 5a and b). As the non-fluorinated **AbuK16** (0.5 wt%) formed only a low viscous solution at physiological conditions, we established a further reference sample comprising a Leu–Lys repeating unit (**LeuK16**, Ac-(Leu–Lys)$_8$-**[4]Abz**-NH_2) to distinguish between the impact of hydrophobicity and fluorine substituents. The Leu–

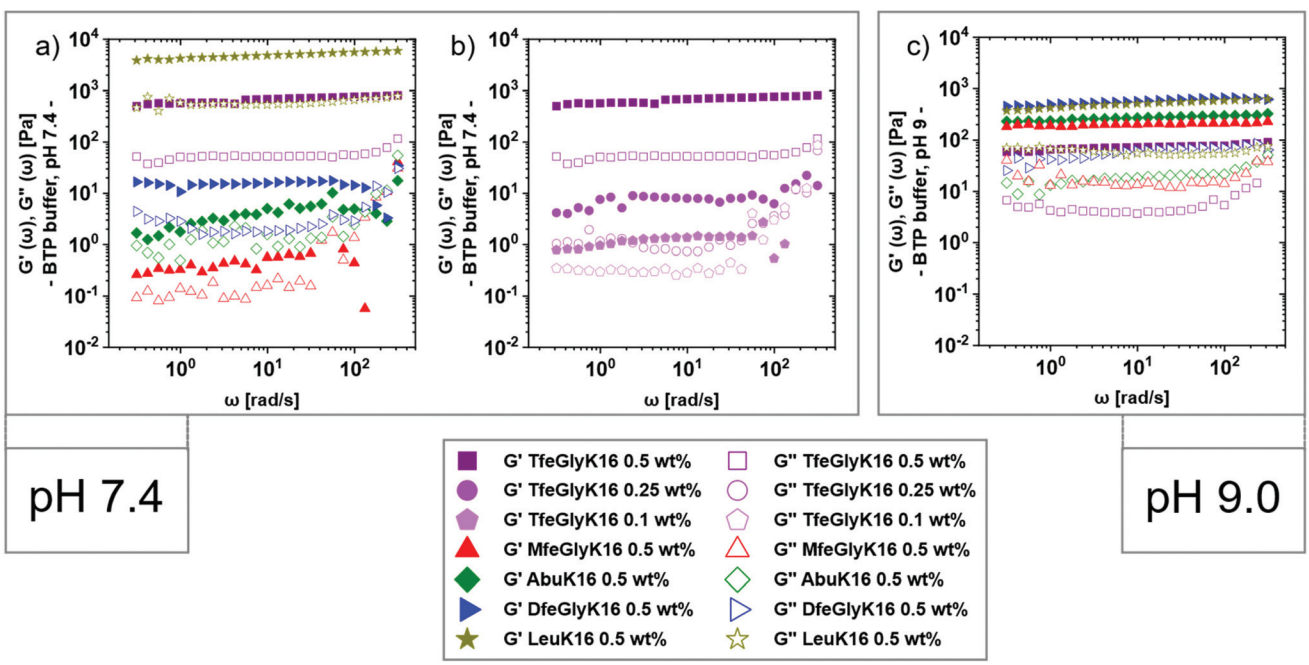

Fig. 5 Storage modulus G' and loss modulus G'' as measured in frequency sweeps (γ = 0.1%) at T = 37 °C for: (a) the peptides **AbuK16**, **MfeGlyK16**, **DfeGlyK16**, **TfeGlyK16** and **LeuK16** (all 0.5 wt%) at pH 7.4; (b) the peptide **TfeGlyK16** at concentrations of 0.5 wt%, 0.25 wt%, and 0.1 wt% at pH 7.4; (c) the peptides **AbuK16**, **MfeGlyK16**, **DfeGlyK16**, **TfeGlyK16** and **LeuK16** (all 0.5 wt%) at pH 9.0. For sample preparation, freeze-dried peptides were dissolved in 50 mM Bis-tris propane + 150 mM NaCl, either pH 7.4 or pH 9.0.

Lys unit was utilized before by Schneider and co-workers for the development of peptide-based hydrogels.[54] Through our RP-HPLC assay, we found **LeuK16** (ϱ = 28.84 ± 0.025 min) to possess greater hydrophobicity than **TfeGlyK16** (see ESI, Fig. S96†). In the case of **TfeGlyK16** measurements were done also at lower concentrations of 0.25 and 0.1 wt%. These data are given in Fig. 5b and show a very strong reduction of the viscoelastic properties upon dilution, the elastic properties being reduced by a factor of around 80. Finally, for all 0.5 wt% samples we also studied their rheological behavior at pH 9.0 to determine how the change in pH affects the viscoelastic properties of the systems. Looking at Fig. 5c one observes that especially the elastic properties described by G' are now much closer than at pH 7.4. For all samples at pH 7.4 and pH 9.0, G' is at about one order of magnitude larger than G'', indicating that these are gel-like systems, for which the elastic properties dominate.[17] Both moduli increase somewhat with increasing frequency, thereby showing power law behavior, but with a rather small exponent. The plateau storage modulus G_0, is of particular interest for gel-like systems. According to classical rubber elasticity theory,[55] G_0 can be related to the crosslinking density ν of the gel. The crosslinking density can in turn be used to estimate an average mesh size ξ in the system, given as:

$$\nu = G_0/kT = \xi^{-3}$$

where k is the Boltzmann constant and T is the temperature. The respective G_0 values for the peptide gels were determined by taking the average of the storage modulus G' data for $\omega \leq 10^2$ rad s^{-1}. These values and calculated mesh sizes are summarized in Table 1. At pH 7.4 and 0.5 wt% concentration, **MfeGlyK16** (0.53 Pa) shows the lowest G_0 value compared to **AbuK16** (4.81 Pa) and its higher fluorinated variants **DfeGlyK16** (15.3 Pa) and **TfeGlyK16** (670 Pa); the reference **LeuK16** possesses by far the highest value of G_0, owing largely to a higher degree of hydrophobicity of the side chain compared to **TfeGly**.[48] Consequently, these experimental data show a consistent analogy to the hydrophobicity trend depicted through our RP-HPLC assay and underline a direct coherence between rheological stiffness and non-polar properties of each amino acid residue (**MfeGly** < **Abu** < **DfeGly** < **TfeGly** < **Leu**). Thus, the successive addition of fluorine atoms strengthens this hydrogel scaffold at physiological conditions.

An interesting behavior is observed upon increasing the pH from 7.4 to 9.0, which lowers the overall charge of the peptide originating from the Lys residues (Fig. 5c). Upon this change, G_0 increases tremendously for **MfeGlyK16** (209 Pa), **AbuK16** (264 Pa) and **DfeGlyK16** (554 Pa) but drops by almost one order of magnitude for **TfeGlyK16** (70 Pa) and **LeuK16** (564 Pa), thereby bringing all the values closer together. This corresponds to an increase of G_0 by a factor of 394 (**MfeGlyK16**), 55 (**AbuK16**) and 36 (**DfeGlyK16**), but also a reduction of G_0 by a factor of 9.6 (**TfeGlyK16**) and 8.6 (**LeuK16**), respectively. The greatest change in viscoelastic stability is observed for the peptide with the lowest hydrophobicity (**MfeGlyK16**) within this work and becomes weaker with increasing non-polar properties (**AbuK16**, **DfeGlyK16**). This surprising loss in G_0 of **TfeGlyK16**-derived hydrogels was confirmed by further measurements at both pH values with independently prepared samples (see ESI, Fig. S104–106†). As an explanation, we suggest a major leverage of side chain-neutralization on the viscoelastic stability of these supramolecular matrices depending rather on peptide hydrophobicity than on fluorine-specific interactions. An almost equal loss in G_0 value in context of pH change found for **LeuK16** in correlation to **TfeGlyK16** serves as further confirmation of this experimental finding. Hence, the divergence in rheological properties between **DfeGlyK16** and **TfeGlyK16**-based hydrogels is, in particular, an interesting phenomenon as it seems to be triggered by only a single H to F substitution of each amino acid residue.

Table 1 Results for the plateau modulus G_0 and corresponding mesh sizes ξ

Name	c (wt%)	pH	G_0 (Pa)	ξ (nm)
LeuK16	0.5	7.4	4869 ± 124	9.83 ± 0.08
		9	564.4 ± 7.2	20.17 ± 0.09
TfeGlyK16	0.5	7.4	670 ± 19	19.05 ± 0.18
		9	70.24 ± 1.4	40.4 ± 0.3
	0.25	7.4	8.63 ± 0.79	81.3 ± 2.5
	0.1	7.4	1.09 ± 0.12	161.9 ± 5.7
DfeGlyK16	0.5	7.4	15.30 ± 1.04	67.14 ± 1.5
		9	554 ± 15	20.29 ± 0.18
AbuK16	0.5	7.4	4.81 ± 0.22	98.72 ± 1.54
		9	264.1 ± 5.1	25.98 ± 0.17
MfeGlyK16	0.5	7.4	0.53 ± 0.02	205.37 ± 2.53
		9	208.8 ± 0.83	28.10 ± 0.04

MD simulations of amphipathic peptides

Finally, we have performed MD simulations of **AbuK16**, **MfeGlyK16**, **DfeGlyK16**, and **TfeGlyK16** in explicit solvent at two different pH values: pH 7 (where for simplicity we assume all Lys residues to be charged) and pH 11 (where we assume all Lys residues to be charge neutral). The aim was to understand how fluorine-specific interactions may modify inter-peptide interactions and thereby control the formation of higher-ordered structures as observed in the above-discussed experiments. Interestingly, we find intra-strand contact pair formations between the fluorine atom of each **MfeGly** residue (**MfeGlyK16**) and backbone hydrogen atoms located on the peptide's amide bonds (Fig. 6a). Such contact pairs are absent in the cases of **DfeGlyK16** and **TfeGlyK16**, whose side chains are randomly oriented as found for **AbuK16** (Fig. 6a). The intra-strand contact pair formation observed for **MfeGlyK16** can be rationalized by the strongly polar **MfeGly** side chain as described before. The free energy profiles of inter-strand interaction as a function of the inter-strand separation for the different peptide types at pH 7 are shown in Fig. 6b, which reveal two distinct minima for each peptide type but **MfeGlyK16**, for which there is only one minimum. The shallow minimum at a larger inter-peptide separation observed for **AbuK16**, **DfeGlyK16**, and **TfeGlyK16** is due to the partially hydrophobic, non-standard (synonymous for **Abu**, **MfeGly**,

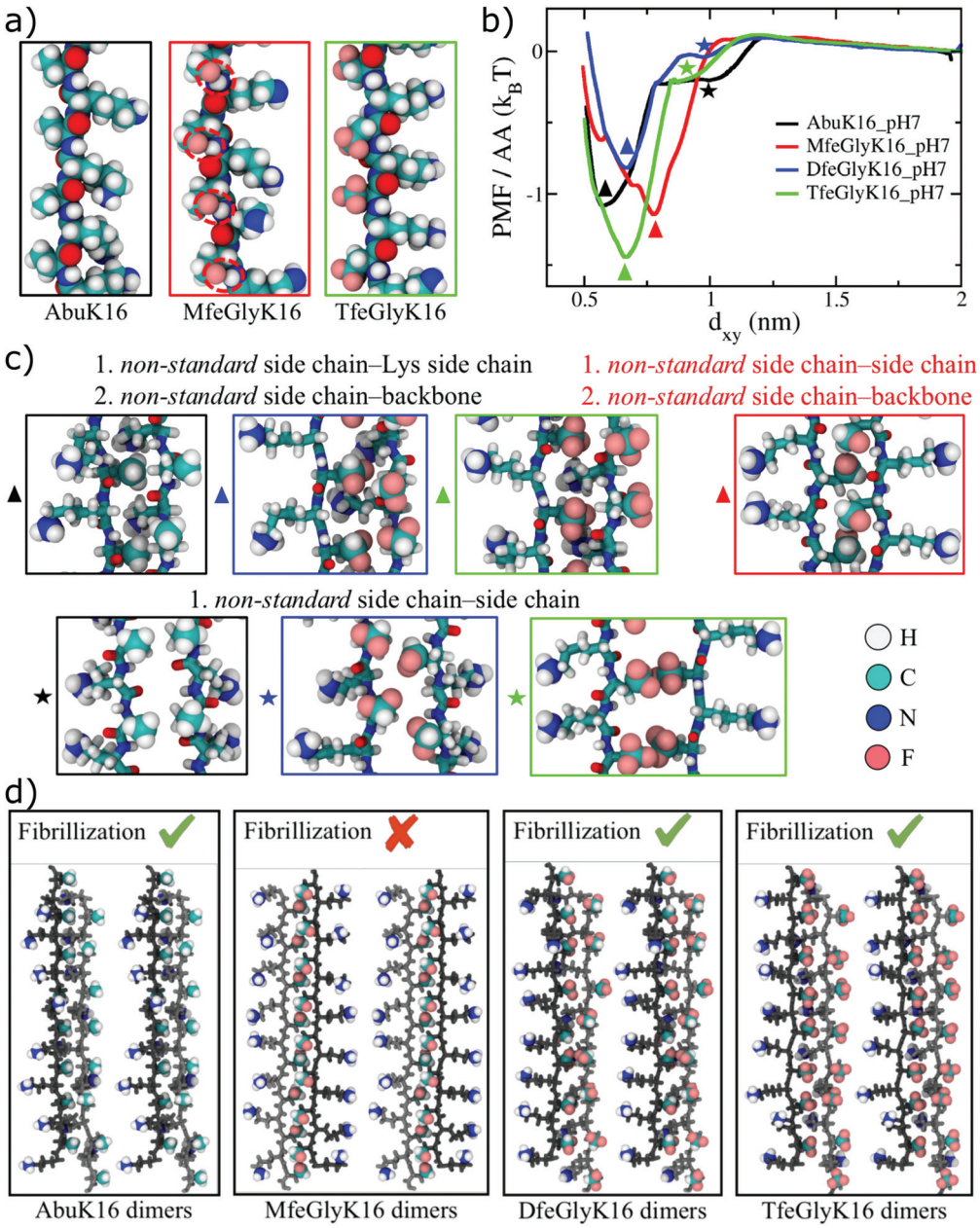

Fig. 6 MD simulation results for amphipathic peptides; water is included in the simulations, but not shown for clarity. (a) Snapshots for representative parts of periodic **AbuK16**, **MfeGlyK16**, and **TfeGlyK16** single strands (taken from umbrella sampling simulations when two strands are far apart) are shown in the space-filling representation and atoms are colored as: H (white), C (cyan), N (blue), O (red), F (pink). Fluorine atoms from **MfeGly** residues and the amide-backbone derived hydrogen atoms form strong intra-strand contact pairs which are marked by red, dashed ellipses. Such contact pairs are not observed for **Abu** and **TfeGly**. (b) The potential of mean force (PMF) per amino acid (AA) as a function of inter-strand separation d_{xy} at pH 7 (charged Lys), depicting the free energy profile of interaction between two peptide strands for side chains with different degree of fluorinations. The global minimum for each peptide type is marked by a triangle, whereas a secondary shallow minimum at a farther distance (when present) is marked by a star symbol. (c) Structures corresponding to free energy minima for each peptide type are shown in ball-stick representation; the terminal group of each side chain is highlighted in the space-filling representation. Atom colors are the same as in (a) and colors of enclosing boxes are the same as colors of the PMF profiles in (b). Dominant binding modes are given at the top of each snapshot. (d) Schematic depicting the possibility of fibrillization of the dimer complex for the different peptide types. One strand of a dimer complex (shown in the ball-stick representation) is colored as light-gray, whereas the other strand is colored as dark-gray. The end groups of side chains from Lys ($-NH_3^+$), **Abu** ($-CH_3$), **MfeGly** ($-CFH_2$), **DfeGly** ($-CF_2H$), and **TfeGly** ($-CF_3$) are highlighted in space-filling representation.

DfeGly and **TfeGly**) amino acid (AA) side chain–side chain interaction, whereas the global minimum at a smaller inter-peptide separation is due to the non-standard AA side chain–Lys side chain and non-standard AA side chain–backbone interactions (see snapshots in Fig. 6c). In contrast, the minimum free-energy structure of **MfeGlyK16** is due to the

polar, non-standard AA side chain–backbone and non-standard AA side chain–side chain interactions, and the charged Lys residues protrude out to minimize the electrostatic repulsion. Although negative and comparable free energy values for all cases imply that every peptide type can form strongly bounded dimers, the possibility of peptide fibril formation depends on whether two such dimers can in turn form favorable contacts with each other. As depicted in Fig. 6d for **AbuK16**, **DfeGlyK16**, and **TfeGlyK16**, two dimers placed parallel to each other can form favorable contacts between the non-standard AA and Lys side chains (which are found to be important for the stability of a dimer as well). In contrast, two **MfeGlyK16** dimers placed parallel to each other face charged end groups of the Lys residue ($-NH_3^+$), and thus repel each other. Therefore, higher-order structure formation or fibrillization at pH 7 is predicted to be possible for **AbuK16**, **DfeGlyK16**, and **TfeGlyK16**, but not for **MfeGlyK16**, explaining our experimental findings at physiological conditions. The free energy profiles at pH 11, shown in Fig. S109† (ESI), reveal only one free-energy minimum for each peptide type, the depth of which is more than that of the corresponding peptide type at pH 7. The increased interaction strength is due to the reduced electrostatic repulsion between the two strands, as Lys residues are charge neutral at pH 11. For **MfeGlyK16**, the intra-strand contact pair formations (Fig. 6a) expose the backbone atoms of **MfeGly** amino acids that can form H-bonds with the solvent-exposed backbone atoms of another **MfeGlyK16** strand, resulting in a very compact **MfeGlyK16** dimer with enhanced side chain–side chain interactions (see snapshots in Fig. S109 within the ESI†). These strong cooperative interactions lead to a 2–3 times deeper free energy minimum for **MfeGlyK16** than other peptide types, for which the inter-peptide interactions are dominated by weak backbone-side chain and side chain–side chain contacts. Like at pH 7, for **AbuK16**, **DfeGlyK16**, and **TfeGlyK16**, two dimers placed parallel to each other can form the same favorable contacts as found in the stable structure of a single dimer, and hence the dimer structure can be periodically extended from either side by adding more dimers to produce large-scale peptide fibrils. For **MfeGlyK16**, the dimer structure is the most stable among the different peptide types and the inter-dimer interaction strength is expected to be lower due to the only possible side chain–side chain interaction as backbone atoms in a dimer complex are shielded by **MfeGly** side chains given by intra-strand contact pair formation. Hence, higher-order structures are expected to be less stable for **MfeGlyK16** and would provide an explanation for its structural properties.

Conclusions

In this work, we systematically designed and characterized a library of oligopeptides with high numbers of fluorinated amino acids. The peptides **AbuK16**, **MfeGlyK16**, **DfeGlyK16** and **TfeGlyK16** served as models to evaluate the impact of fluorine-specific interactions in the context of secondary structure formation, peptide self-assembly and hydrogel formation. The fluorination degree of the aliphatic side chain plays a crucial role in determining the peptide intrinsic hydrophobic properties. This led not only to the observation of different secondary structures such as PPII helices or β-sheets, but also to fluorine-driven self-assembly into ordered nanostructures. On the other hand, we found for **MfeGlyK16** at physiological conditions no evidence of β-sheet assembly, explained by MD simulations that find strong dimer formation preventing peptide fibrillization. Rheological characterization revealed a correlation between the hydrophobic nature of each fluorinated amino acid and an enhanced viscoelastic stability of resulting hydrogel matrices as shown for **MfeGlyK16**, **DfeGlyK16** and **TfeGlyK16** in physiological conditions, but also a loss in mechanical stiffness for the latter variant at pH 9.0. This study firstly established and studied a library of distinctive aliphatic and polyfluorinated SAPs for which fluorine-specific interactions were evinced by significant alterations of intra- and intermolecular interactions. The underlined design principle, the unique properties of the peptides and resulting hydrogel matrices will contribute to the future development of *de novo* designed fluorinated biomaterials.

Experimental section

General methods

^{1}H-, ^{13}C- and ^{19}F-NMR spectra (see ESI†) were recorded at room temperature using a JEOL ECX 400 (JEOL, Tokyo, Japan), a JEOL ECP 500 (JEOL, Tokyo, Japan) or a Bruker AVANCE III 700 (700 MHz, BRUKER, Billerica, MA, USA). Chemical shifts δ are reported in ppm with the solvent resonance (MeOH-d_4) as the internal standard. HRMS were determined on an Agilent 6220 ESI-TOF MS instrument (Agilent Technologies, Santa Clara, CA, USA). For analysis, the MassHunter Workstation Software Version B.02.00 (Agilent Technologies, Santa Clara, CA, USA) was used. IR Spectra were recorded on an ALPHA II FT-IR spectrometer (Bruker, USA). All NMR and IR spectra were evaluated by using Mnova/Mestrenova (Mestrelab Research, CA, USA). Elemental analysis was proceeded by use of an VARIO EL elemental analyzer (Elementar Analysensysteme GmbH, Langenselbold, Germany). All essential data for compound characterization is placed within the ESI.† All chemicals were purchased from commercial sources (Merck, Sigma-Aldrich, VWR, Fluorochem) and used without further purification. The Fmoc-protected fluorinated amino acid **TfeGly** was synthesised according to literature (see ESI,† chapter "Gram scale synthesis and characterization of fluorinated amino acid Fmoc-TfeGly-OH"). **MfeGly** and **DfeGly** were synthesised by Suvrat Chowdhary and Thomas Hohmann.

Synthesis and purification of peptides

All peptides were synthesized with a microwave-equipped Liberty Blue™ peptide synthesizer (CEM, Matthews, NC, USA). A Rink Amide ProTide™ resin (CEM, Matthews, NC, USA) was utilized and the synthesis was performed either in 0.05 mmol or 0.1 mmol scale using oxyma/DIC as activating reagents

(0.05 mmol scale: 0.5 M oxyma in DMF and 0.25 M DIC in DMF/0.1 mmol scale: 1 M oxyma in DMF and 0.5 M DIC in DMF). Coupling of native Fmoc-protected amino acids occurred in DMF using 5 eq. of substance (for fluorinated amino acids only 1.5 eq. were used) with 5 eq. of activating reagents and double couplings of 4 min coupling time (for fluorinated amino acid: mono coupling of 10 min) at 90 °C. For deprotection of the N-terminus, a 10% piperazine (w/v) solution in EtOH/NMP (1 : 9) with 0.1 M HOBt was used. Acetylation was done manually in three batches using acetic anhydride (10% v/v) and DIPEA (10% v/v) in DMF (6 mL). All peptides were cleaved from the resin by treatment with TFA/TIPS/H_2O (90/5/5) for three hours using sonication at room temperature. Then the resins were washed with TFA and DCM, and excess of solvents were removed by evaporation. Peptides were dried by lyophilization before purification with preparative reversed phase HPLC. Purification of synthesized peptides was performed on a Knauer low-pressure HPLC system (Knauer GmbH, Berlin, Germany) sold by VWR (Darmstadt, Germany), comprising a LaPrep Sigma preparative pump (LP1200), a ternary low-pressure gradient, a dynamic mixing chamber, a 6-port-3-channel injection valve with an automated preparative 10 mL sample loop, a LaPrep Sigma standard 1-channel-UV-detector (LP3101), a flow cell with 0.5 mm thickness and a 16-port LaPrep Sigma fractionation valve (LP2016). A Kinetex RPC18 endcapped (5 μM, 100 Å, 250 × 21.2 mm, Phenomenex®, USA) HPLC-column was used. A Security GuardTM PREP Cartridge Holder Kit (21.20 mm, ID, Phenomenex®, USA) served as pre-column. As eluents water and ACN, both containing 0.1% (v/v) TFA were applied. HPLC runs were performed with a flow rate of 15.0 mL min^{-1}, UV-detection occurred at 220 nm for respective peptides. Data analysis occurred with an EZChrom Elite-Software (Version 3.3.2 SP2, Agilent). After separation, the purity of the collected fractions was determined by analytical HPLC. Analytical HPLC was carried out on a Chromaster 600 bar DAD-System with CSM software or a Hitachi Primaide™ UV-HPLC system (both from VWR/Hitachi, Darmstadt, Germany). A Kinetex® RP-C18 (5 μM, 100 Å, 250 × 4.6 mm, Phenomenex®, USA) column and a SecurityGuard™ Cartridge Kit equipped with a C18 cartridge (4 × 3.0 mm, Phenomenex®, USA) as pre-column was used. Otherwise, a Luna® RP-C8 (5 μm, 100 Å, 150 × 3 mm, Phenomenex®, USA) column was used. As eluents water and ACN, both containing 0.1% (v/v) TFA were applied. A flow rate of 1 mL min^{-1} was used and UV-detection occurred at 220 nm or 280 nm for respective peptides. Data analysis was done with EZ Chrom ELITE software (version 3.3.2, Agilent). The resulting pure peptides (>95%) were obtained after lyophilization of the collected fractions. All essential data for the quantification of purified peptides (HPLC data, HRMS spectra) can be found in the ESI (Fig. S37–S91 and Tables S1–S22†).

Lyophilization

To lyophilize the synthesized peptides a laboratory freeze dryer ALPHA 1-2 LD (Christ Gefriertrocknungsanlagen GmbH, Osterode am Harz, Germany) was used.

Sample preparation – exchange of TFA salts

All purified peptides were inevitably obtained as corresponding TFA salts during resin cleavage and subsequent RP-HPLC purification using eluents containing 0.1% TFA. Peptide samples (about 13 mg each) were dissolved in 800 μL Milli-Q-H_2O and transferred on a VariPure IPE exchange column (100 mg, 3 mL) (Agilent Technologies, Santa Clara, CA, USA). These columns were previously washed and pre-conditioned with MeOH (3 × 3 mL) and Milli-Q-H_2O (3 × 3 mL). The resin was additionally washed with Milli-Q-H_2O (500 μL) and the collected peptide fractions were combined. Afterwards, desired samples were lyophilized to obtain the peptide with bicarbonates as counter-ions.

Preparation of peptide stock solutions and self-assembly

Peptide stock solutions were prepared by dissolving lyophilized peptide powder (10–15 mg) in 1,1,1,3,3,3-hexafluoropropan-2-ol [HFIP] (2 mL) and treatment for 15 min in an ultrasound-bath to dissolve preformed aggregates. An aliquot of 10 μL was evaporated and the dried peptide film dissolved in a 6 M guanidine hydrochloride (GndHCl) solution (pH 7.4), resulting into a dilution factor (DL) of 100. These samples were measured *via* UV detection at 280 nm by use of an Eppendorf BioPhotometer plus with semi-micro-VIS Cuvettes (PMMA) 10 × 100 (Eppendorf, Hamburg, Germany). All UV spectra were baseline corrected with a reference spectrum of a sample containing solely buffer solution. The UV absorbance given through the fluorophore *p*-aminobenzoic acid (PABA) at the C-terminus of the peptides at 280 nm was evaluated in triplicates. By use of a calibration curve derived from *p*-aminohippuric acid (PAH) (see ESI, Fig. S92†), the concentration of each stock solution was calculated. If not otherwise stated, all peptide samples were treated following this protocol before each measurement: an aliquot from the HFIP peptide stock solution was taken and evaporated. The dried peptide was then dissolved in respective buffer and vortexed (1 min), sonicated (5 min) and finally ultracentrifuged (1 min) at room temperature.

RP-HPLC assay for estimation of hydrophobicity

The protocol for the RP-HPLC assay was previously established by our group.[28,29] Peptide samples were dissolved in 250 μL of a mixture of 5% (v/v) ACN in 95% (v/v) Milli-Q-water containing 0.1% TFA and filtered over a syringe filter with 0.2 μm pore size. The overall concentration of each sample was 0.2 mM. The retention times of all samples were determined on a C18 column (Capcell C18, 5 μm) using a LaChrom-ELITE-HPLC-System (VWR International) with UV detection at 280 nm. A linear gradient from 5 to 40% ACN + 0.1% TFA in 30 min was applied at room temperature and all experiments were performed in triplicates.

QM calculations

All QM calculations were performed using Gaussian 16.1.[56] **Abu**, **MfeGly**, **DfeGly**, and **TfeGly**-derived motifs, as shown in

Fig. 2b, were taken for QM calculations. Geometry optimizations of these structures were done at the MP2/6-31G* level of theory. Water interaction energies were obtained from the HF/6-31G* single point calculations of the geometry optimized structures. Electrostatic potential maps for the geometry optimized structures were rendered using the Avogadro software.[57] Dihedral energy scans were performed at the MP2/6-31G* level of theory. Force field parameters and partial atomic charges for the amino acid **Abu** and its fluorinated variants (**MfeGly**, **DfeGly**, and **TfeGly**) were initially obtained from CHARMM36m[58] and CGenFF[59] parameters, using the CGenFF program.[60,61] As there were large penalties for dihedral angles associated with side chain rotations (Cα–Cβ–Cγ–F and Cα–Cβ–Cγ–H) and partial atomic charges, new parameters were derived from QM energy scans and water interaction energies, respectively using the FFParam package.[62] Optimized partial atomic charges and dihedral parameters for the different amino acids are given in the ESI† (Chapter 12).

Equilibrium MD simulations

To study interpeptide interactions, two periodic polypeptide chains, each with the long-axis oriented along the *z*-direction, with an interaxial distance d_{xy} of 2.5 nm, arranged antiparallel (ap) to each other were considered. Each system was solvated in a rectangular box of size 5 × 5 × 5.832 nm^3. If needed, enough counterions (Cl^- ions) were added to charge neutralize the whole system. The simulation box is shown in Fig. S108† (ESI). CHARMM-compatible TIP3P water[63,64] and ion parameters[65] were used. The solvated system was subjected to energy minimization using the steepest descent algorithm, for removing any unfavourable contacts. The simulation for each case was performed for 500 ns in the $Np_{xy}L_zT$ ensemble, with L_z per amino acid = 3.6 Å, at T = 300 K and p_{xy} = 1 bar with periodic boundary condition in *xyz* directions, using the GROMACS 2020.1 package.[66] The stochastic velocity rescaling thermostat[67] with a time constant of τ_T = 0.1 ps was used to control the temperature, while for the pressure control a semi-isotropic Parrinello–Rahman barostat[68] was used with a time constant of τ_p = 1 ps and a compressibility of $\kappa = 4.5 \times 10^{-5}$ bar^{-1}. The LINCS algorithm[69] was used to convert the bonds with H-atoms to constraints, allowing a timestep of Δt = 2 fs. Electrostatics interactions were computed using the particle mesh Ewald (PME) method[70] with a real-space cut-off distance of 1.2 nm, while van der Waals (VDW) interactions were modelled using Lennard-Jones potentials with a cut-off distance of 1.2 nm where the resulting forces smoothly switch to zero between 1 nm to 1.2 nm.

Umbrella sampling simulations

To calculate the free energy landscape or the potential of mean force (PMF) between two periodic polypeptide chains, the final configuration obtained from the equilibrium MD simulation was first pulled in either direction to generate initial conformations for two polypeptide chains at different interaxial separations. Total 40–50 umbrella windows, with an inter-window spacing of 0.35 Å, were simulated in the $Np_{xy}L_zT$ for 30 ns each. During these simulations, an additional umbrella potential with a spring constant of 10 000 kJ mol^{-1} nm^{-2} was used to restrain the interaxial separation to a given distance. Every 100 fs data was collected, and the last 20 ns simulation data for each window was used to obtain the PMF using the weighted histogram analysis method (WHAM).[71,72] The g_wham module[73] of GROMACS was used for performing the WHAM analysis and calculating error bars using the bootstrap method.

CD spectroscopy

Circular dichroism experiments were performed using a Jasco J-810 spectropolarimeter fitted with a recirculating chiller (D-76227, Karlsruhe). Data were recorded using 0.1 mm Quartz Suprasil® cuvettes (Hellma) equipped with a stopper. Spectra were recorded at 37 °C from 190 to 250 nm at 0.2 nm intervals, 1 nm bandwidth, 4 s response time and a scan speed of 100 nm min^{-1}. Baselines were recorded and were subtracted from the data. Each reported CD value represents the average of minimum three measurements. Further CD spectra can be found in the ESI (Fig. S93–S95†)

Congo red (CR) assay for fibril detection

Aliquots of peptide HFIP-stock solutions (0.5 wt%) were dried and then redissolved in 50 mM Bis-tris propane + 150 mM NaCl with addition of 50 μM Congo red (overall pH 7.4). Negative controls were prepared by dissolving corresponding samples in buffer without dye. After dissolution, the standard self-assembly protocol was applied, and all samples were incubated overnight at 37 °C. UV spectra (300–700 nm) were recorded for all samples using a Varian Cary 50 UV-VIS Spectrophotometer (Agilent, USA) and 0.5 mm Quartz Suprasil® cuvettes (Hellma). Experimental data can be found in the ESI (Fig. S97†).

Thioflavin T (ThT) fluorescence assay for fibril detection

A suitable protocol for this assay was recently published by our group.[29] Aliquots of peptide HFIP-stock solutions were dried and then redissolved in 50 mM Bis-tris propane + 150 mM NaCl with addition of 20 μM Thioflavin T (overall pH 7.4). The buffer containing ThT was previously filtered over a nylon syringe filter with 0.2 μm pore size. After dissolution, the sample was sonicated for 30 s, transferred on a BRAND® microplate (size: 96 wells, color: black; Sigma-Aldrich), sealed to prevent evaporation and placed in an Infinite® M Nano$^+$ plate reader (Tecan Deutschland GmbH, Crailsheim, Germany). ThT fluorescence (λ_{ex} = 420 nm, λ_{em} = 485 nm, *Z*-position: 15 173 nm [manual], gain: 80 [manual], lag time: 0 μs, integration time: 20 μs) was measured after 24 h incubation at 37 °C. The fluorescence intensity at 485 nm was normalized with respect to the negative control solely containing buffer (set as FL_{int} 1.0).

Cryogenic electron microscopy (cryo-EM)

Perforated carbon film-covered microscopical 200 mesh grids (R1/4 batch of Quantifoil, MicroTools GmbH, Jena, Germany)

were cleaned with chloroform and hydrophilized by 60 s glow discharging at 10 μA in a EMSCOPE SC500 before 4 μl aliquots of the peptide solution were applied to the grids. The samples were vitrified by automatic blotting and plunge freezing with a FEI Vitrobot Mark IV (Thermo Fisher Scientific Inc., Waltham, Massachusetts, USA) using liquid ethane as cryogen. The vitrified specimens were transferred to the autoloader of a FEI TALOS ARCTICA electron microscope (Thermo Fisher Scientific Inc., Waltham, Massachusetts, USA). This microscope is equipped with a high-brightness field-emission gun (XFEG) operated at an acceleration voltage of 200 kV. Micrographs were acquired on a FEI Falcon 3 direct electron detector (Thermo Fisher Scientific Inc., Waltham, Massachusetts, USA) using the 70 μm objective aperture at a nominal magnification of 28 000, corresponding to a calibrated pixel size of 3.75 Å per pixel, respectively.

Small-angle-X-ray scattering (SAXS)

SAXS measurement were performed in a flow-through capillary with a Kratky-type instrument (SAXSess from Anton Paar, Austria) at 37 ± 1 °C. The SAXSess has a low sample-to-detector distance of 0.309 m, which is appropriate for investigations of liquid samples with low scattering intensities. The measured intensity was converted to absolute scale according to Orthaber *et al.*[74] The scattering vector q is defined in terms of the scattering angle θ and the wavelength λ of the radiation (λ = 0.154 nm): thus, $q = 4\pi n/\lambda \sin\theta$. Deconvolution (slit length desmearing) of the SAXS curves was performed with the SAXS-Quant software. Samples analyzed with SAXS were used as prepared, *i.e.* samples were mixed with buffer solution, vortexed for 20 s and filled in the capillary. Curve fitting was conducted with SASfit.[75]

Rheological characterization of amphipathic peptide hydrogels

Before each measurement, peptide samples of **AbuK16**, **MfeGlyK16**, **DfeGlyK16**, **TfeGlyK16** and **LeuK16** were dissolved in 50 mM Bis-tris propane + 150 mM NaCl (either pH 7.4 or pH 9.0), treated as mentioned above and incubated at 37 °C for 24 h. All rheological measurements were performed on an Anton Paar MCR 502 WESP temperature-controlled rheometer in strain-imposed mode at physiological temperature (37 °C). For all measurements, a parallel plate geometry with chromium oxide coating was used, with a diameter of 50 mm for the upper rotating plate. The gap size between the plates was set to 175 μm. The sample and geometry were surrounded by a solvent trap to reduce effects of solvent evaporation. Further experimental data can be found in the ESI (Fig. S97†).

Author contributions

B. K. and S. C. conceived the overall project. B. K. provided guidance on data analysis, interpretation, and manuscript preparation. S. C. designed and developed concepts and experiments, synthesized, and purified all peptides, performed CD, UV and FL experiments, established and proceeded a RP-HPLC-based hydrophobicity plot for peptides, prepared samples for further experiments and wrote the manuscript. R. F. S. performed rheology experiments and wrote the manuscript. A. K. S. performed simulations. A. K. S. and R. R. N. analyzed and interpreted data and wrote the manuscript. T. t. D. assisted S. C. in synthesis and purification of peptides and circular dichroism experiments. K. B.-J. and A. F. T. performed SAXS experiments and SAXS data analysis. T. H. provided fluorinated amino acids. B. S. performed cryoEM experiments, analyzed, and interpreted data. R. R. N. and M. G. provided expertise and feedback.

Conflicts of interest

There are no conflicts to declare.

Acknowledgements

S. C., T. H., B. S., R. R. N. and B. K. gratefully acknowledges financial support by the Deutsche Forschungsgemeinschaft (DFG) through the collaborative research center CRC 1349 "Fluorine-Specific Interactions", project no. 387284271. R. F. S., M. G., and R. R. N. were funded by the DFG grant CRC 1449 "Dynamic Hydrogels at Biointerfaces", project no. 431232613. We thank Dr Johann Moschner, Dr Katharina Hellmund, Dr Dorian Jamal Mikolajczak, Dr Ana Rita de Lima Fernandes, Dr Allison Berger, and Dr Chaitanya Kumar Thota for fruitful scientific discussions and expertise. We thank Dr Jakob Leppkes for his support during the synthesis of fluorinated amino acids. We would like to acknowledge the assistance of the Core Facility BioSupraMol supported by the DFG. We thank Benedikt Kirmayer for assistance in the preparation of cryo-EM samples and micrographs. A. K. S. and R. R. N. acknowledge support from the Max-Planck MaxWater initiative.

Notes and references

1 A. Levin, T. A. Hakala, L. Schnaider, G. J. L. Bernardes, E. Gazit and T. P. J. Knowles, *Nat. Rev. Chem.*, 2020, **4**, 615–634.
2 S. Zhang, *Nat. Biotechnol.*, 2003, **21**, 1171–1178.
3 J. P. Schneider, D. J. Pochan, B. Ozbas, K. Rajagopal, L. Pakstis and J. Kretsinger, *J. Am. Chem. Soc.*, 2002, **124**, 15030–15037.
4 B. Ozbas, J. Kretsinger, K. Rajagopal, J. P. Schneider and D. J. Pochan, *Macromolecules*, 2004, **37**, 7331–7337.
5 S. Zhang, T. Holmes, C. Lockshin and A. Rich, *Proc. Natl. Acad. Sci. U. S. A.*, 1993, **90**, 3334–3338.
6 S. Zhang, T. C. Holmes, C. M. DiPersio, R. O. Hynes, X. Su and A. Rich, *Biomaterials*, 1995, **16**, 1385–1393.
7 F. Gelain, Z. Luo and S. Zhang, *Chem. Rev.*, 2020, **120**, 13434–13460.
8 F. Gelain, Z. Luo, M. Rioult and S. Zhang, *npj Regener. Med.*, 2021, **6**, 9.

9 C. J. C. Edwards-Gayle and I. W. Hamley, *Org. Biomol. Chem.*, 2017, **15**, 5867–5876.
10 V. Castelletto, C. J. C. Edwards-Gayle, F. Greco, I. W. Hamley, J. Seitsonen and J. Ruokolainen, *ACS Appl. Mater. Interfaces*, 2019, **11**, 33573–33580.
11 S. Motamed, M. P. Del Borgo, K. Kulkarni, N. Habila, K. Zhou, P. Perlmutter, J. S. Forsythe and M. I. Aguilar, *Soft Matter*, 2016, **12**, 2243–2246.
12 P.-X. Zhang, N. Han, Y.-H. Kou, Q.-T. Zhu, X.-L. Liu, D.-P. Quan, J.-G. Chen and B.-G. Jiang, *Neural Regener. Res.*, 2019, **14**, 51–58.
13 K. S. Hellmund, B. von Lospichl, C. Böttcher, K. Ludwig, U. Keiderling, L. Noirez, A. Weiß, D. J. Mikolajczak, M. Gradzielski and B. Koksch, *Pept. Sci.*, 2021, **113**, e24201.
14 S. Lee, T. H. T. Trinh, M. Yoo, J. Shin, H. Lee, J. Kim, E. Hwang, Y.-B. Lim and C. Ryou, *Int. J. Mol. Sci.*, 2019, **20**, 5850.
15 J. Y. C. Lim, Q. Lin, K. Xue and X. J. Loh, *Mater. Today Adv.*, 2019, **3**, 100021.
16 X. Zhao and S. Zhang, *Chem. Soc. Rev.*, 2006, **35**, 1105–1110.
17 L. M. De Leon Rodriguez, Y. Hemar, J. Cornish and M. A. Brimble, *Chem. Soc. Rev.*, 2016, **45**, 4797–4824.
18 J. Kopeček and J. Yang, *Acta Biomater.*, 2009, **5**, 805–816.
19 J. N. Sloand, M. A. Miller and S. H. Medina, *Pept. Sci.*, 2021, **113**, e24184.
20 A. A. Berger, J.-S. Völler, N. Budisa and B. Koksch, *Acc. Chem. Res.*, 2017, **50**, 2093–2103.
21 E. N. G. Marsh, *Acc. Chem. Res.*, 2014, **47**, 2878–2886.
22 S. A. Samsonov, M. Salwiczek, G. Anders, B. Koksch and M. T. Pisabarro, *J. Phys. Chem. B*, 2009, **113**, 16400–16408.
23 M. Salwiczek, S. Samsonov, T. Vagt, E. Nyakatura, E. Fleige, J. Numata, H. Cölfen, M. T. Pisabarro and B. Koksch, *Chem. – Eur. J.*, 2009, **15**, 7628–7636.
24 S. Huhmann, E. K. Nyakatura, H. Erdbrink, U. I. M. Gerling, C. Czekelius and B. Koksch, *J. Fluorine Chem.*, 2015, **175**, 32–35.
25 T. Vagt, E. Nyakatura, M. Salwiczek, C. Jäckel and B. Koksch, *Org. Biomol. Chem.*, 2010, **8**, 1382–1386.
26 S. Ye, B. Loll, A. A. Berger, U. Mülow, C. Alings, M. C. Wahl and B. Koksch, *Chem. Sci.*, 2015, **6**, 5246–5254.
27 J. Leppkes, N. Dimos, B. Loll, T. Hohmann, M. Dyrks, A. R. Wieseke, B. G. Keller and B. Koksch, *RSC Chem. Biol.*, 2022, **3**(6), 773–782.
28 U. I. M. Gerling, M. Salwiczek, C. D. Cadicamo, H. Erdbrink, C. Czekelius, S. L. Grage, P. Wadhwani, A. S. Ulrich, M. Behrends, G. Haufe and B. Koksch, *Chem. Sci.*, 2014, **5**, 819–830.
29 S. Chowdhary, J. Moschner, D. J. Mikolajczak, M. Becker, A. F. Thünemann, C. Kästner, D. Klemczak, A.-K. Stegemann, C. Böttcher, P. Metrangolo, R. R. Netz and B. Koksch, *ChemBioChem*, 2020, **21**, 3544–3554.
30 S. Huhmann and B. Koksch, *Eur. J. Org. Chem.*, 2018, **2018**, 3667–3679.
31 C. K. Thota, A. A. Berger, B. Harms, M. Seidel, C. Böttcher, H. von Berlepsch, C. Xie, R. Süssmuth, C. Roth and B. Koksch, *Pept. Sci.*, 2020, **112**, e24130.
32 F. Agostini, L. Sinn, D. Petras, C. J. Schipp, V. Kubyshkin, A. A. Berger, P. C. Dorrestein, J. Rappsilber, N. Budisa and B. Koksch, *ACS Cent. Sci.*, 2021, **7**, 81–92.
33 J.-S. Völler, M. Dulic, U. I. M. Gerling-Driessen, H. Biava, T. Baumann, N. Budisa, I. Gruic-Sovulj and B. Koksch, *ACS Cent. Sci.*, 2017, **3**, 73–80.
34 J. Moschner, V. Stulberg, R. Fernandes, S. Huhmann, J. Leppkes and B. Koksch, *Chem. Rev.*, 2019, **119**, 10718–10801.
35 J. Leppkes, T. Hohmann and B. Koksch, *J. Fluorine Chem.*, 2020, **232**, 109453.
36 H. Mei, T. Hiramatsu, R. Takeda, H. Moriwaki, H. Abe, J. Han and V. A. Soloshonok, *Org. Process Res. Dev.*, 2019, **23**, 629–634.
37 J. Han, R. Takeda, X. Liu, H. Konno, H. Abe, T. Hiramatsu, H. Moriwaki and V. A. Soloshonok, *Molecules*, 2019, **24**, 4521.
38 Y. Nian, J. Wang, H. Moriwaki, V. A. Soloshonok and H. Liu, *Dalton Trans.*, 2017, **46**, 4191–4198.
39 T. T. Romoff, A. B. Palmer, N. Mansour, C. J. Creighton, T. Miwa, Y. Ejima, H. Moriwaki and V. A. Soloshonok, *Org. Process Res. Dev.*, 2017, **21**, 732–739.
40 T. Hohmann, M. Dyrks, S. Chowdhary, M. Weber, D. Nguyen, J. Moschner and B. Koksch, ChemRxiv, 2022, this content is a preprint and has not been peer-reviewed.
41 R. Gambaretto, L. Tonin, C. Di Bello and M. Dettin, *Biopolymers*, 2008, **89**, 906–915.
42 G. D'Auria, M. Vacatello, L. Falcigno, L. Paduano, G. Mangiapia, L. Calvanese, R. Gambaretto, M. Dettin and L. Paolillo, *J. Pept. Sci.*, 2009, **15**, 210–219.
43 K. Güçlü, G. Kıbrıslıoğlu, M. Özyürek and R. Apak, *J. Agric. Food Chem.*, 2014, **62**, 1839–1845.
44 A. K. Pandey, K. M. Thomas, C. R. Forbes and N. J. Zondlo, *Biochemistry*, 2014, **53**, 5307–5314.
45 T. J. Measey, R. Schweitzer-Stenner, V. Sa and K. Kornev, *Macromolecules*, 2010, **43**, 7800–7806.
46 Y. Cho, L. B. Sagle, S. Iimura, Y. Zhang, J. Kherb, A. Chilkoti, J. M. Scholtz and P. S. Cremer, *J. Am. Chem. Soc.*, 2009, **131**, 15188–15193.
47 T. J. Measey and R. Schweitzer-Stenner, *J. Am. Chem. Soc.*, 2006, **128**, 13324–13325.
48 M. Salwiczek, E. K. Nyakatura, U. I. M. Gerling, S. Ye and B. Koksch, *Chem. Soc. Rev.*, 2012, **41**, 2135–2171.
49 J. R. Robalo and A. Vila Verde, *Phys. Chem. Chem. Phys.*, 2019, **21**, 2029–2038.
50 Y. Chen, Y. Hua, W. Zhang, C. Tang, Y. Wang, Y. Zhang and F. Qiu, *Int. J. Nanomed.*, 2018, **13**, 2477–2489.
51 A. Bertolani, L. Pirrie, L. Stefan, N. Houbenov, J. S. Haataja, L. Catalano, G. Terraneo, G. Giancane, L. Valli, R. Milani, O. Ikkala, G. Resnati and P. Metrangolo, *Nat. Commun.*, 2015, **6**, 7574.
52 M. S. de Freitas, R. Rezaei Araghi, E. Brandenburg, J. Leiterer, F. Emmerling, K. Folmert, U. I. M. Gerling-Driessen, B. Bardiaux, C. Böttcher, K. Pagel, A. Diehl, H. v. Berlepsch, H. Oschkinat and B. Koksch, *J. Struct. Biol.*, 2018, **203**, 263–272.

53 J. Schmitt, V. Calabrese, M. A. da Silva, S. Lindhoud, V. Alfredsson, J. L. Scott and K. J. Edler, *Phys. Chem. Chem. Phys.*, 2018, **20**, 16012–16020.
54 I. M. Geisler and J. P. Schneider, *Adv. Funct. Mater.*, 2012, **22**, 529–537.
55 P. J. Flory and J. Rehner Jr., *J. Chem. Phys.*, 1943, **11**, 521–526.
56 M. J. Frisch, G. W. Trucks, H. B. Schlegel, G. E. Scuseria, M. A. Robb, J. R. Cheeseman, G. Scalmani, V. Barone, G. A. Petersson, H. Nakatsuji, X. Li, M. Caricato, A. V. Marenich, J. Bloino, B. G. Janesko, R. Gomperts, B. Mennucci, H. P. Hratchian, J. V. Ortiz, A. F. Izmaylov, J. L. Sonnenberg, D. Williams, F. Ding, F. Lipparini, F. Egidi, J. Goings, B. Peng, A. Petrone, T. Henderson, D. Ranasinghe, V. G. Zakrzewski, J. Gao, N. Rega, G. Zheng, W. Liang, M. Hada, M. Ehara, K. Toyota, R. Fukuda, J. Hasegawa, M. Ishida, T. Nakajima, Y. Honda, O. Kitao, H. Nakai, T. Vreven, K. Throssell, J. A. Montgomery Jr., J. E. Peralta, F. Ogliaro, M. J. Bearpark, J. J. Heyd, E. N. Brothers, K. N. Kudin, V. N. Staroverov, T. A. Keith, R. Kobayashi, J. Normand, K. Raghavachari, A. P. Rendell, J. C. Burant, S. S. Iyengar, J. Tomasi, M. Cossi, J. M. Millam, M. Klene, C. Adamo, R. Cammi, J. W. Ochterski, R. L. Martin, K. Morokuma, O. Farkas, J. B. Foresman and D. J. Fox, *Gaussian 16 Rev. C.01*, 2016.
57 M. D. Hanwell, D. E. Curtis, D. C. Lonie, T. Vandermeersch, E. Zurek and G. R. Hutchison, *J. Cheminf.*, 2012, **4**, 17.
58 J. Huang, S. Rauscher, G. Nawrocki, T. Ran, M. Feig, B. L. de Groot, H. Grubmüller and A. D. MacKerell, *Nat. Methods*, 2017, **14**, 71–73.
59 K. Vanommeslaeghe, E. Hatcher, C. Acharya, S. Kundu, S. Zhong, J. Shim, E. Darian, O. Guvench, P. Lopes, I. Vorobyov and A. D. Mackerell, Jr., *J. Comput. Chem.*, 2010, **31**, 671–690.
60 K. Vanommeslaeghe and A. D. MacKerell, *J. Chem. Inf. Model.*, 2012, **52**, 3144–3154.
61 K. Vanommeslaeghe, E. P. Raman and A. D. MacKerell, *J. Chem. Inf. Model.*, 2012, **52**, 3155–3168.
62 A. Kumar, O. Yoluk and A. D. MacKerell, Jr., *J. Comput. Chem.*, 2020, **41**, 958–970.
63 W. L. Jorgensen, J. Chandrasekhar, J. D. Madura, R. W. Impey and M. L. Klein, *J. Chem. Phys.*, 1983, **79**, 926–935.
64 A. D. MacKerell Jr., D. Bashford, M. Bellott, R. L. Dunbrack Jr., J. D. Evanseck, M. J. Field, S. Fischer, J. Gao, H. Guo and S. Ha, *J. Phys. Chem. B*, 1998, **102**, 3586–3616.
65 R. M. Venable, Y. Luo, K. Gawrisch, B. Roux and R. W. Pastor, *J. Phys. Chem. B*, 2013, **117**, 10183–10192.
66 M. J. Abraham, T. Murtola, R. Schulz, S. Páll, J. C. Smith, B. Hess and E. Lindahl, *SoftwareX*, 2015, **1**, 19–25.
67 G. Bussi, D. Donadio and M. Parrinello, *J. Chem. Phys.*, 2007, **126**, 014101.
68 M. Parrinello and A. Rahman, *J. Appl. Phys.*, 1981, **52**, 7182–7190.
69 B. Hess, *J. Chem. Theory Comput.*, 2008, **4**, 116–122.
70 T. Darden, D. York and L. Pedersen, *J. Chem. Phys.*, 1993, **98**, 10089–10092.
71 G. M. Torrie and J. P. Valleau, *J. Comput. Phys.*, 1977, **23**, 187–199.
72 S. Kumar, J. M. Rosenberg, D. Bouzida, R. H. Swendsen and P. A. Kollman, *J. Comput. Chem.*, 1992, **13**, 1011–1021.
73 J. S. Hub, B. L. De Groot and D. Van Der Spoel, *J. Chem. Theory Comput.*, 2010, **6**, 3713–3720.
74 D. Orthaber, A. Bergmann and O. Glatter, *J. Appl. Crystallogr.*, 2000, **33**, 218–225.
75 I. Bressler, J. Kohlbrecher and A. F. Thünemann, *J. Appl. Crystallogr.*, 2015, **48**, 1587–1598.

Rational Design of Amphiphilic Fluorinated Peptides: Evaluation of Self-Assembly Properties and Hydrogel Formation

Suvrat Chowdhary[1], Robert F. Schmidt[2], Dr. Anil Kumar Sahoo[3,4], Tiemo tom Dieck[1], Thomas Hohmann[1], Dr. Boris Schade[5], Kerstin Brademann-Jock[6], Dr. Andreas Thünemann[6], Prof. Dr. Roland R. Netz[3], Prof. Dr. Michael Gradzielski[2] and Prof. Dr. Beate Koksch[1]*

1 Institute of Chemistry and Biochemistry, Freie Universität Berlin, Arnimallee 20, 14195 Berlin, Germany
2 Institute of Chemistry, Technische Universität Berlin, Straße des 17. Juni 124, 10623 Berlin, Germany
3 Department of Physics, Freie Universität Berlin, Arnimallee 14, 14195 Berlin, Germany
4 Max Planck Institute of Colloids and Interfaces, Department of Biomaterials, Am Mühlenberg 1, 14476 Potsdam, Germany
5 Institute of Chemistry and Biochemistry and Core Facility *BioSupraMol*, Freie Universität Berlin, Fabeckstraße 36a, 14195 Berlin, Germany
6 Federal Institute for Materials Research and Testing (BAM), Unter den Eichen 87, 12205 Berlin, Germany

*** Corresponding author:**
Prof. Dr. Beate Koksch; beate.koksch@fu-berlin.de; Phone: +49 30 838 55344

Supporting Information

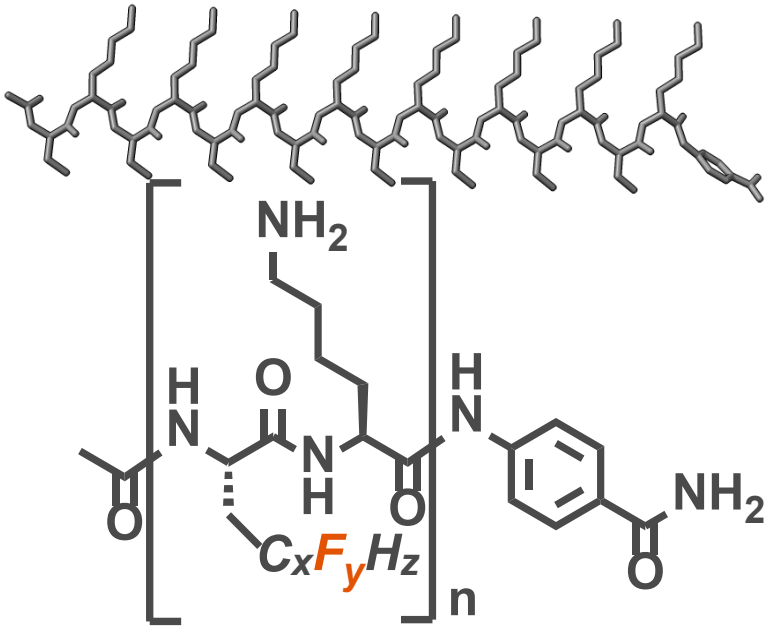

Content

1. Gram scale synthesis and characterization of fluorinated amino acid Fmoc-TfeGly-OH (6)

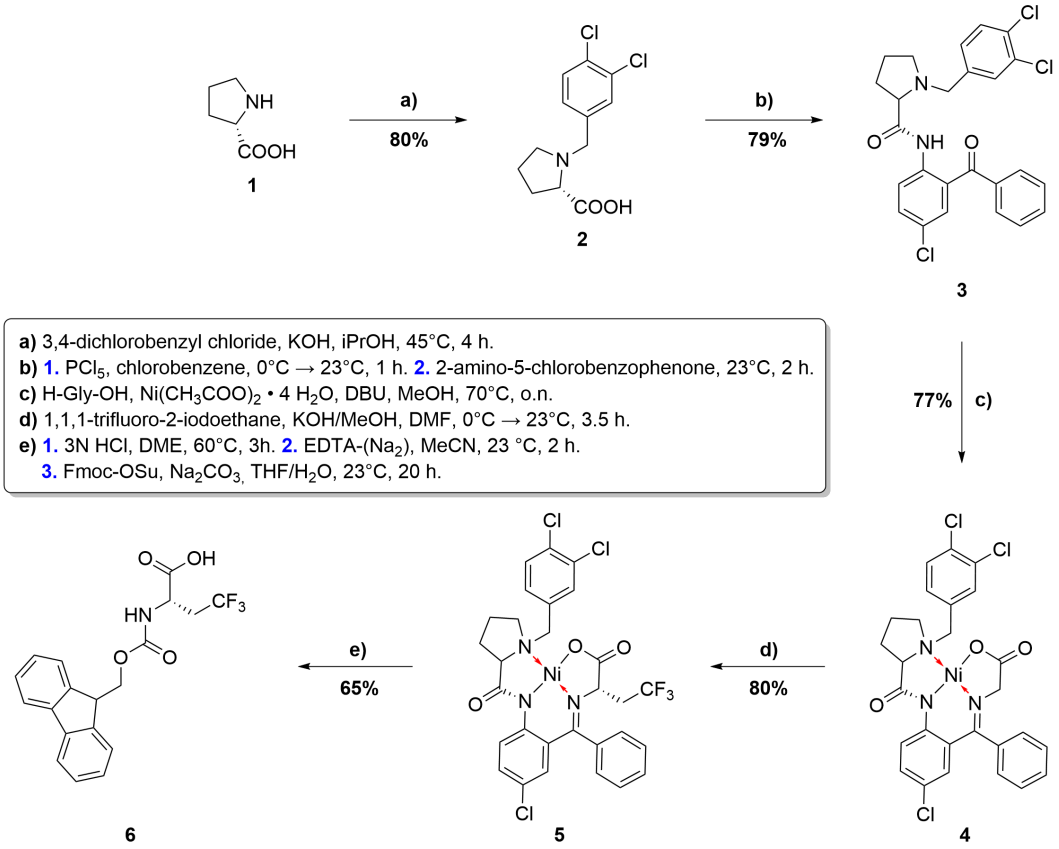

Scheme S1: Synthesis of Fmoc-TfeGly-OH **(6)** in gram scale according to Soloshonok *et al.*[1-9]

A five-step synthesis for Fmoc-TfeGly-OH **(6)** was developed and described in literature by Soloshonok *et al.*[1-9] In the first step of this synthetic route, H-Pro-OH **1** is alkylated with 3,4-dichlorobenzyl chloride. To selectively alkylate the amine and not the C-terminal carboxyl group, the reaction is carried out in a basic KOH / iPrOH solution. The intermediate **2** reacts afterwards with PCl_5 to form the corresponding acid chloride, enabling the formation of an amide bond with the amine side chain of 2-amino-5-chlorobenzophenone and the synthesis of compound **3**. The formation of the Schiff base as a chelating ligand in compound **4** occurs trough the reaction of **3** with H-Gly-OH, nickel acetate tetrahydrate and DBU. The following asymmetric alkylation of the chiral Ni-ligand **4** with CF_3CH_2I and subsequent disassembly of compound **5** and simultaneous Fmoc-protection leads finally to the *N*-Fmoc derivative of (2*S*)-4,4,4-trifluoroethylglycine (TfeGly).

1.1 Synthesis of (3,4-dichlorobenzyl)-L-proline (2)

L-Pro-H **(1)** (69.0 g, 0.6 mol, 1 equiv.) and KOH (70.6 g, 1.26 mol, 2.1 equiv) were dissolved in iPrOH (600 mL) at 45 °C. Afterwards 3,4-dichlorobenzyl chloride (91.1 mL, 0.66 mol, 1.1 equiv.) were added and the reaction mixture was stirred for 4 h at 45 °C. For quenching, the pH was adjusted to 5-6 with $HCl_{conc.}$ and MeOH (1000 mL) was added. The reaction mixture was then stirred for 16 h at 45°C and precipitated KCl salts were filtered and washed with a iPrOH/MeoH mixture (3:2). The filtrated solution was concentrated under reduced pressure and the crude product was washed with MeCN (500 mL) for 10 min under gentle stirring. Finally, the product was filtered, washed with MeCN and dried *in vacuo*.

The title compound **2** was obtained as a white solid substance (133.32 g, 0.48 mol, 80%).

^{1}H NMR (600 MHz, METHANOL-D_4): δ = **7.67** (d, J = 2.2 Hz, 1H), **7.49** (d, J = 8.3 Hz, 1H), **7.38** (dd, J = 8.3, 2.2 Hz, 1H), **4.35** (d, J = 13.0 Hz, 1H), **4.18** (d, J = 12.9 Hz, 1H), **3.79** (dd, J = 9.6, 6.7 Hz, 1H), **3.49 – 3.44** (m, 1H), **3.16 – 3.07** (m, 1H), **2.42 – 2.32** (m, 1H), **2.05 – 1.96** (m, 2H), 1.92 – 1.79 (m, 1H).

^{13}C ^{10} NMR (151 MHz, METHANOL-D_4): δ = 171.88, 170.55, 168.50, 142.06, 128.74, 127.98, 118.88, 40.90, 22.62.

IR (ATR): ν = 3059.34, 2974.98, 2858.70, 1603.14, 1526.06, 1477.04, 1386.78, 1374.44, 1308.48, 1145.31, 1022.05, 835.23, 813.93, 663.51, 651.15, 496.65, 489.81, 400.90 cm^{-1}.

Elemental analysis [CHN] (%) = Anal. Calcd for $C_{12}H_{13}Cl_2NO_2$ (m: 1.9720 mg): C, 52.58; H, 4.78; N, 5.11. Found: C, 50.51; H, 4.72; N, 5.35.

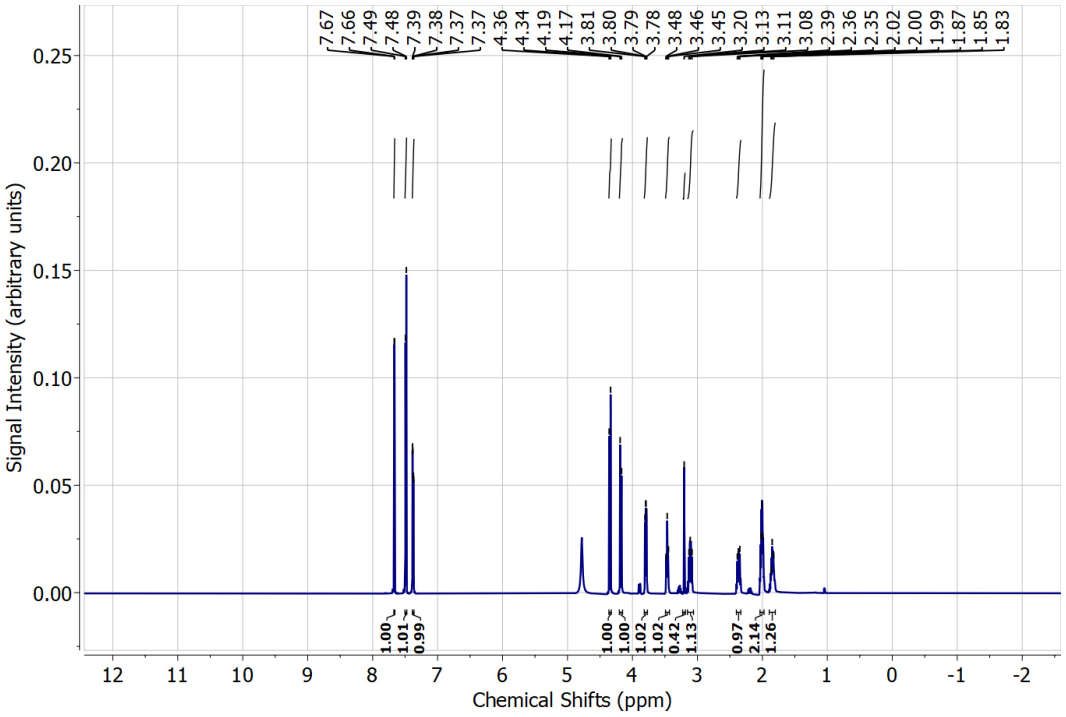

Figure S1: ^{1}H NMR (600 MHz) spectrum of (3,4-dichlorobenzyl)-L-proline **(2)** dissolved in MeOH-d_4.

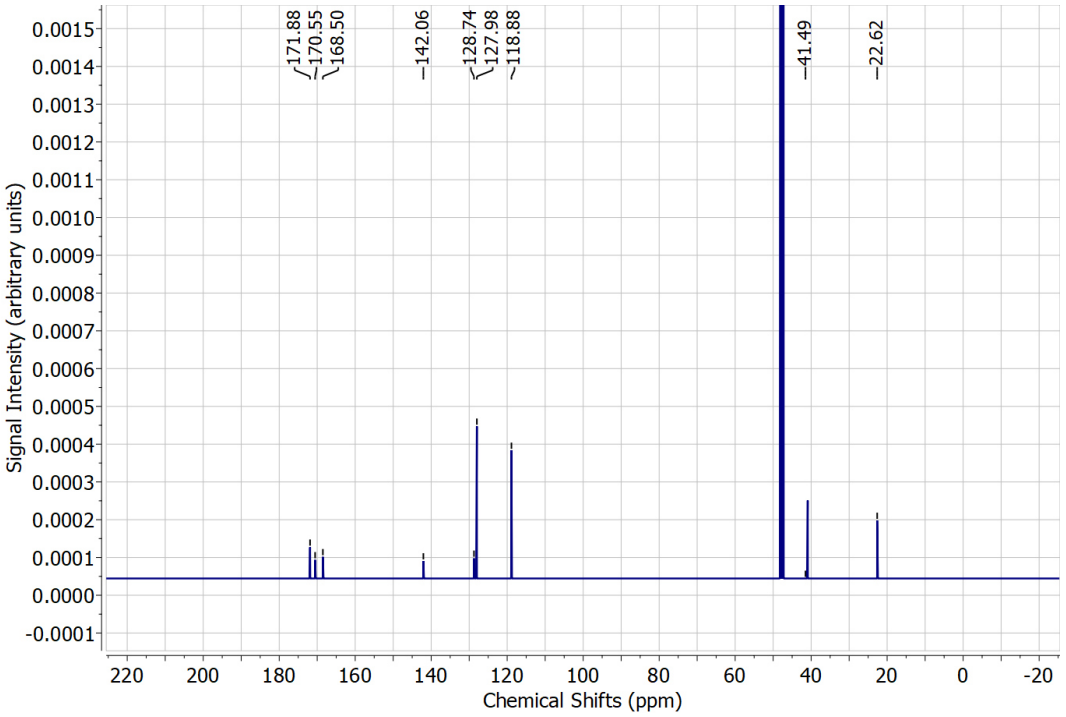

Figure S2: ^{13}C {1H} NMR (151 MHz) spectrum of (3,4-dichlorobenzyl)-L-proline **(2)** dissolved in MeOH-d_4.

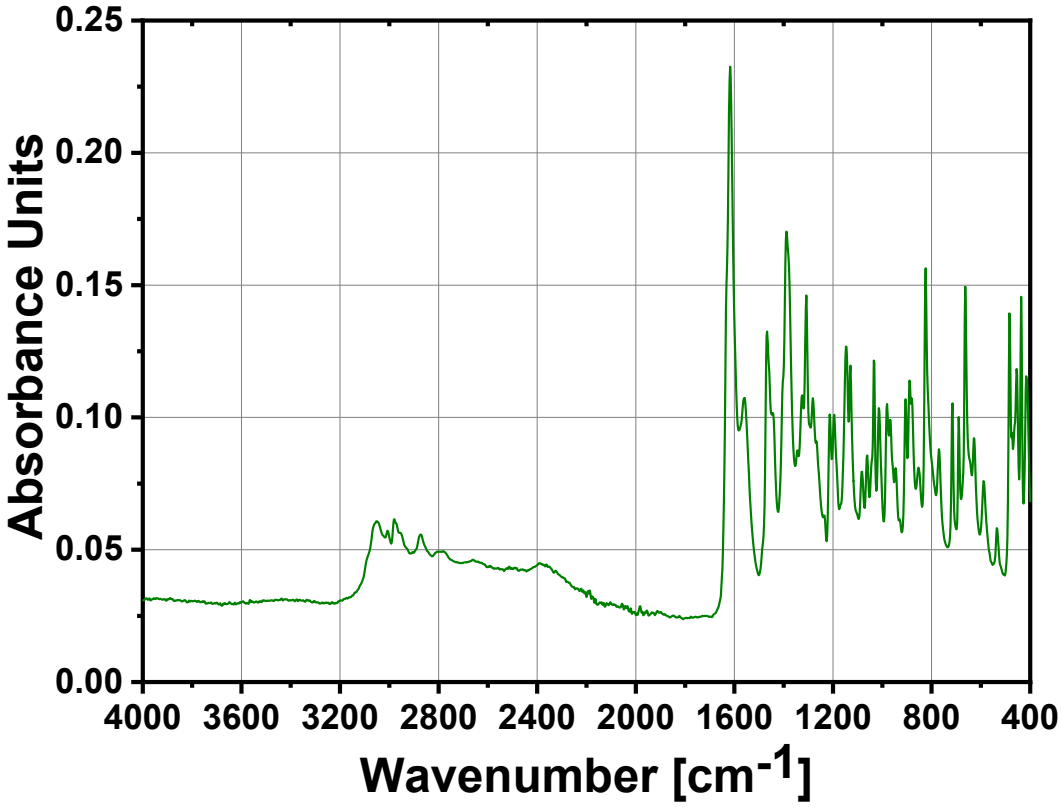

Figure S3: IR-ATR spectrum of (3,4-dichlorobenzyl)-L-proline **(2)**.

1.2 Synthesis of *N*-(2-benzoyl-4-chlorophenyl)-1-(3,4-dichlorobenzyl)pyrrolidine-2-carboxamide (3)

Compound **2** (91.0 g, 0.33 mol, 1 equiv.) was dissolved in chlorobenzene (650 mL) and cooled to 0 °C under nitrogen protection before phosphorus pentachloride PCl_5 (68.71 g, 0.33 mol, 1 equiv.) was added slowly to the solution. The reacting mixture was stirred for 30 min at 0°C and afterwards warmed to 23 °C while further stirring for 2 h to form the corresponding acid chloride. Then 2-amino-5-chlorobenzophenone (76.45 g, 0.33 mol, 1 equiv.) was slowly added and the reaction mixture was kept stirring at 23 °C for 2 h. This reaction was quenched by the addition of MeOH (60 mL) and further stirring for 1 h, leading to the precipitation of crude product. The precipitation was filtered and washed with chlorobenzene (120 mL) and acetone (2 * 300 mL), whereas the filtrated solution was concentrated under reduced pressure leading to further precipitation of crude product. This precipitation was filtered and washed with acetone (2 * 250 mL). Both batches of product were combined and dried *in vacuo* at 45 °C. The crude solid was afterwards washed with MeOH (300mL) for 1 min under gentle stirring, filtered and dried *in vacuo* at 45 °C.

The title compound **3** was obtained as fine white / slightly yellowish needles (128.41 g, 0.26 mol, 79%).

^{1}H NMR (600 MHz, METHANOL-D_4): δ = **7.73 – 7.23** (m, 11H), **4.32 – 4.18** (m, 3H), **3.54 – 3.42** (m, 1H), **2.39 – 2.22** (m, 1H), **2.13 – 2.02** (m, 1H), **1.86 – 1.72** (m, 1H), **1.52 – 1.43** (m, 1H).

^{13}C {1H} NMR (151 MHz, METHANOL-D_4): δ = 194.37, 136.57, 134.14, 133.59, 133.31, 133.03, 132.81, 132.69, 131.55, 131.10, 130.99, 130.55, 129.90, 129.66, 128.35, 125.76, 66.91, 56.50, 54.70, 28.05, 22.48.

IR (ATR): ν = 3172.20, 2951.04, 2864.40, 2732.17, 1705.04, 1660.84, 1610.42, 1535.14, 1495.99, 1463.02, 1446.54, 1386.78, 1275.51, 1254.90, 1238.42, 1209.57, 1032.36, 960.24, 880.83, 818.06, 696.15, 690.30, 665.57, 632.60 cm^{-1}.

Elemental analysis [CHN] (%) = Anal. Calcd for $C_{25}H_{21}Cl_3N_2O_2$ (m: 1.8260 mg): C, 61.56; H, 4.34; N, 5.74. Found: C, 58.31; H, 5.31; N, 4.58.

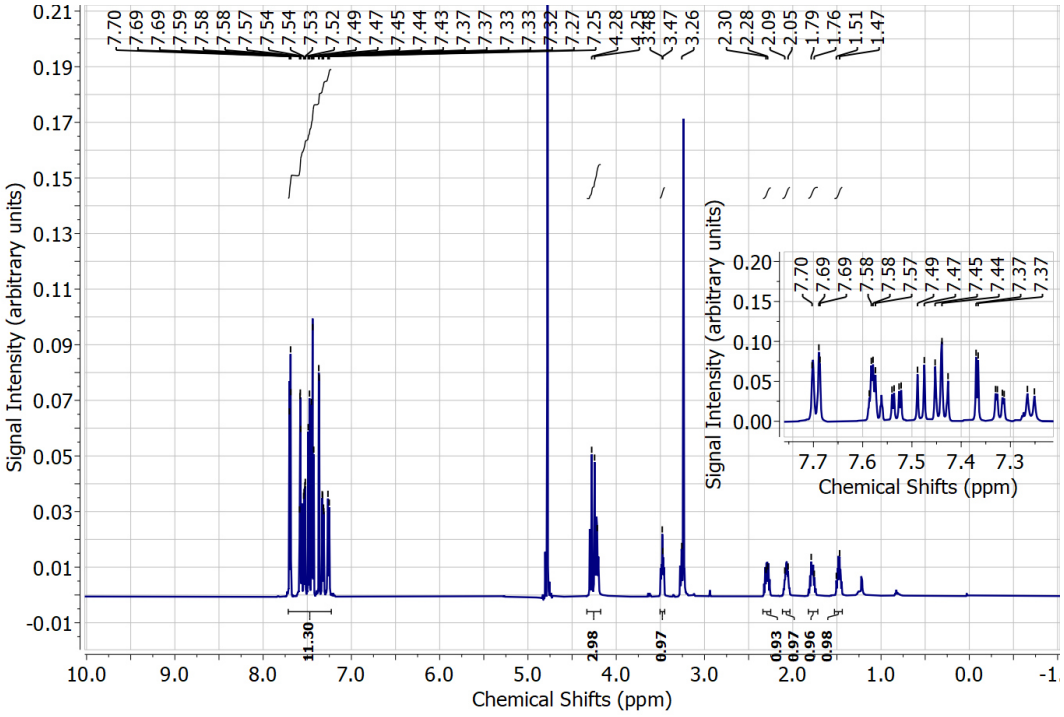

Figure S4: ^{1}H NMR (600 MHz) spectrum of *N*-(2-benzoyl-4-chlorophenyl)-1-(3,4-dichlorobenzyl)pyrrolidine-2-carboxamide **(3)** dissolved in MeOH-d_4.

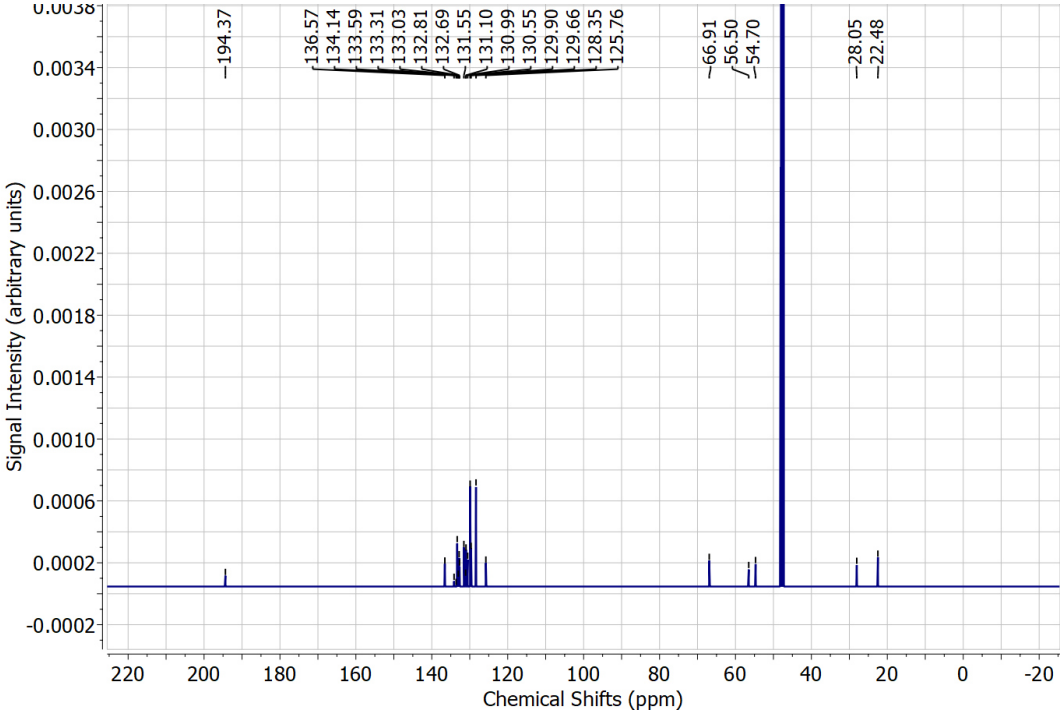

Figure S5: ^{13}C {1H} NMR (151 MHz) spectrum of *N*-(2-benzoyl-4-chlorophenyl)-1-(3,4-dichlorobenzyl)pyrrolidine-2-carboxamide **(3)** dissolved in MeOH-d_4.

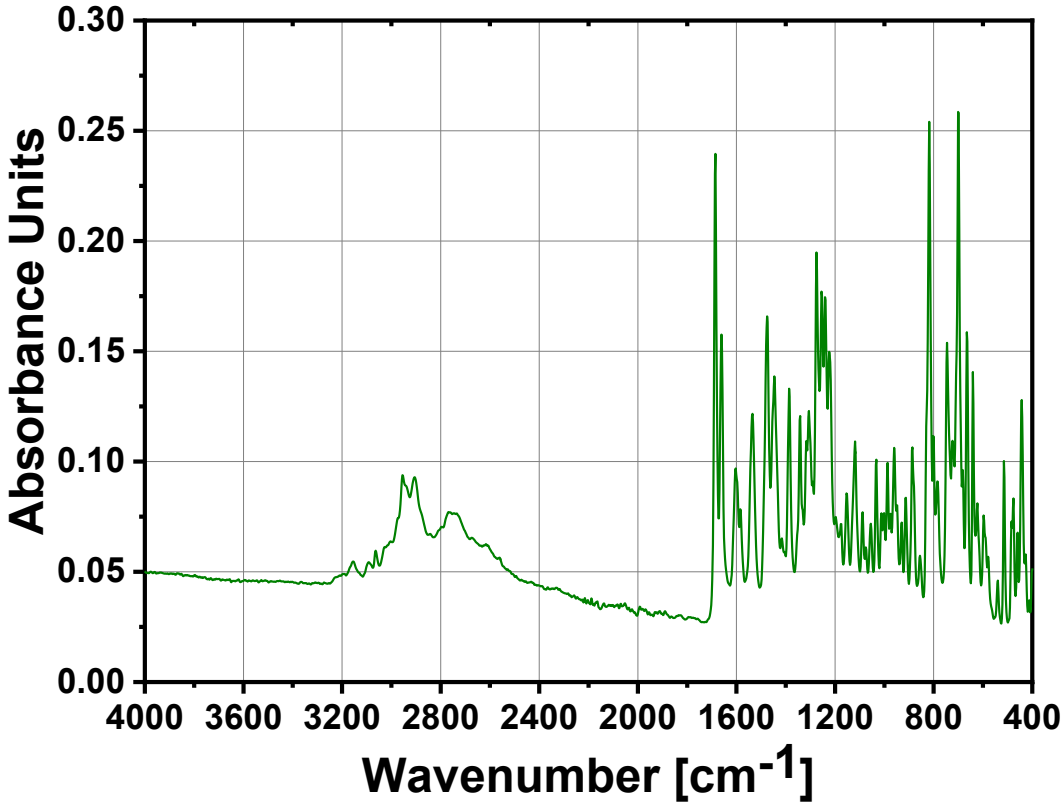

Figure S6: IR-ATR spectrum of *N*-(2-benzoyl-4-chlorophenyl)-1-(3,4-dichlorobenzyl)pyrrolidine-2-carboxamide **(3)**.

1.3 Synthesis of Nickel(II)-[N-[[5-Chloro-2-[[[(*S*)-1-[(3,4dichlorophenyl)methyl]-2-pyrrolidinyl-κN]carbonyl]aminoκN]phenyl]phenylmethylene]-glycinato(2-)-κN, κO] -- Glycine−Ni(II) Ligand Complex (4)

At first, MeOH (1200 mL) was added to a mixture of compound **3** (128.41 g, 0.26 mol, 1 equiv.), nickel acetate tetrahydrate (129.09 g, 0.52 mol, 2 equiv.) and H-Gly-OH (40.0 g, 0.52 mol, 2 equiv.). This green suspension was stirred at 23 °C before 1,8-diazabicyclo[5.4.0]undec-7-ene DBU (175.58 mL, 1.3 mol, 5 equiv.) was slowly added. The reaction mixture was warmed to 75 °C and stirred for 24 h. Afterwards, the reaction was quenched by addition of a 6%-AcOH solution (1300 mL) and further stirring for 3 h. The crude product was filtered, washed with water (850 mL) and a water/methanol-mixture (1:1) (850 mL) and then dried *in vacuo* at 55 °C.

The title compound **4** was obtained as a red solid substance (133.45 g, 0.20 mol, 77%).

^{1}H NMR (600 MHz, METHANOL-D$_4$): δ = **8.79** (d, J = 2.1 Hz, 1H), **8.31** (dd, J = 8.2, 2.2 Hz, 1H), **7.99** (dd, J = 9.2, 1.3 Hz, 1H), **7.68 – 7.60** (m, 1H), **7.59 – 7.52** (m, 3H), **7.27** (d, J = 6.5 Hz, 1H), **7.14** (dd, J = 9.3, 2.6 Hz, 1H), **7.03** (d, J = 7.2 Hz, 1H), **6.68** (d, J = 2.6 Hz, 1H), **4.23** (d, J = 12.6 Hz, 1H), **3.56 – 3.52** (m, 1H), **3.49** (s, 1H), **3.48 – 3.36** (m, 2H), **3.34 – 3.29** (m, 1H) **2.64 – 2.53** (m, 1H), **2.51 – 2.43** (m, 1H), **2.24 – 2.12** (m, 2H).

^{13}C {1H} NMR (151 MHz, METHANOL-D$_4$): δ = 181.83, 179.03, 171.31, 140.45, 136.41, 133.74, 133.58, 132.90, 132.58, 131.52, 131.37, 131.12, 131.01, 129.92, 129.75, 129.34, 126.86, 126.51, 125.87, 125.60, 125.09, 70.99, 62.60, 58.29, 30.55, 23.14.

IR (ATR): ν = 3582.60, 3556.38, 3482.28, 2986.38, 2889.48, 1673.12, 1667.02, 1658.78, 1619.54, 1482.74, 1469.06, 1322.90, 1254.90, 1074.63, 1017.93, 835.23, 832.95, 717.09, 589.33, 549.09, 449.21, 429.39 cm^{-1}.

Elemental analysis [CHN] (%) = Anal. Calcd for $C_{27}H_{22}Cl_3N_3NiO_3$ (m: 2.2480 mg): C, 53.91; H, 3.69; N, 6.99. Found: C, 52.90; H, 4.27; N, 7.06.

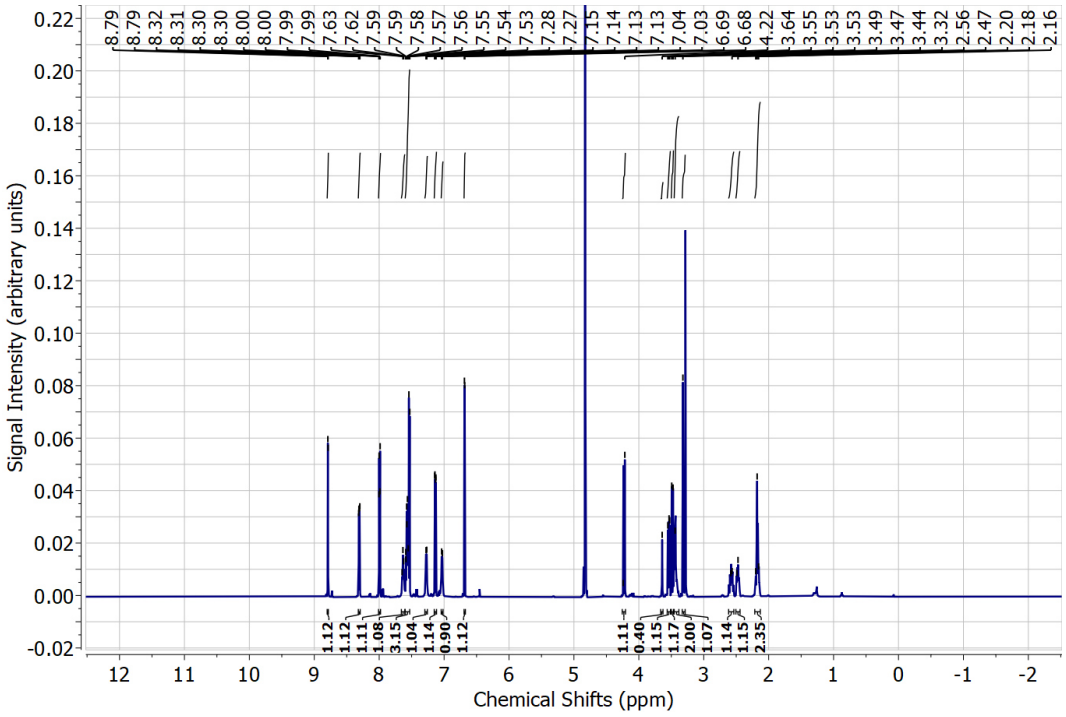

Figure S7: ^{1}H NMR (600 MHz) spectrum of the glycine−Ni(II) ligand complex **4** dissolved in MeOH-d_4.

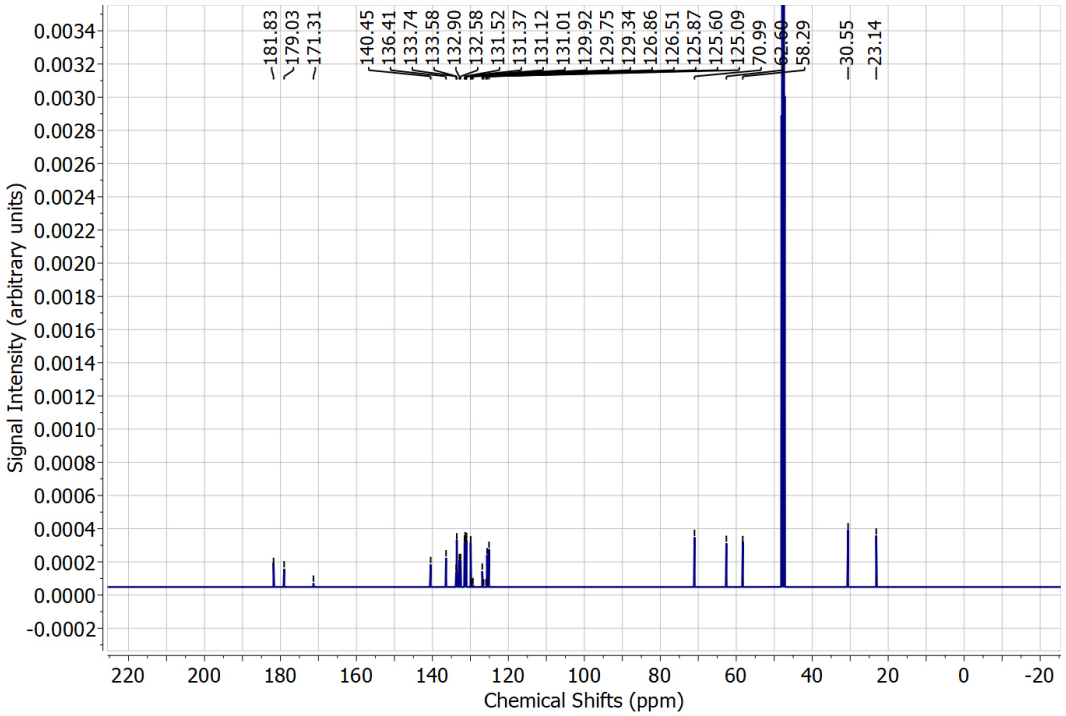

Figure S8: ^{13}C {1H} NMR (151 MHz) spectrum of the glycine−Ni(II) ligand complex **4** dissolved in MeOH-d_4.

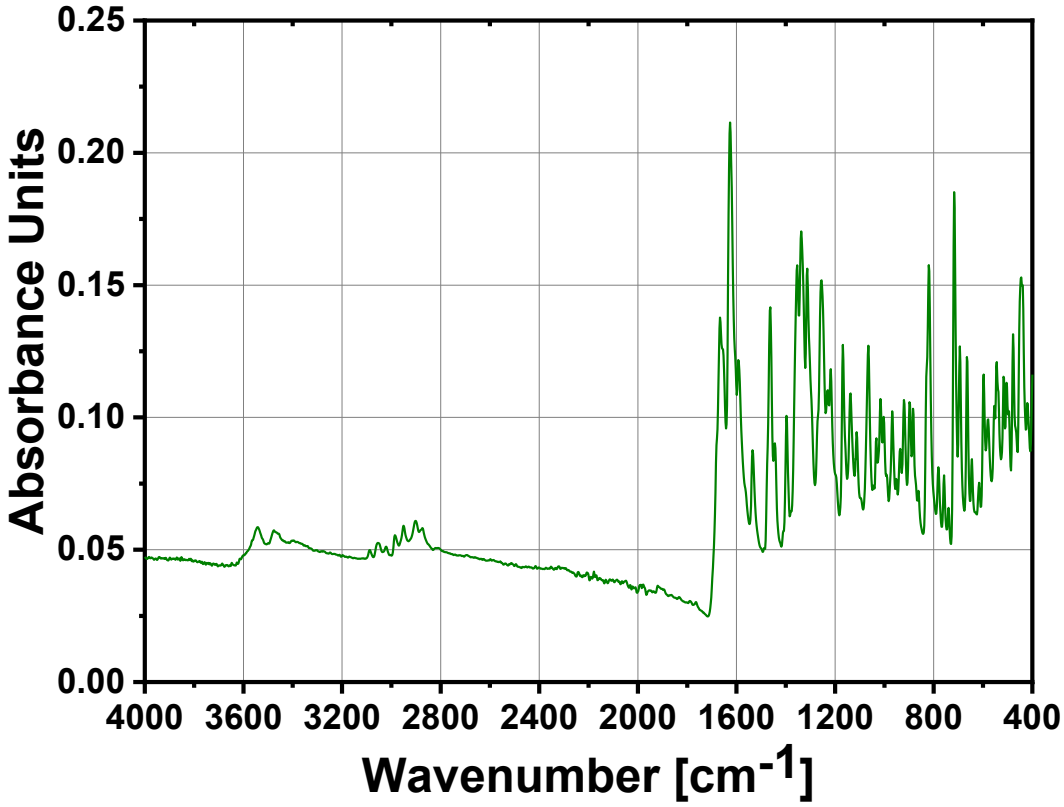

Figure S9: IR-ATR spectrum the glycine−Ni(II) ligand complex **4**.

1.4 Synthesis of the CF_3-CH_2-alkylated Glycine−Ni(II) Ligand Complex 5

The glycine−Ni(II) ligand complex **4** (30.0 g, 0.049 mol, 1 equiv.) and 1,1,1-trifluoro-2-iodoethane (5.20 mL, 0.053 mol, 1.05 equiv.) were dissolved in freshly deoxygenated N,N-dimethylformamide (DMF) (300 mL) and cooled to 0 °C. Afterwards, a solution of KOH (3.0 g, 0.053 mmol, 1.05 equiv.) in freshly deoxygenated MeOH (28 mL) was slowly added under N_2 atmosphere. The reaction mixture was stirred for 3.5 h while warming up to 23 °C. For subsequent quenching, water (110 mL) was added, and the solution was further stirred for 1 h. Afterwards, water (40 mL) was added, and the solution was further stirred for 1 h. The precipitated crude product was filtered, washed with a DMF-water mixture (60 mL) and water (80 mL) and finally dried *in vacuo* at 55 °C.

The title compound **5** was obtained as a red solid substance (26.7 g, 0.039 mol, 80%).

^{1}H NMR (600 MHz, METHANOL-D_4): δ = **8.81** (s, 1H), **8.28** (d, J = 8.2 Hz, 1H), **8.00** (d, J = 9.4 Hz, 1H), **7.72 – 7.61** (m, 2H), **7.59 – 7.55** (m, 1H), **7.52 – 7.50** (m, 1H), **7.49 – 7.45** (m, 1H), **7.12** (d, J = 6.7 Hz, 1H), **7.00** (d, J = 7.8 Hz, 1H), **6.53** (s, 1H), **4.29 – 4.24** (m, 1H), **4.19** (d, J = 12.6 Hz, 2H), **3.61 – 3.54** (m, 1H), **3.41 – 3.36** (m, 3H), **2.68 – 2.51** (m, 2H), **2.33 – 2.25** (m, 1H), **2.23 – 2.14** (m, 2H).

^{13}C {1H} NMR (151 MHz, METHANOL-D_4): δ = 136.59, 133.15, 132.02, 131.15, 131.12, 131.01, 130.83, 130.61, 129.90, 129.83, 129.60, 129.32, 128.70, 128.41, 127.54, 126.85, 125.54, 124.18, 71.34, 67.92, 62.71, 58.38, 58.12, 54.14, 30.59, 30.51, 23.72, 22.56.

^{19}F NMR (565 MHz, METHANOL-D4): δ = -61.57 – -61.62 (m, 3F).

IR (ATR): ν = 3273.86, 2963.70, 2888.52, 1852.89, 1762.14, 1634.05, 1624.29, 1465.77, 1458.90, 1331.37, 1259.02, 1240.48, 1154.47, 1143.63, 1112.72, 1100.48, 831.67, 708.84, 553.68 cm^{-1}.

Elemental analysis [CHN] (%) = Anal. Calcd for $C_{29}H_{23}Cl_3F_3N_3NiO_3$ (m: 1.9100 mg): C, 50.96; H, 3.30; N, 6.15. Found: C, 51.83; H, 3.812; N, 6.402.

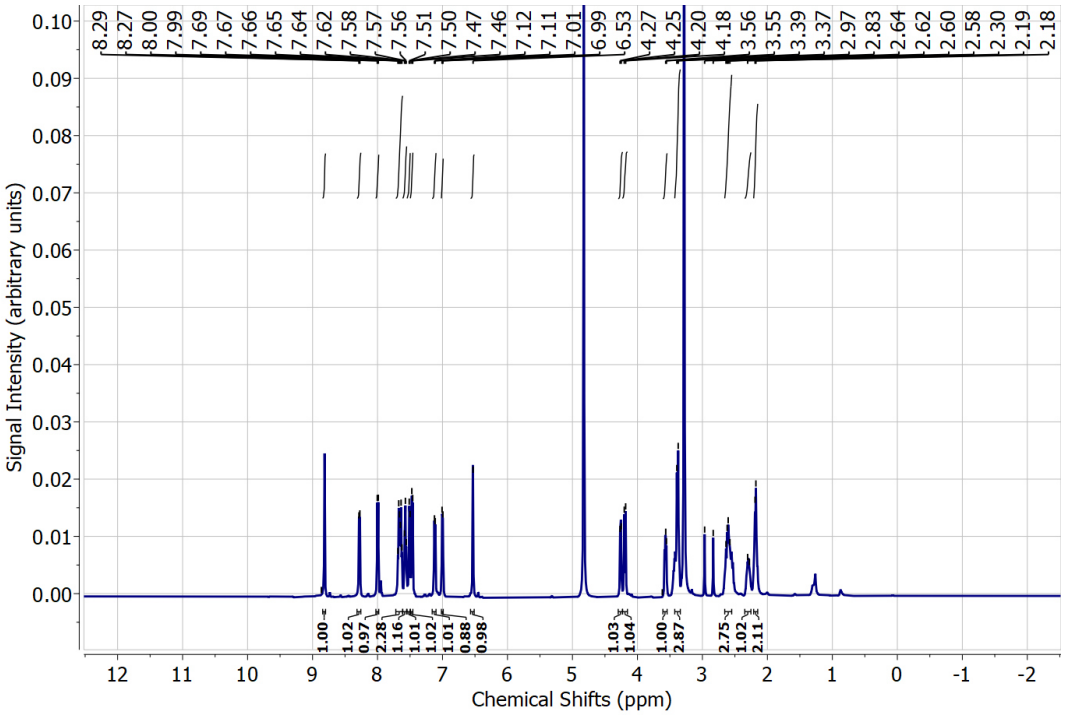

Figure S10: ^{1}H NMR (600 MHz) spectrum of the CF_3-CH_2-alkylated Glycine−Ni(II) ligand complex **5** dissolved in MeOH-d_4.

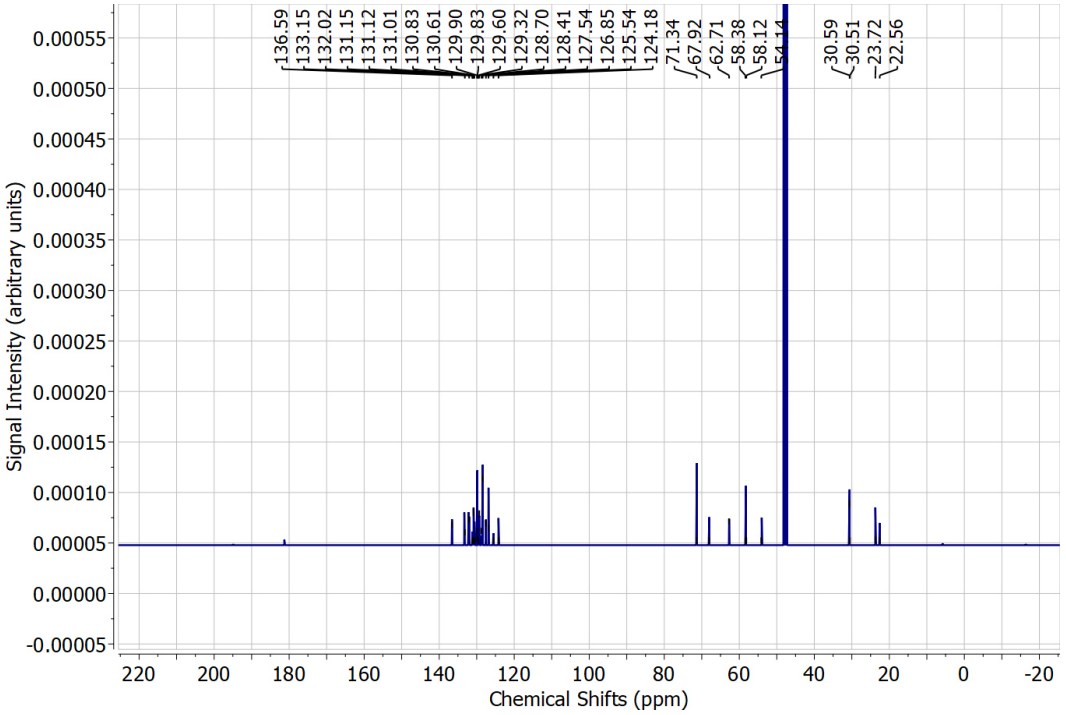

Figure S11: ^{13}C {1H} NMR (151 MHz) spectrum of the CF_3-CH_2-alkylated Glycine−Ni(II) ligand complex **5** dissolved in MeOH-d_4.

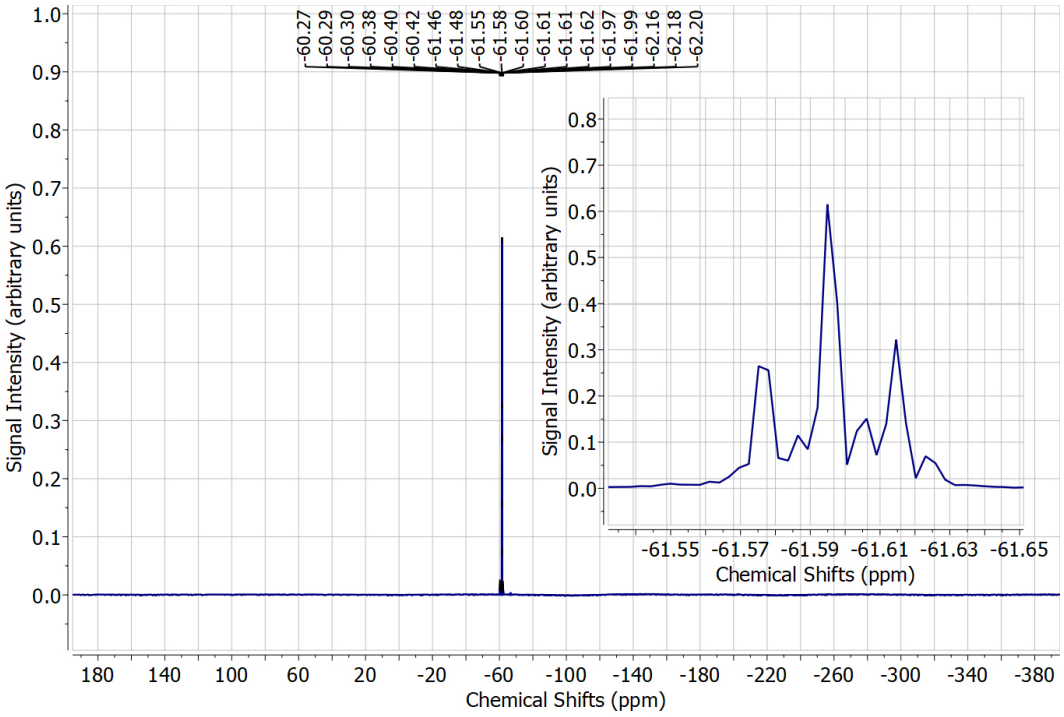

Figure S12: ^{19}F NMR (565 MHz) spectrum of the CF_3-CH_2-alkylated Glycine−Ni(II) ligand complex **5** dissolved in MeOH-d_4.

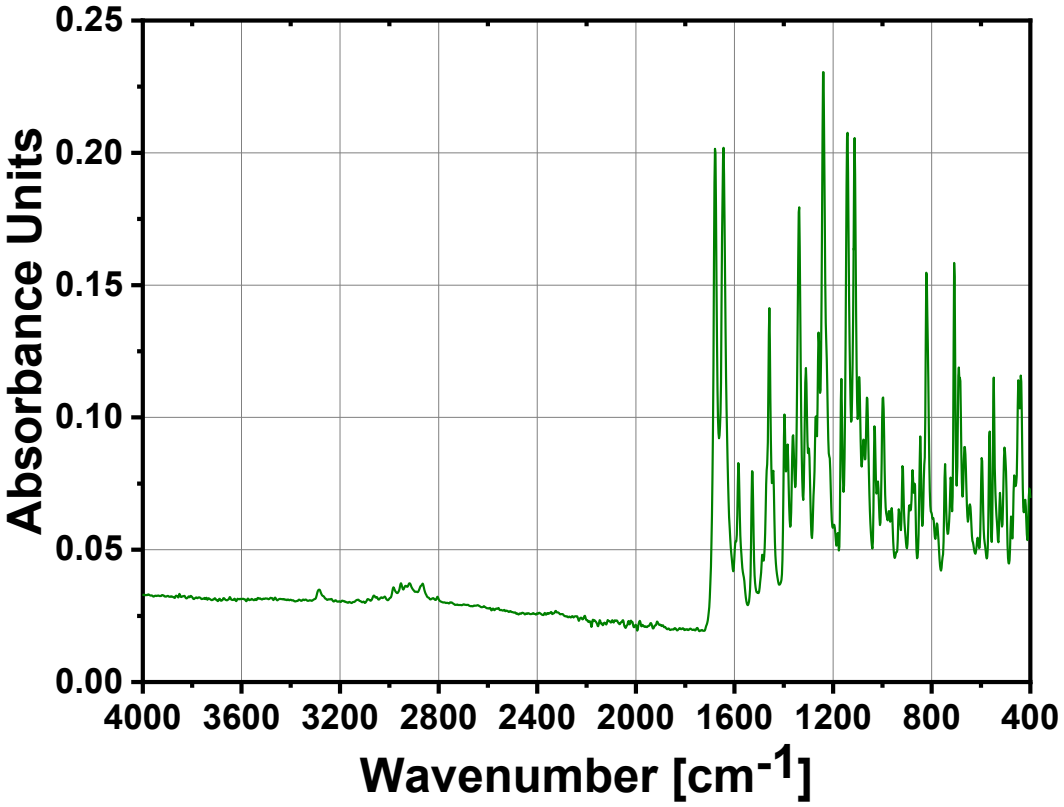

Figure S13: IR-ATR spectrum the CF_3-CH_2-alkylated Glycine−Ni(II) ligand complex **5**.

1.5 Synthesis of Fmoc-TfeGly-OH (6)

Compound **5** (26.7 g, 0.039 mol, 1 equiv.) was dissolved in dimethoxyethane (140 mL) and 3N HCl (85 mL) and heated to 60 °C while stirring for 3h. Then the mixture was filtered and washed with water (50 mL). The combined solutions were concentrated, leading to further precipitation of Ni-ligand residues. These precipitates were filtered and washed with water (25 mL) and the solutions were combined. EDTA-(Na_2) (14.51 g, 0.039 mol, 1 equiv.) in MeCN (85 mL) was added and the mixture was stirred for 2 h at 23 °C. The reaction was quenched by adjusting the pH to 8-8.5 by use of a 48%-NaOH solution. Afterwards, Na_2CO_3 (8.3 g, 0.078 mol, 2 equiv.) was supplemented and Fmoc-OSu (13.15 g, 0.039 mol, 1 equiv.) in THF (70 mL) was added slowly while the reacting mixture was stirred at 23 °C for 20 h. Then, MeCN and THF were removed from the solution under reduced pressure. The aqueous solution was washed with Et_2O (3 * 100 mL) to remove leftovers of Fmoc-OSu. Then, the pH of the solution was adjusted to 2 by using $HCl_{conc.}$ before the aqueous phase was extracted with ethyl acetate (6 * 80 mL). The combined organic phases were dried over Na_2SO_4, filtered, concentrated, and dried *in vacuo* at 55 °C. The crude product (11.86 g) was dissolved in ethyl acetate (60 mL) and toluene (300 mL) and warmed to 75 °C for complete dissolution. Then, the solution was concentrated under reduced pressure and after further addition of toluene (100 mL) concentrated again to a total volume of approximately 200 mL. This solution was left to stand overnight at room temperature, leading to precipitation of pure Fmoc-TfeGly-OH **(6)**. The amino acid was filtered, washed with ice-cold toluene (100 mL) and hexane (100 mL) and then dried *in vacuo* at 55 °C.

The title compound **6** was obtained as a white solid substance (9.18 g, 0.024 mol, 80%).

^{1}H NMR (600 MHz, METHANOL-D_4): δ = **7.73** (d, J = 6.6 Hz, 2H), **7.61** (d, J = 8.9 Hz, 2H), **7.33** (t, J = 7.8 Hz, 2H), **7.25** (t, J = 7.4 Hz, 2H), **4.47** (dd, J = 10.0, 3.5 Hz, 1H), **4.29** (d, J = 7.2 Hz, 2H), **4.16** (t, J = 7.1 Hz, 1H), **2.87 – 2.78** (m, 1H), **2.70 – 2.59** (m, 1H).

^{13}C {1H} NMR (151 MHz, METHANOL-D_4): δ = 171.84, 156.94, 143.86, 143.83, 141.23, 128.61, 127.90, 127.47, 127.12, 126.82, 125.29, 124.94, 119.60, 67.05, 66.89, 34.85, 34.66, 34.47, 34.28.

^{19}F NMR (565 MHz, METHANOL-D4): δ = 65.69 (t, J = 11.1 Hz, 3F).

IR (ATR): ν = 3317.51, 3076.28, 2926.94, 1704.70, 1551.92, 1460.96, 1392.25, 1269.33, 1249.81, 1154.47, 1120.96, 1044.19, 724.84, 618.01, 539.90 cm^{-1}.

Elemental analysis [CHN] (%) = Anal. Calcd for $C_{19}H_{16}F_3NO_4$ (m: 1.8930 mg): C, 60.16; H, 4.25; N, 3.69. Found: C, 60.78; H, 4.86; N, 3.69.

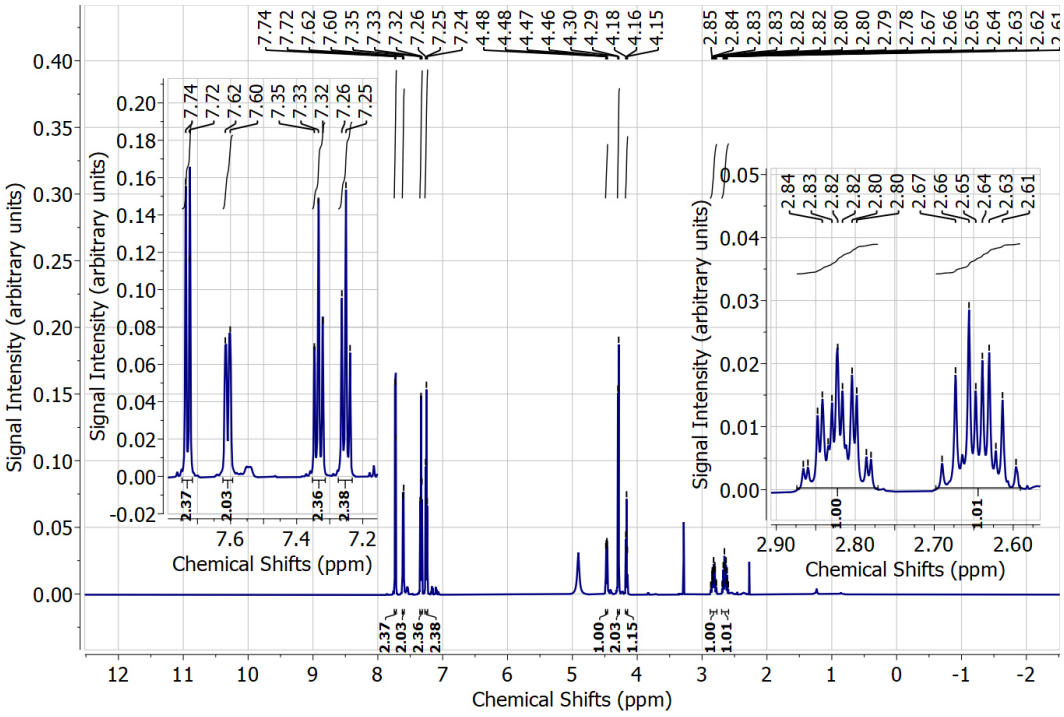

Figure S14: ^{1}H NMR (600 MHz) spectrum of Fmoc-TfeGly-OH **(6)** dissolved in MeOH-d_4.

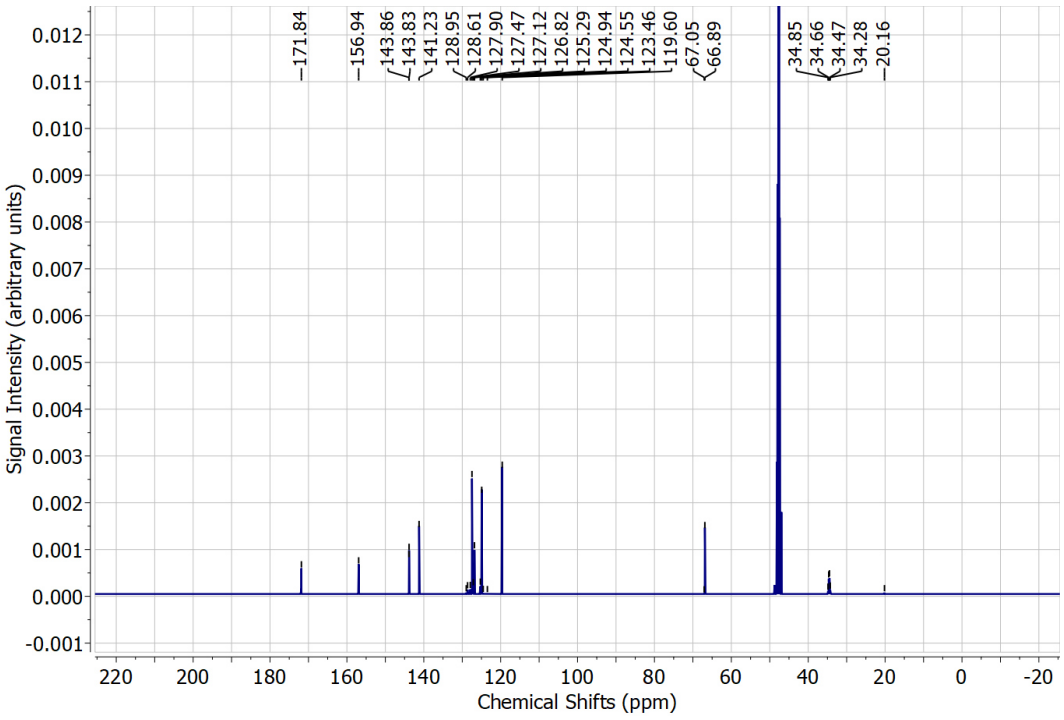

Figure S15: ^{13}C {1H} NMR (151 MHz) spectrum of Fmoc-TfeGly-OH **(6)** dissolved in MeOH-d_4.

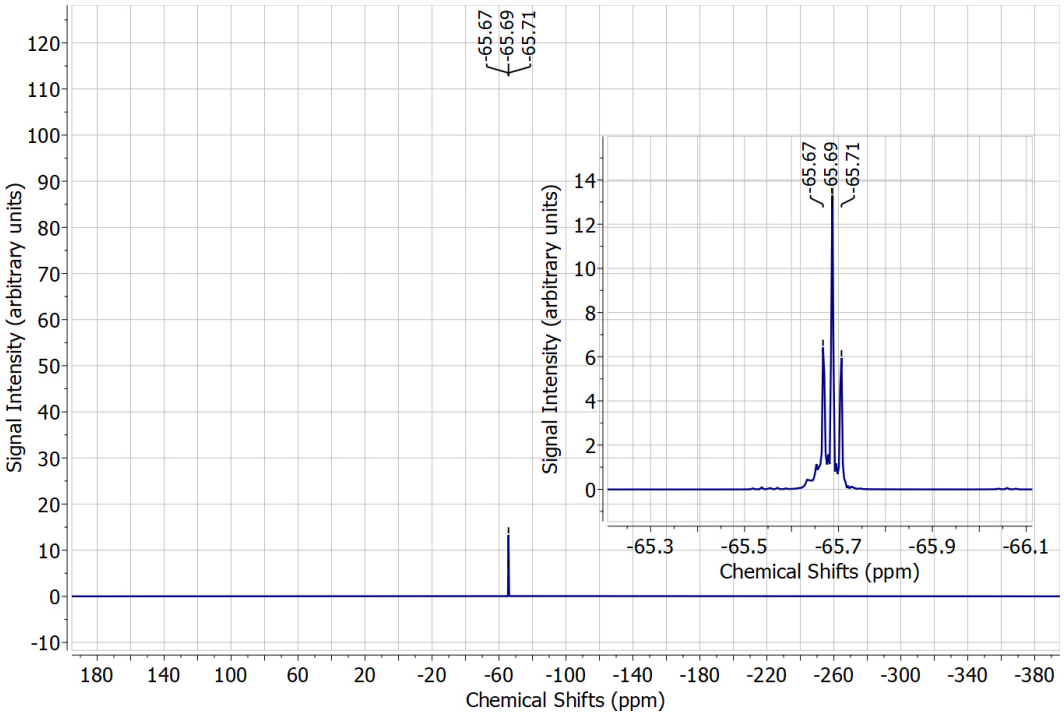

Figure S16: ^{19}F NMR (565 MHz) spectrum of Fmoc-TfeGly-OH **(6)** dissolved in MeOH-d_4.

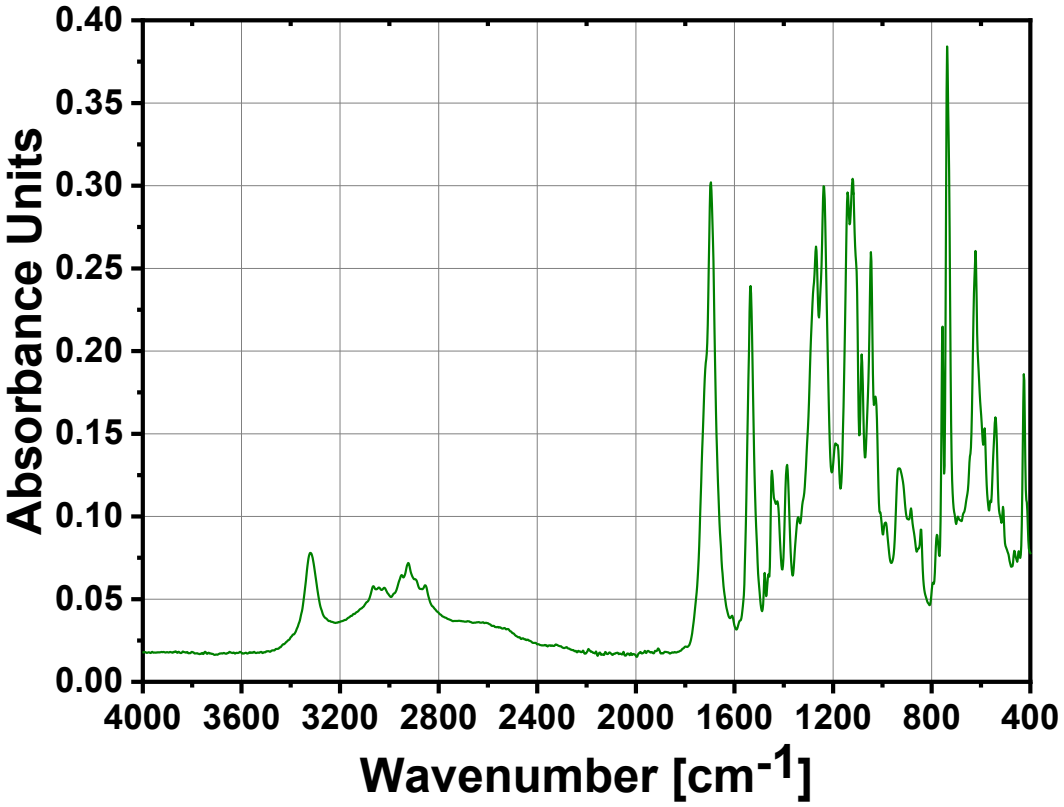

Figure S17: IR-ATR spectrum of Fmoc-TfeGly-OH **(6)**.

2. Fluorinated Fmoc-protected amino acids Fmoc-MfeGly-OH (7) and Fmoc-DfeGly-OH (9)

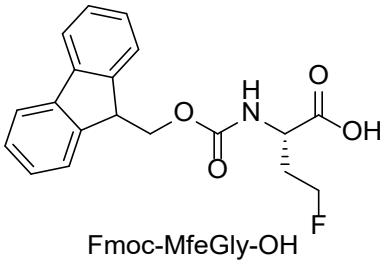

Fmoc-MfeGly-OH

7

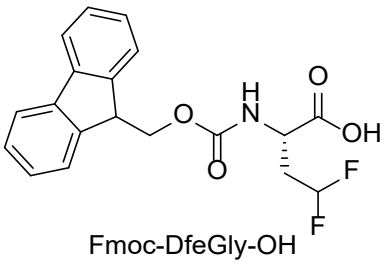

Fmoc-DfeGly-OH

8

Scheme 2: Chemical structures of Fmoc-MfeGly-OH **(9)** and Fmoc-DfeGly-OH **(10).**

The fluorinated Fmoc-protected amino acids Fmoc-MfeGly-OH **(7)** and Fmoc-DfeGly-OH **(8)** were provided by Suvrat Chowdhary & Thomas Hohmann (Freie Universität Berlin, Koksch Group).[11] To validate the chemical nature and purity of these compounds, NMR and IR spectra were recorded and elemental analysis experiments proceeded.

2.1. Characterization of Fmoc-MfeGly-OH (7)

^{1}H NMR (600 MHz, METHANOL-D$_4$): δ = **7.76** (d, J = 7.6 Hz, 2H), **7.64** (t, J = 7.5 Hz, 2H), **7.35** (t, J = 7.5 Hz, 2H), **7.27** (t, J = 7.4 Hz, 2H), **4.56 – 4.40** (m, 2H), **4.37 – 4.31** (m, 2H), **4.31 – 4.25** (m, 1H), **4.19** (t, J = 7.1 Hz, 1H), **2.31 – 2.21** (m, 1H), **2.03 – 1.92** (m, 1H).

^{13}C {1H} NMR (151 MHz, METHANOL-D$_4$): δ = 173.98, 157.36, 143.99, 143.85, 141.27, 127.45, 126.84, 126.81, 124.93, 119.58, 80.59, 79.50, 66.66, 50.51, 32.18, 32.05.

^{19}F NMR (565 MHz, METHANOL-D4): δ = -222.46 – -222.83 (m, 3F)

IR (ATR): ν = 3318.16, 2968.13, 1681.65, 1537.05, 1266.21, 1211.12, 1030.30, 896.68, 760.36, 737.69, 546.06 cm^{-1}.

Elemental analysis [CHN] (%) = Anal. Calcd for $C_{19}H_{18}FNO_4$ (m: 1.4860 mg): C, 66.46; H, 5.28; N, 4.08. Found: C, 65.85; H, 5.926; N, 4.15.

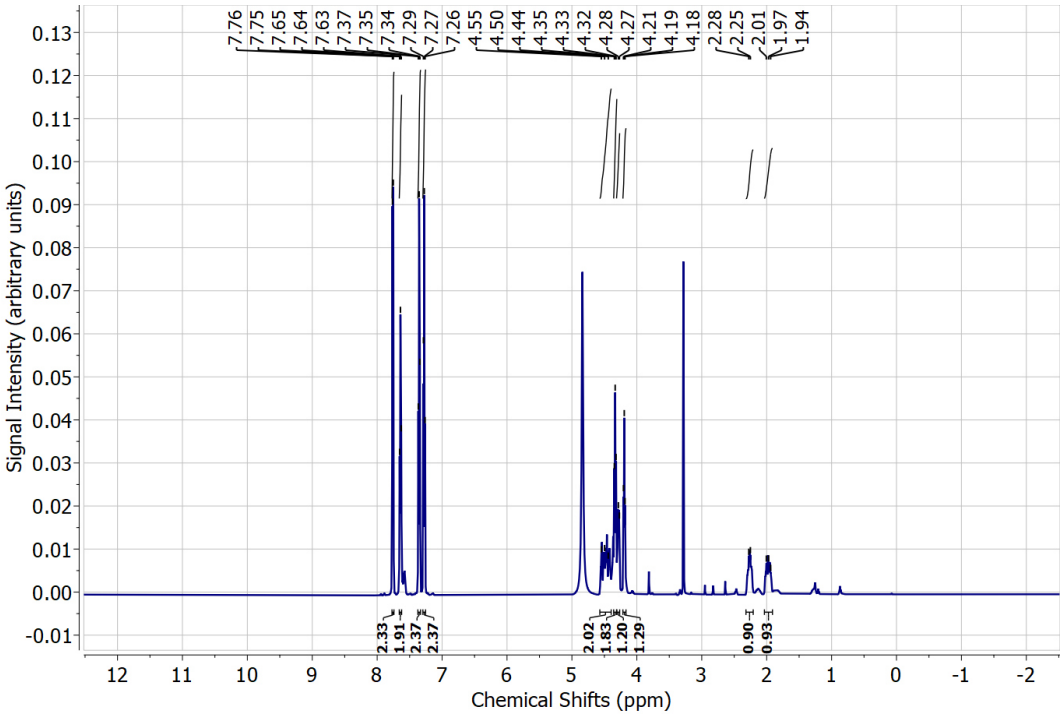

Figure S18: ^{1}H NMR (600 MHz) spectrum of Fmoc-MfeGly-OH **(7)** dissolved in MeOH-d_4.

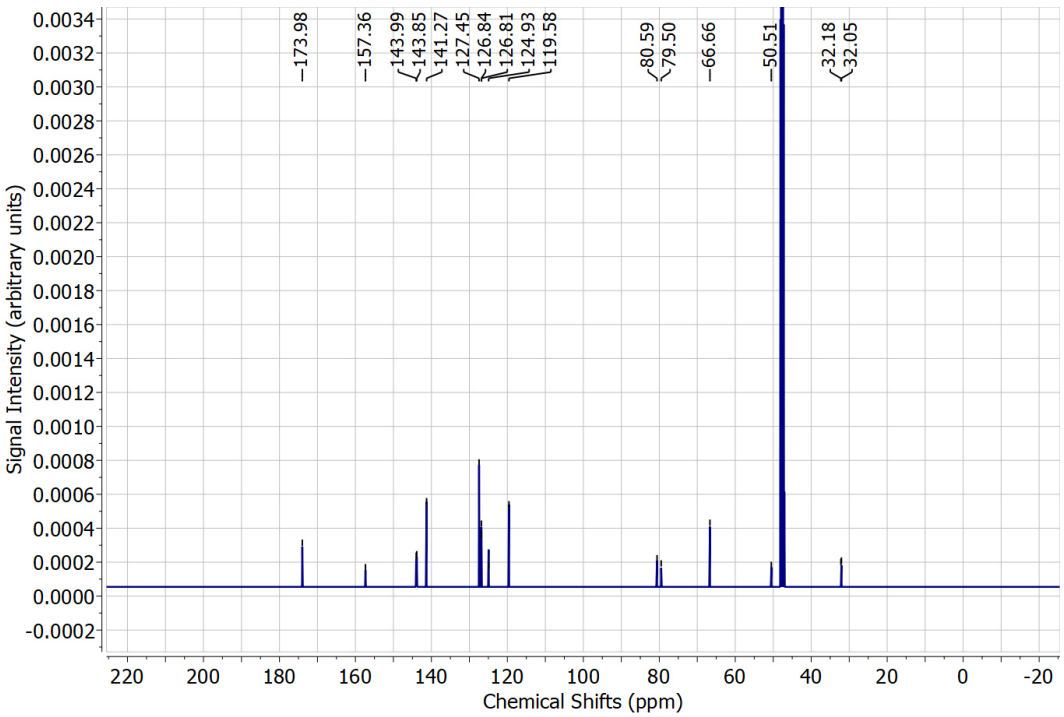

Figure S19: ^{13}C {1H} NMR (151 MHz) spectrum of Fmoc-MfeGly-OH **(7)** dissolved in MeOH-d_4.

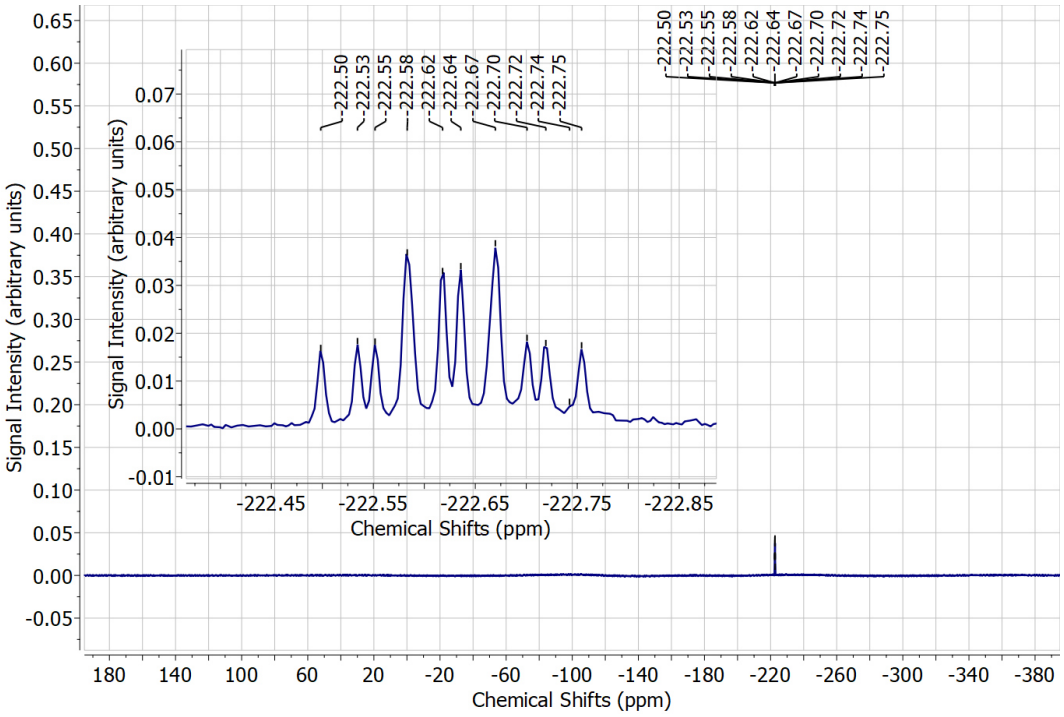

Figure S20: ^{19}F NMR (565 MHz) spectrum of Fmoc-MfeGly-OH **(7)** dissolved in MeOH-d_4.

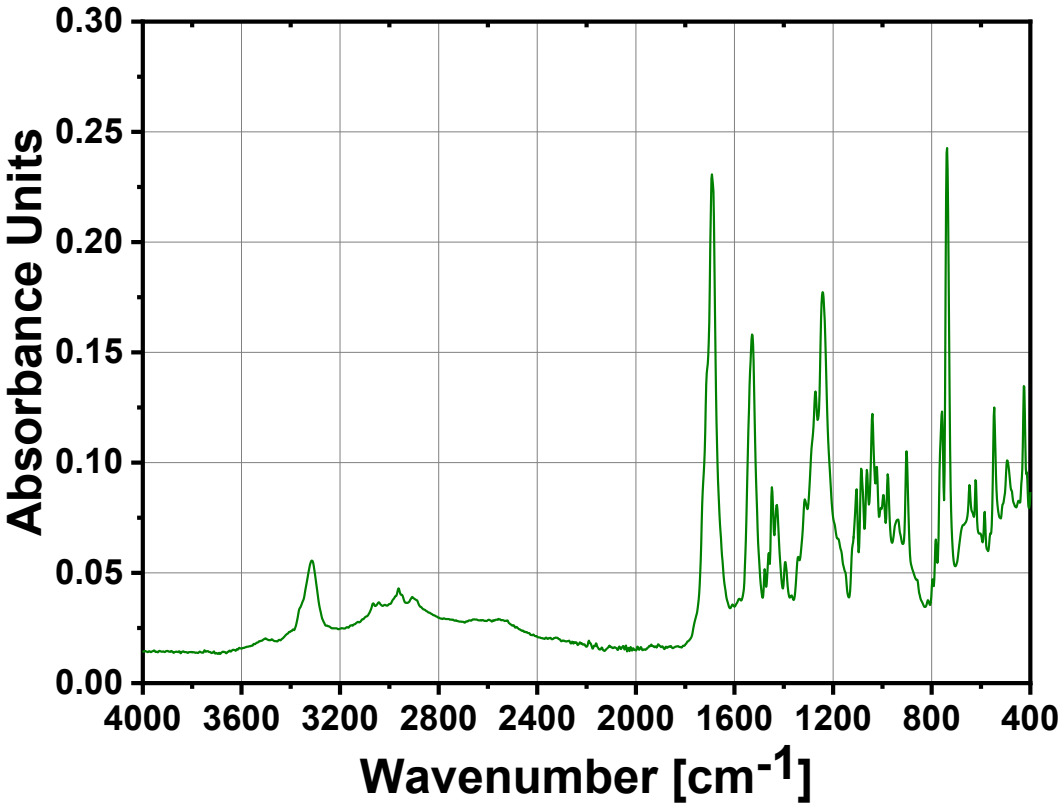

Figure S21: IR-ATR spectrum of Fmoc-MfeGly-OH **(7)**.

2.2. Characterization of Fmoc-DfeGly-OH (8)

^{1}H NMR (600 MHz, METHANOL-D$_4$): δ = **7.77** (d, J = 7.6 Hz, 2H), **7.67 – 7.62** (m, 2H), **7.36** (t, J = 7.0 Hz, 2H), **7.28** (td, J = 7.4, 1.2 Hz, 2H), **6.03 – 5.81** (m, 1H), **4.41 – 4.31** (m, 2H), **4.35 – 4.27** (m, 1H), **4.20** (t, J = 6.9 Hz, 1H), **2.43 – 2.33** (m, 1H), **2.26 – 2.16** (m, 1H).

^{13}C {1H} NMR (151 MHz, METHANOL-D$_4$): δ = 13C NMR (151 MHz, METHANOL-D4) δ 172.75, 157.13, 143.95, 143.83, 141.28, 127.46, 126.82, 124.92, 119.58, 117.30, 115.72, 66.70, 35.84, 35.69, 35.54, 24.93.

^{19}F NMR (565 MHz, METHANOL-D4): δ = -117.45 – -119.06 (m, 3F).

IR (ATR): ν = 3314.06, 3023.44, 2898.22, 1682.88, 1548.48, 1448.60, 1423.87, 1277.57, 1216.50, 1075.20, 737.69, 531.63 cm^{-1}.

Elemental analysis [CHN] (%) = Anal. Calcd for $C_{19}H_{17}F_2NO_4$ (m: 2.1280 mg): C, 63.16; H, 4.74; N, 3.88. Found: C, 63.38; H, 5.17; N, 3.94.

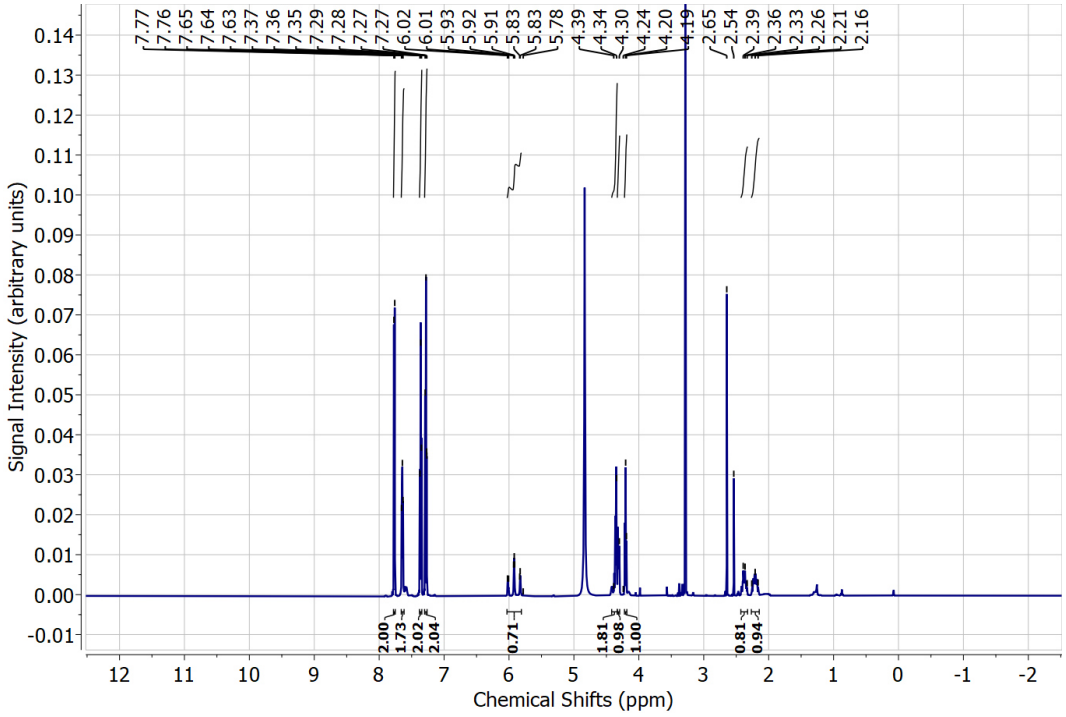

Figure S22: ^{1}H NMR (600 MHz) spectrum of Fmoc-DfeGly-OH **(8)** dissolved in MeOH-d$_4$.

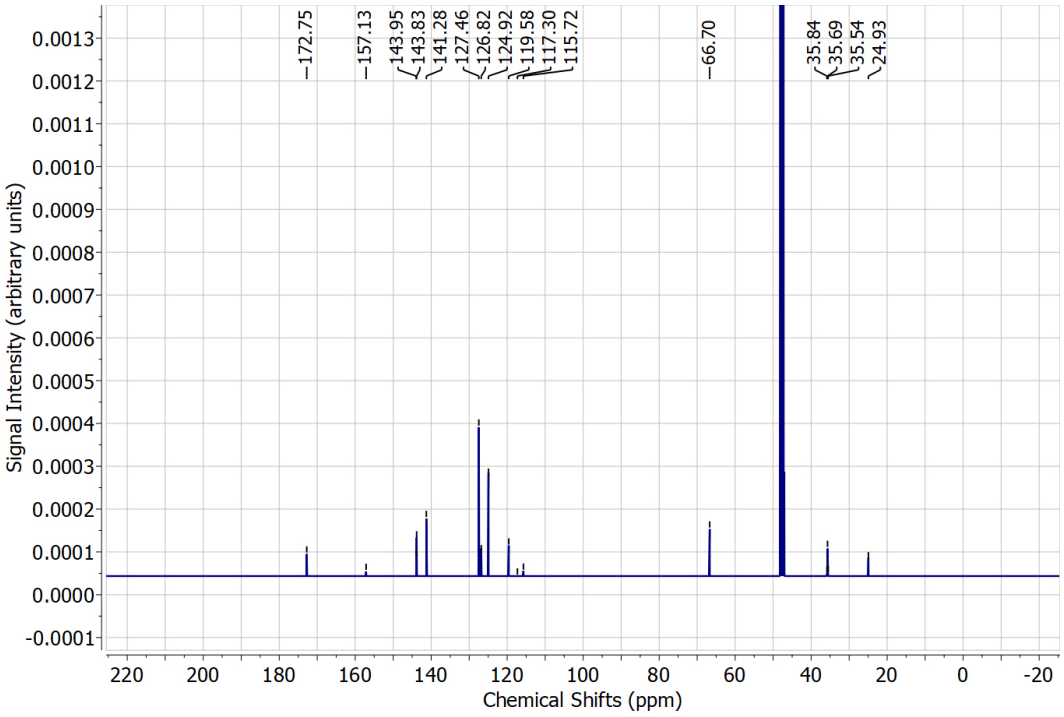

Figure S23: ^{13}C {1H} NMR (151 MHz) spectrum of Fmoc-DfeGly-OH **(8)** dissolved in MeOH-d_4.

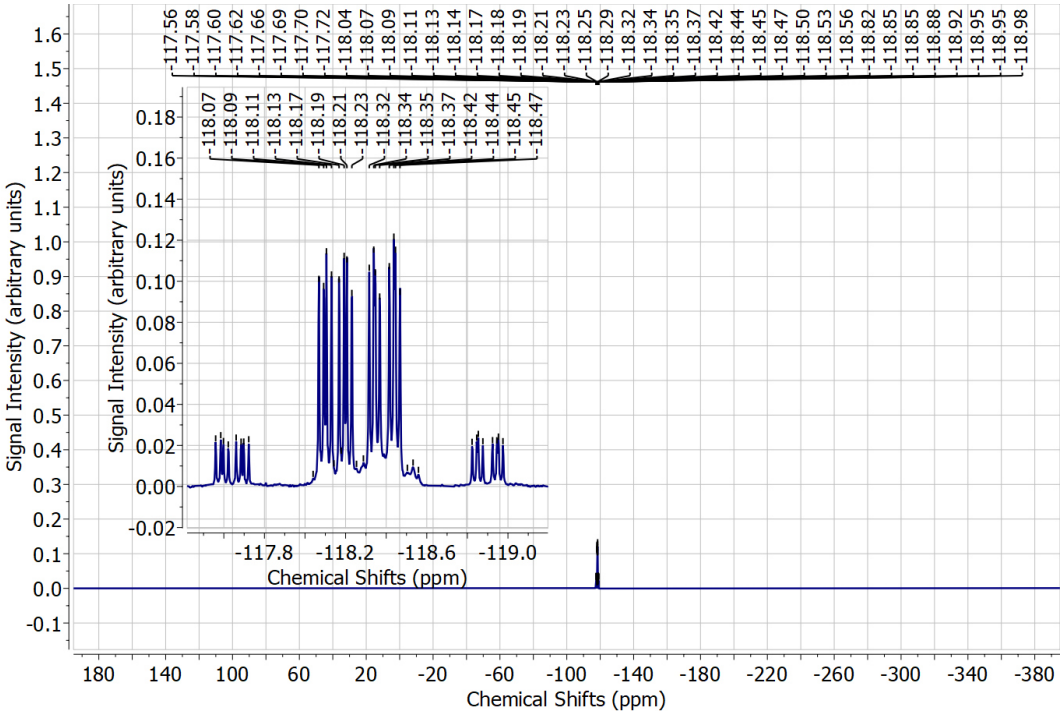

Figure S24: ^{19}F NMR (565 MHz) spectrum of Fmoc-DfeGly-OH **(8)** dissolved in MeOH-d_4.

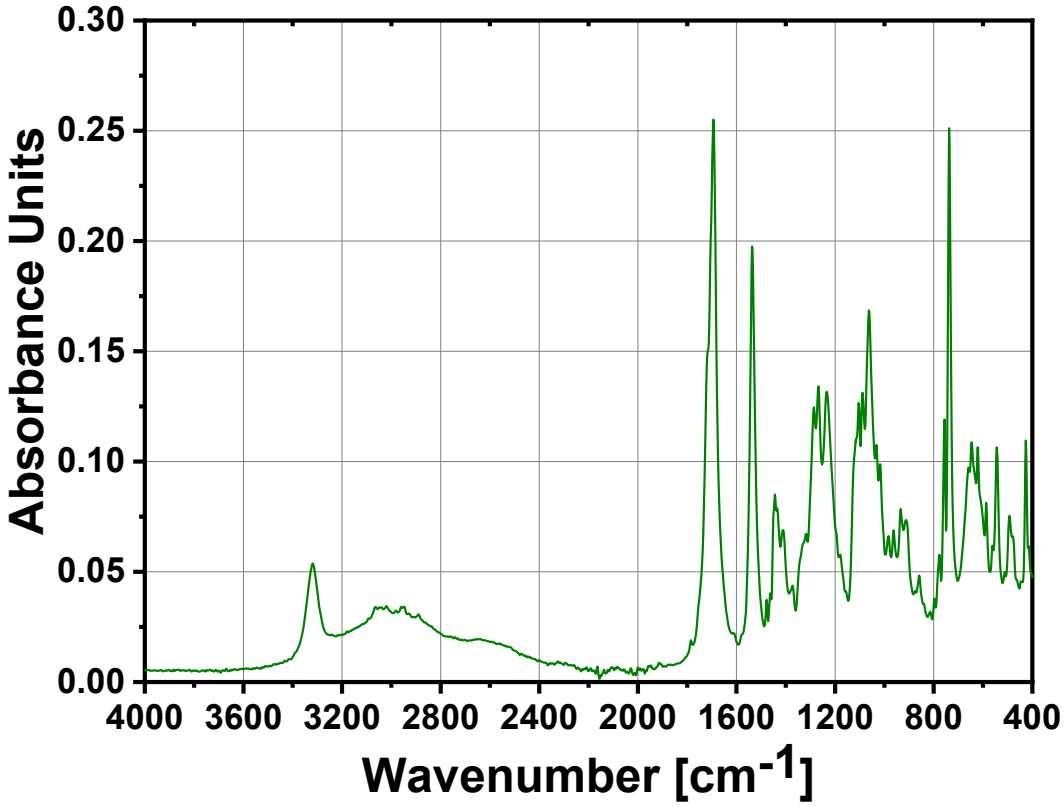

Figure S25: IR-ATR spectrum Fmoc-DfeGly-OH **(8)**.

3. Peptide Synthesis: Selected HPLC chromatograms of crude peptides after SPPS

In this chapter, HPLC chromatograms of crude peptide samples after solid-phase peptide synthesis are presented. This is intended to give an impression about the outcome of overall peptide synthesis. All HPLC chromatograms were **directly exported** from the HPLC systems. (**VWR Chromaster 600 bar** or **Hitachi Primaide**) using EZ Chrom ELITE software (version 3.3.2, Agilent).

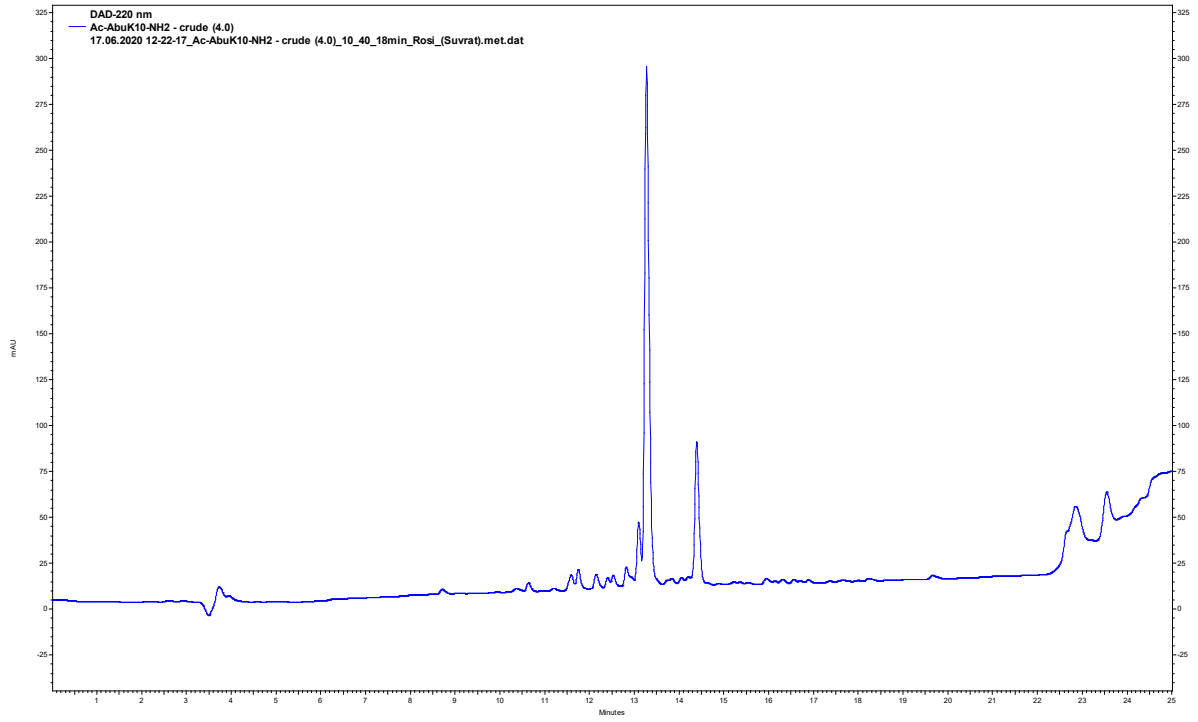

Figure S26: Crude HPLC chromatogram of peptide sequence **AbuK10** (**HPLC:** Chromaster 600 bar – Method: **(A)** H_2O + 0.1% TFA / **(B)** ACN + 0.1% TFA – 10% **(B)** → 40% **(B)** in 18 min. UV detection occurred at 220 nm.

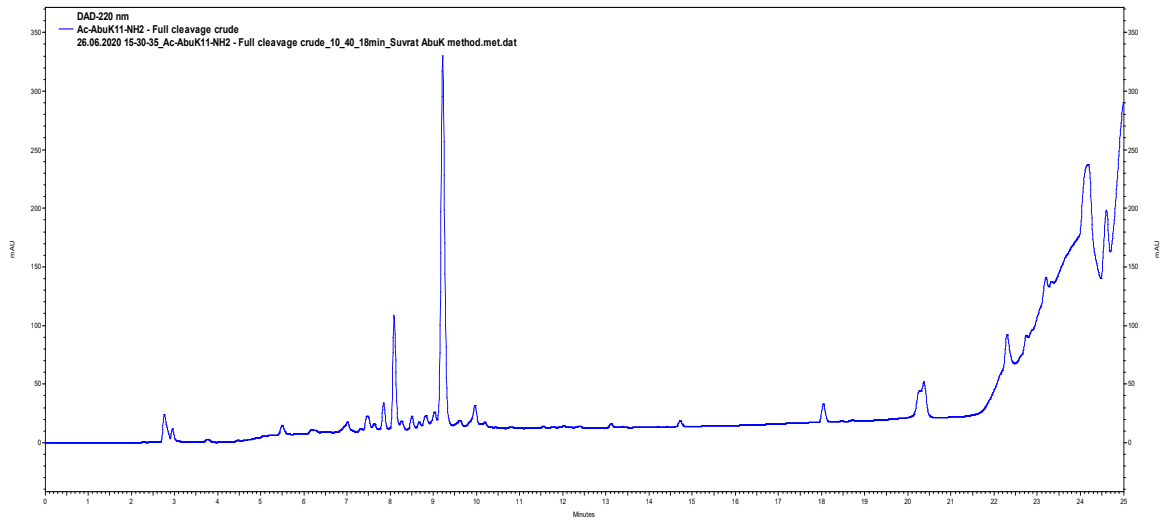

Figure S27: Crude HPLC chromatogram of peptide sequence **AbuK11** (**HPLC:** Hitachi Primaide – Method: **(A)** H_2O + 0.1% TFA / **(B)** ACN + 0.1% TFA – 10% **(B)** → 40% **(B)** in 18 min. UV detection occurred at 220 nm.

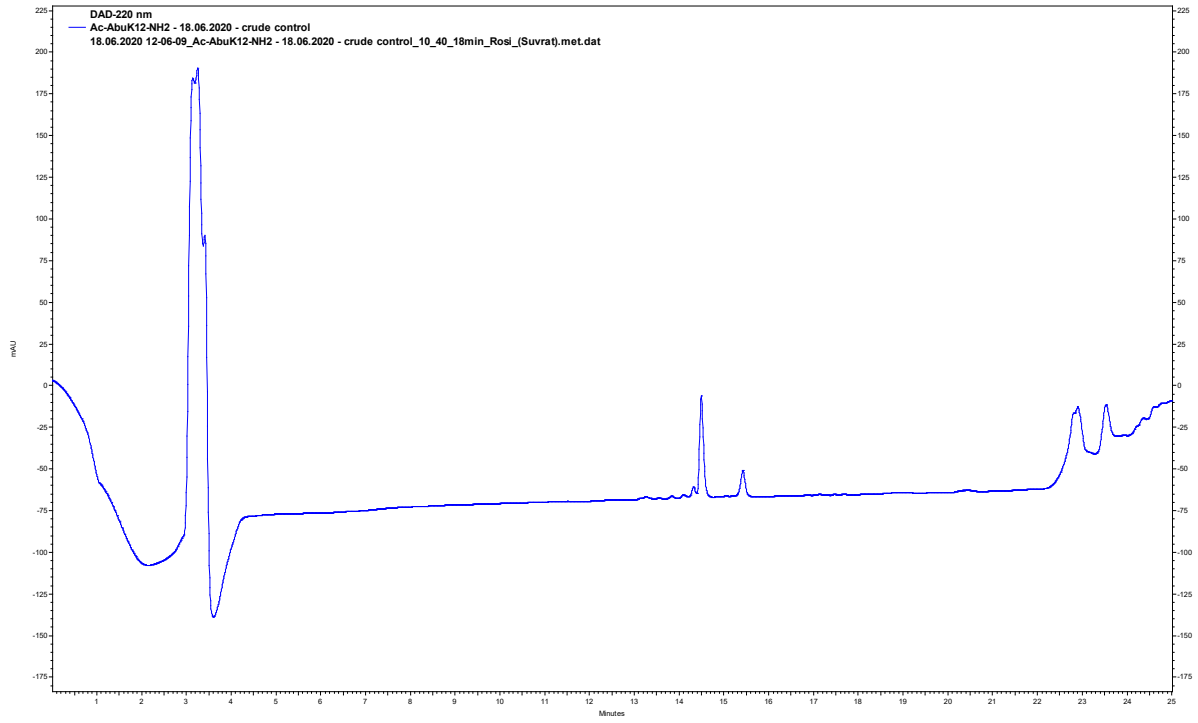

Figure S28: Crude HPLC chromatogram of peptide sequence **AbuK12** (**HPLC:** Chromaster 600 bar – Method: **(A)** H_2O + 0.1% TFA / **(B)** ACN + 0.1% TFA – 10% **(B)** → 40% **(B)** in 18 min. UV detection occurred at 220 nm.

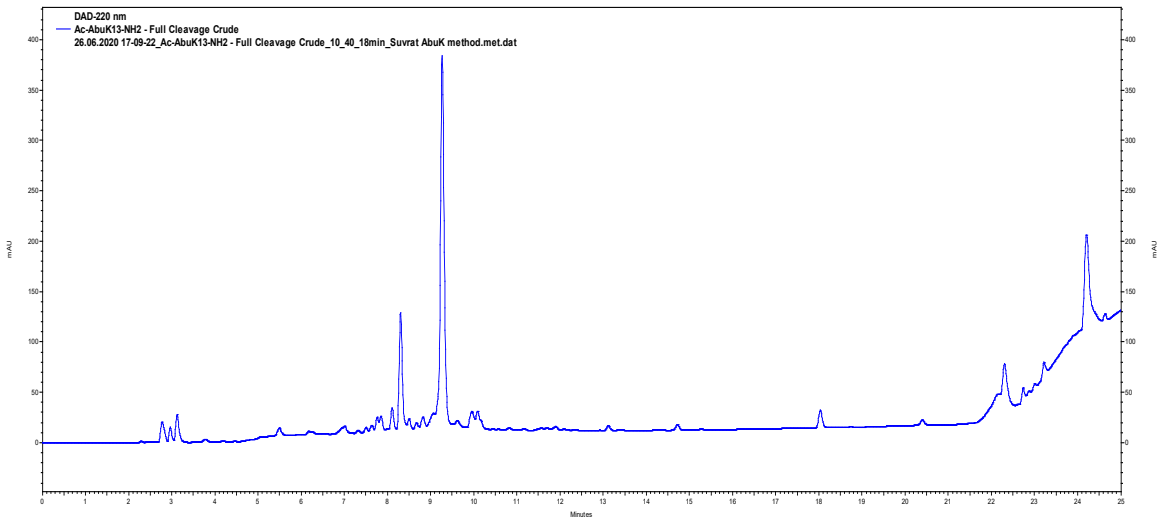

Figure S29: Crude HPLC chromatogram of peptide sequence **AbuK13** (**HPLC:** Hitachi Primaide – Method: **(A)** H_2O + 0.1% TFA / **(B)** ACN + 0.1% TFA – 10% **(B)** → 40% **(B)** in 18 min. UV detection occurred at 220 nm.

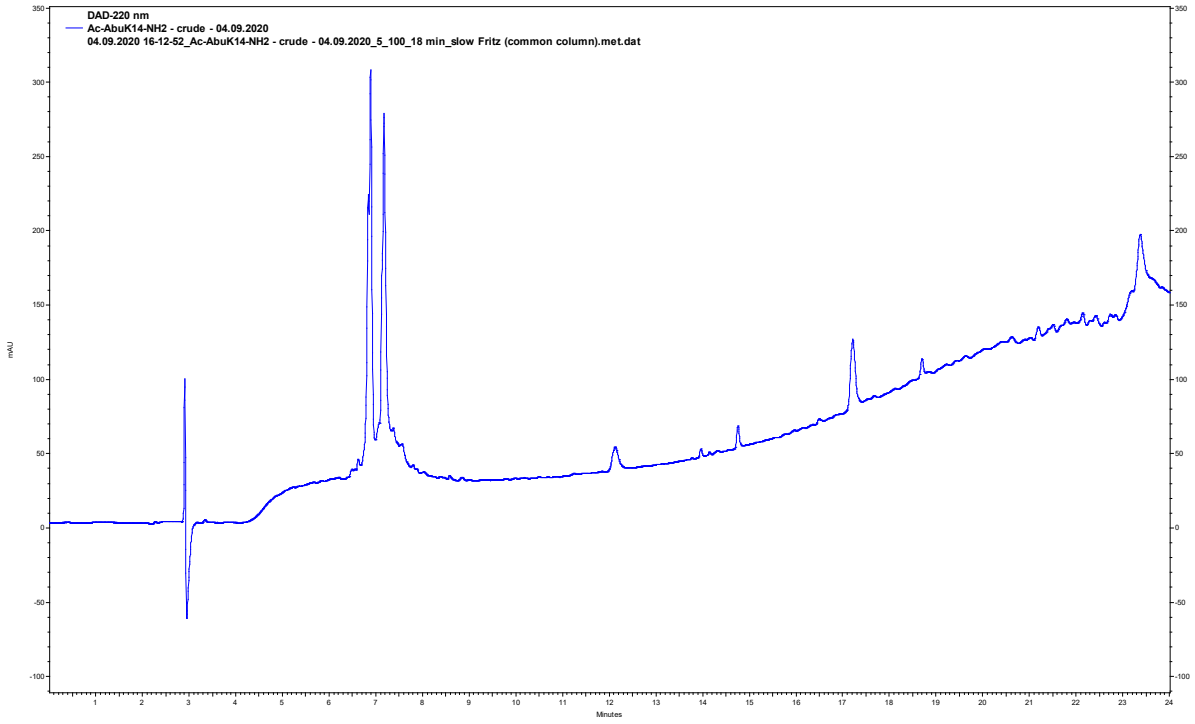

Figure S30: Crude HPLC chromatogram of peptide sequence **AbuK14** (**HPLC:** Chromaster 600 bar – Method: **(A)** H_2O + 0.1% TFA / **(B)** ACN + 0.1% TFA – 5% **(B)** → 100% **(B)** in 18 min. UV detection occurred at 220 nm.

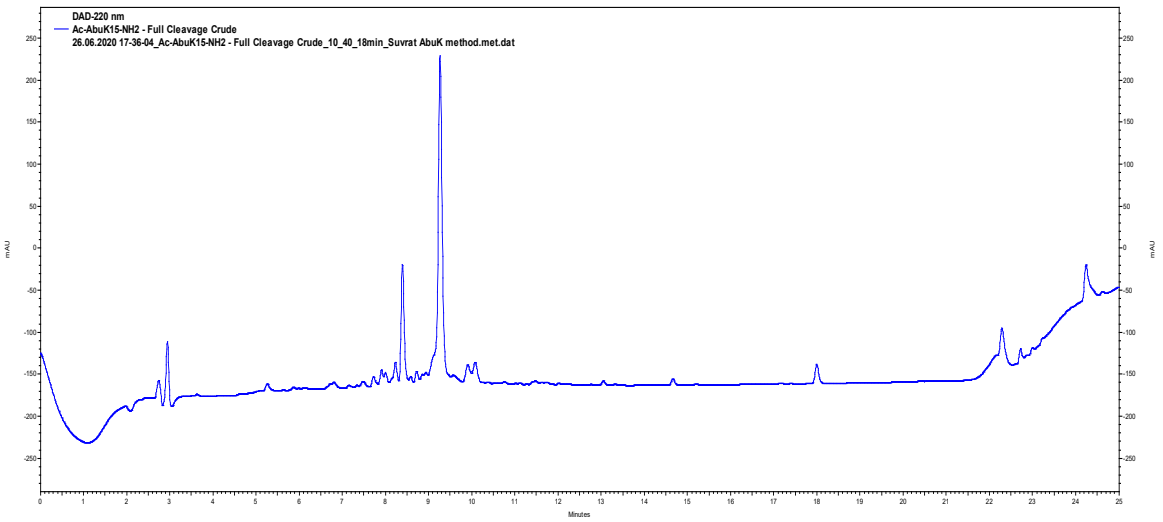

Figure S31: Crude HPLC chromatogram of peptide sequence **AbuK15** (**HPLC:** Hitachi Primaide – Method: **(A)** H_2O + 0.1% TFA / **(B)** ACN + 0.1% TFA – 10% **(B)** → 40% **(B)** in 18 min. UV detection occurred at 220 nm.

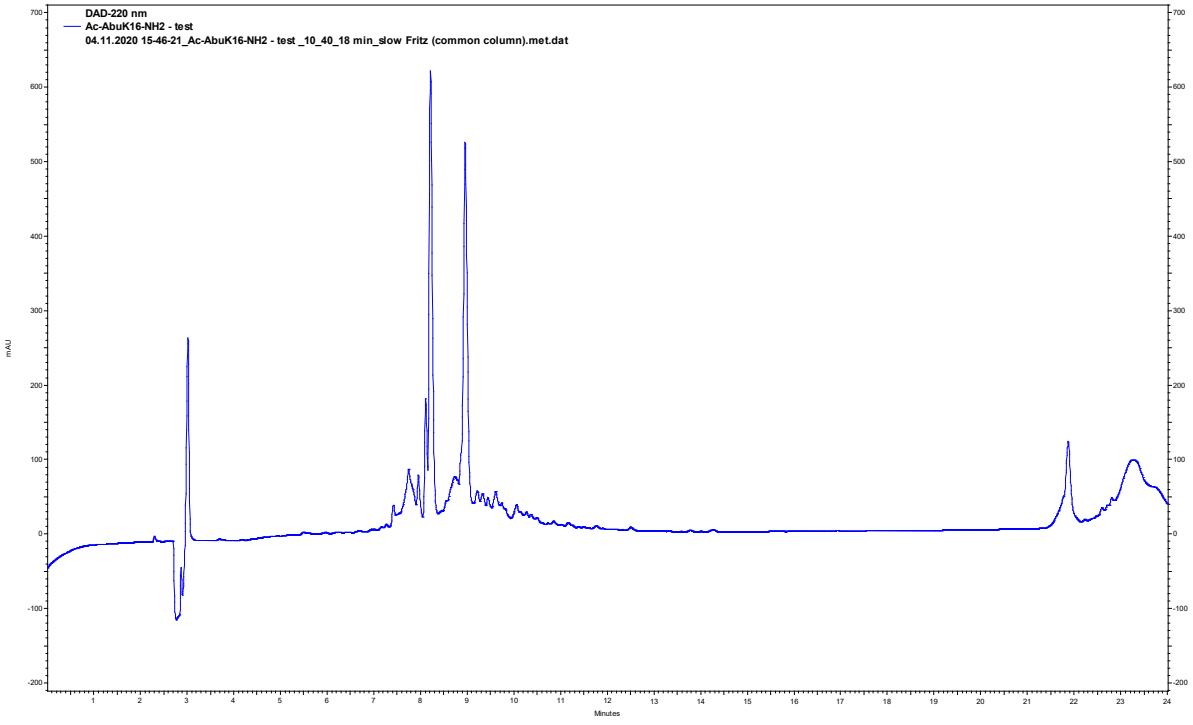

Figure S32: Crude HPLC chromatogram of peptide sequence **AbuK16** (**HPLC:** Chromaster 600 bar – Method: **(A)** H_2O + 0.1% TFA / **(B)** ACN + 0.1% TFA – 10% **(B)** → 40% **(B)** in 18 min. UV detection occurred at 220 nm.

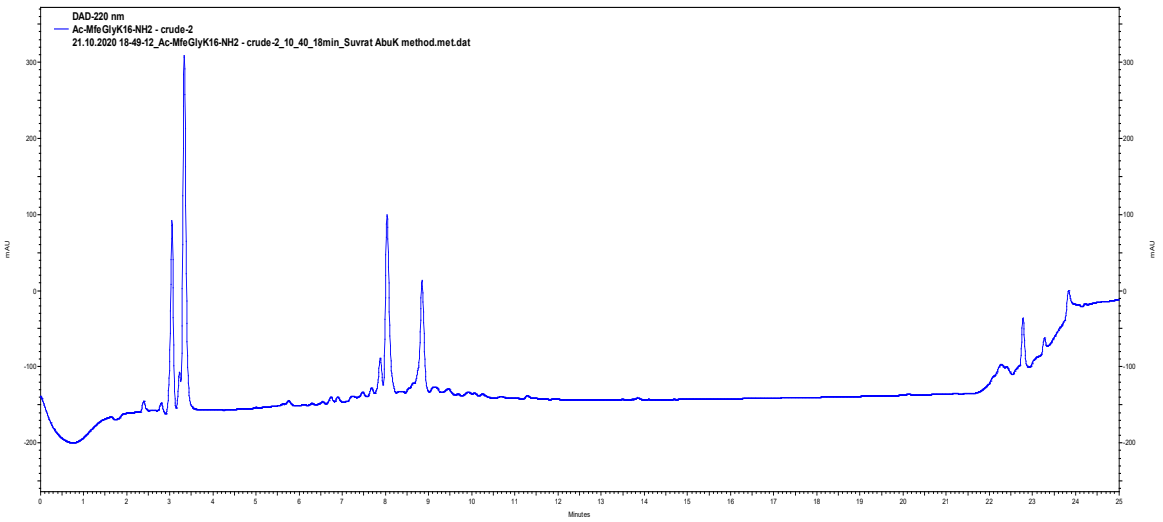

Figure S33: Crude HPLC chromatogram of peptide sequence **MfeGlyK16** (**HPLC:** Hitachi Primaide – Method: **(A)** H_2O + 0.1% TFA / **(B)** ACN + 0.1% TFA – 10% **(B)** → 40% **(B)** in 18 min. UV detection occurred at 220 nm.

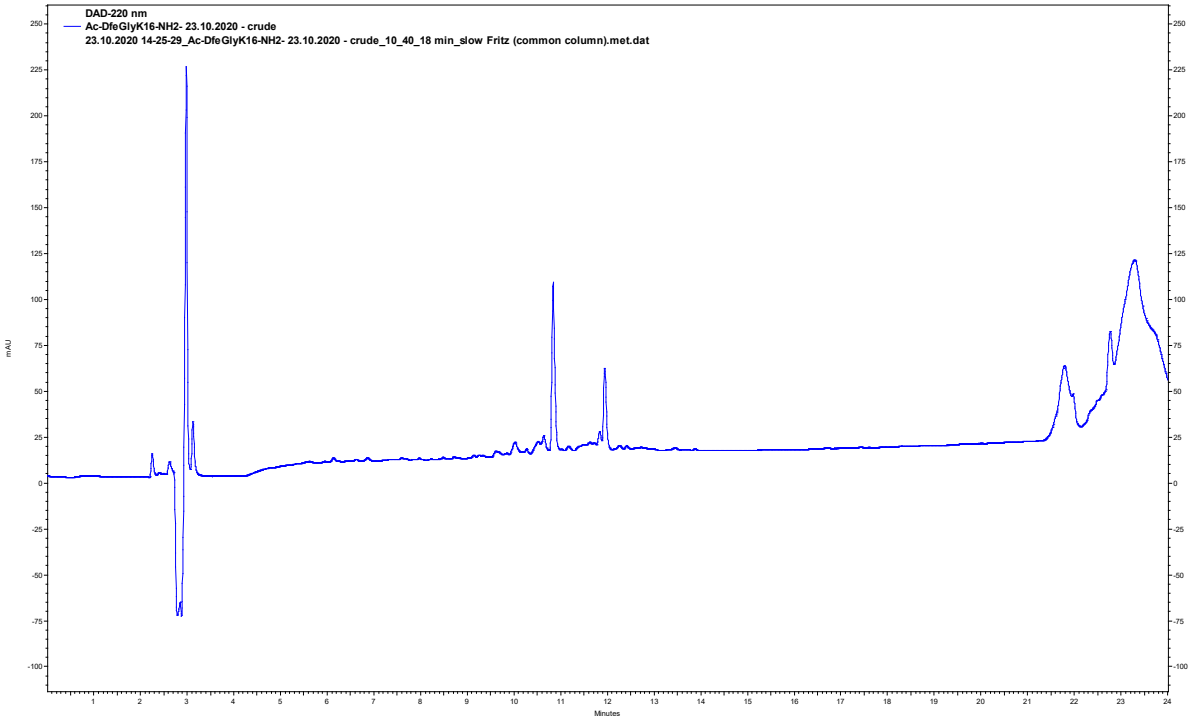

Figure S34: Crude HPLC chromatogram of peptide sequence **DfeGlyK16** (**HPLC:** Chromaster 600 bar – Method: **(A)** H_2O + 0.1% TFA / **(B)** ACN + 0.1% TFA – 10% **(B)** → 40% **(B)** in 18 min. UV detection occurred at 220 nm.

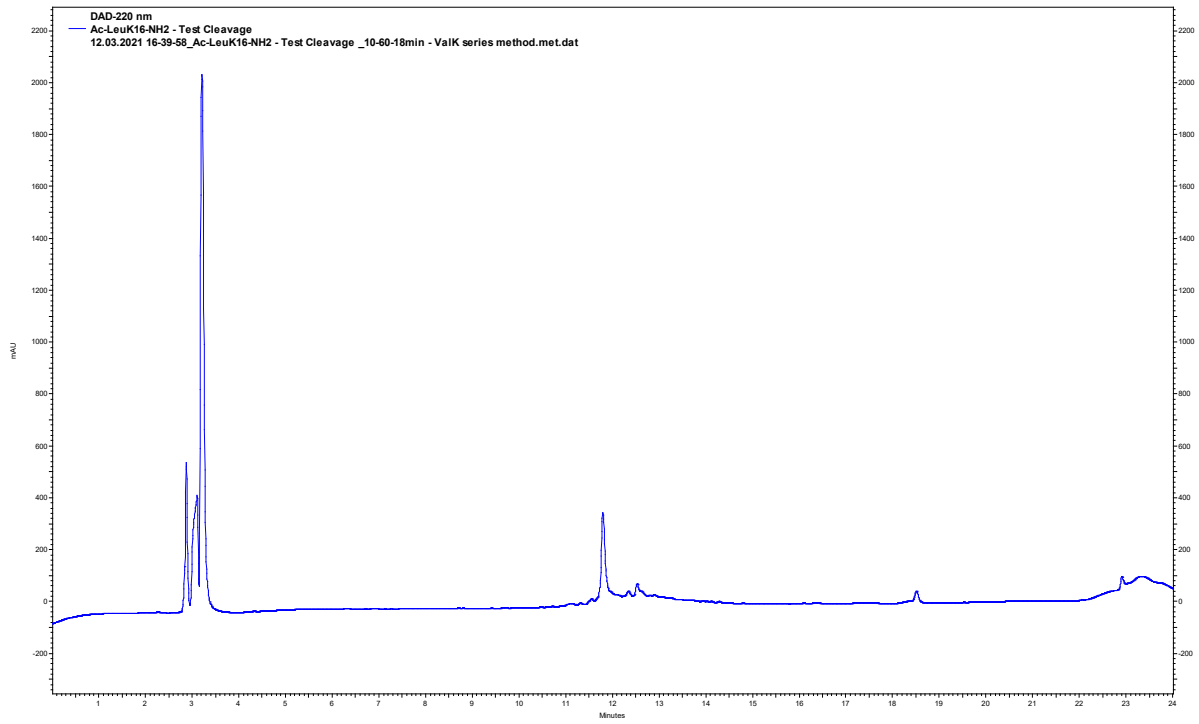

Figure S35: Crude HPLC chromatogram of peptide sequence **LeuK16** (**HPLC:** Chromaster 600 bar – Method: **(A)** H_2O + 0.1% TFA / **(B)** ACN + 0.1% TFA – 10% **(B)** → 60% **(B)** in 18 min. UV detection occurred at 220 nm.

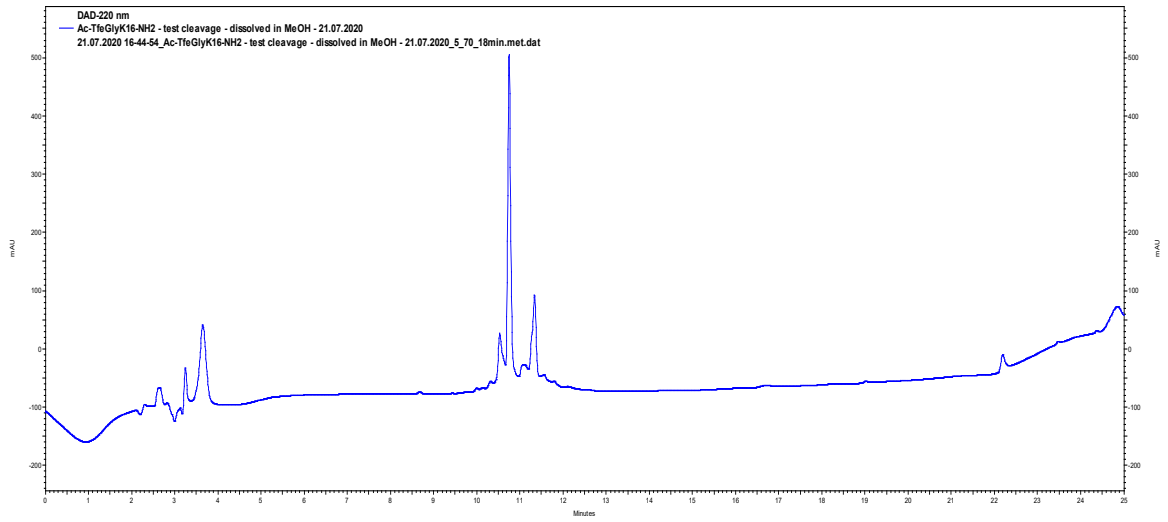

Figure S36: Crude HPLC chromatogram of peptide sequence **TfeGlyK16** (**HPLC:** Hitachi Primaide – Method: **(A)** H_2O + 0.1% TFA / **(B)** ACN + 0.1% TFA – 5% **(B)** → 70% **(B)** in 18 min. UV detection occurred at 220 nm.

4. Peptide Synthesis: Characterization of purified sequences

In this chapter, all peptide sequences of this research project are presented. Their purity was determined through **analytical HPLC** (DAD Detection at 220 nm) (**VWR Chromaster 600 bar** or **Hitachi Primaide**) and **high-resolution mass spectrometry (HRMS)**. All HPLC chromatograms were evaluated with the software OriginLab (OriginLab Corporation, Northampton, MA, USA). For HRMS spectra, the program MassHunter Workstation SoftwareVersion B.02.00 (Agilent Technologies, Santa Clara, CA, USA) was utilized. All HRMS spectra were compared to their **calculated isotope distribution** trough MassHunter Workstation SoftwareVersion B.02.00 (Agilent Technologies, Santa Clara, CA, USA) to provide a fundamentally credible interpretation of experimental data.

peptide	**scale [mmol]**	**amount of purified peptide [mg]**
AbuK10	0.5	10.1
AbuK11	0.5	12.5
AbuK12	0.5	13.6
AbuK13	0.5	13.7
AbuK14	0.1	28.5
AbuK15	0.1	30.5
AbuK16	0.1	45.0
MfeGlyK16	0.1	39.1
DfeGlyK16	0.1	65.2
TfeGlyK16	0.1	78.9
LeuK16	0.1	40.3

4.1 Peptide sequence: AbuK10

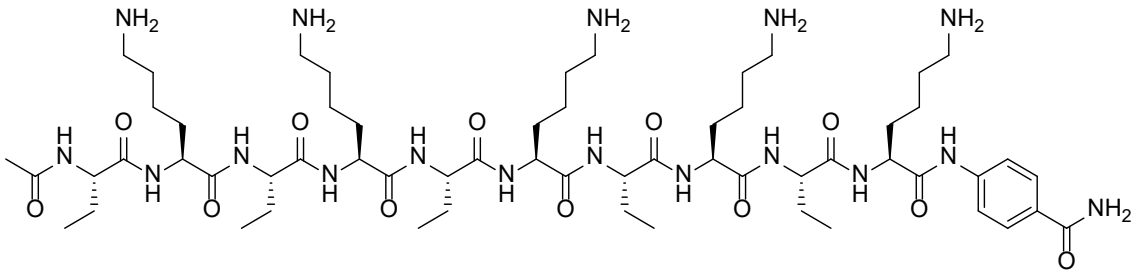

Figure S37: Chemical structure of peptide **AbuK10**.

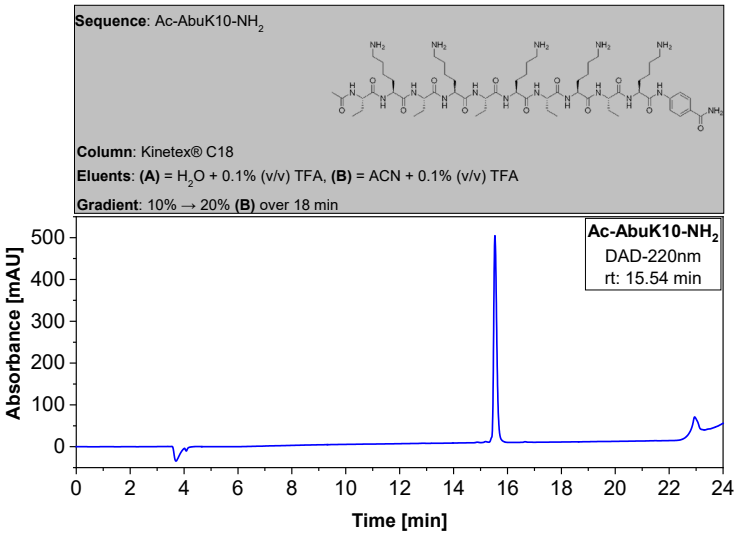

Figure S38: Analytical HPLC chromatogram of pure peptide **AbuK10.**
HPLC: VWR Chromaster 600 bar.

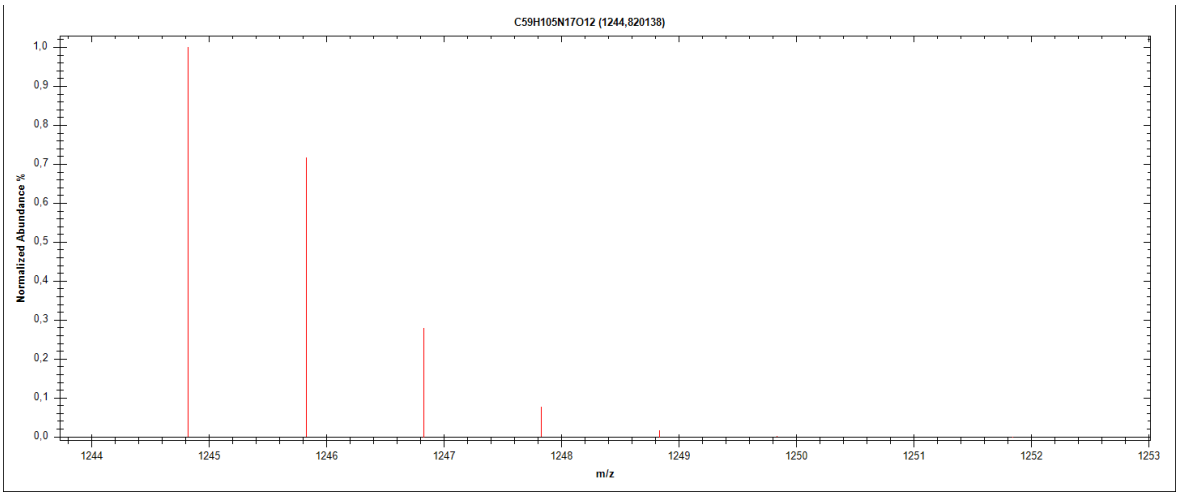

Figure S39: Calculated isotope distribution and mass intensity data for peptide **AbuK10.**

Table S1: Ion species $(M+H)^+$ calculated for peptide sequence **AbuK10**.

m/z Ion species $(M+H)^+$	Abund (% largest)
1244,8201	100
1245,823	71,7
1246,8257	27,81
1247,8284	7,66

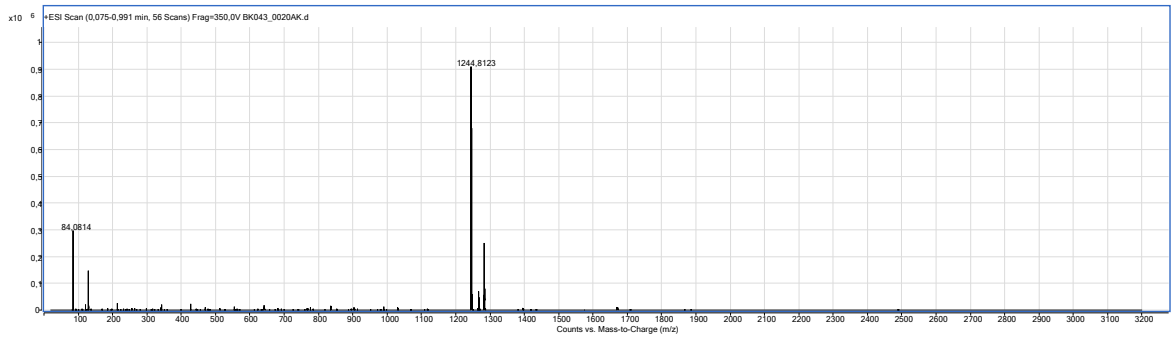

Figure S40: High resolution mass spectrometry (HRMS) spectrum of **AbuK10** in positive ionization mode (**unzoom**).

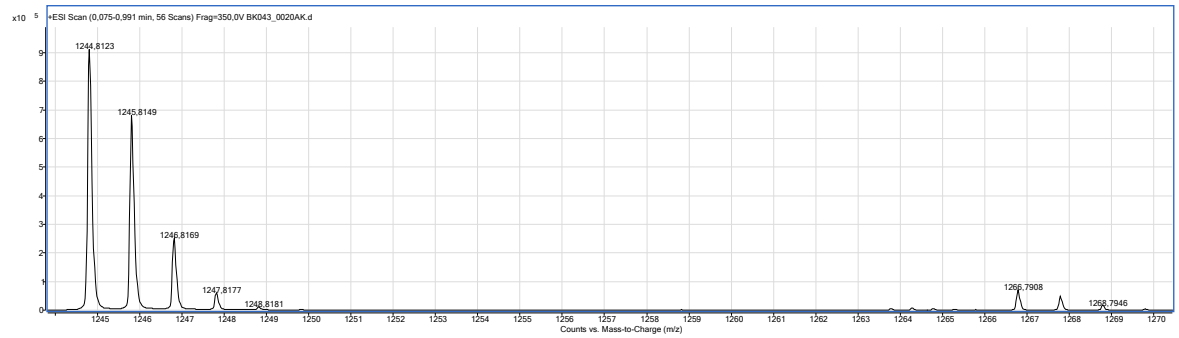

Figure S41: High resolution mass spectrometry (HRMS) spectrum of **AbuK10** in positive ionization mode (**zoom**).

Table S2: Comparison of ion species $(M+H)^+$ both calc. and detected - **AbuK10**.

Ion species $(M+H)^+$ (calc.)	Ion species $(M+H)^+$ (detected)
1244,8201	1244,9123
1245,823	1245,9149
1246,8257	1246,9169
1247,8284	1247,9177

4.2 Peptide sequence: AbuK11

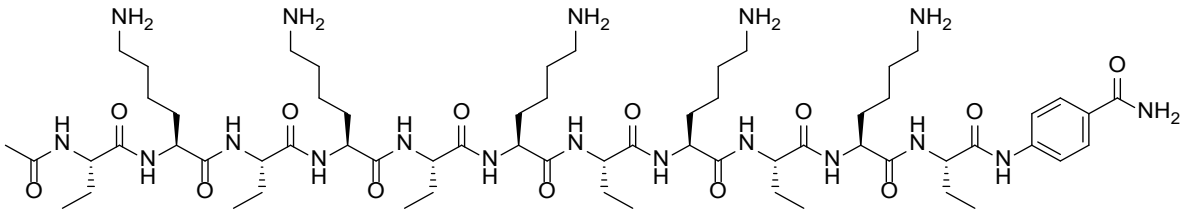

Figure S42: Chemical structure of peptide **AbuK11**.

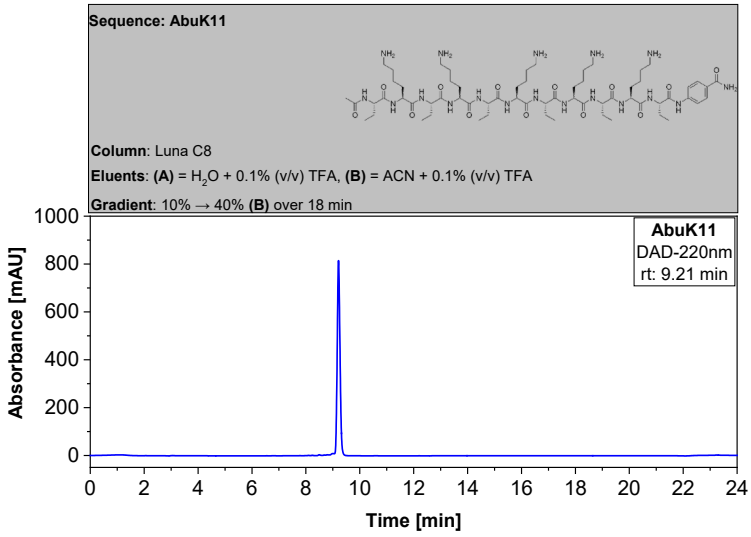

Figure S43: Analytical HPLC chromatogram of pure peptide **AbuK11. HPLC:** Hitachi Primaide.

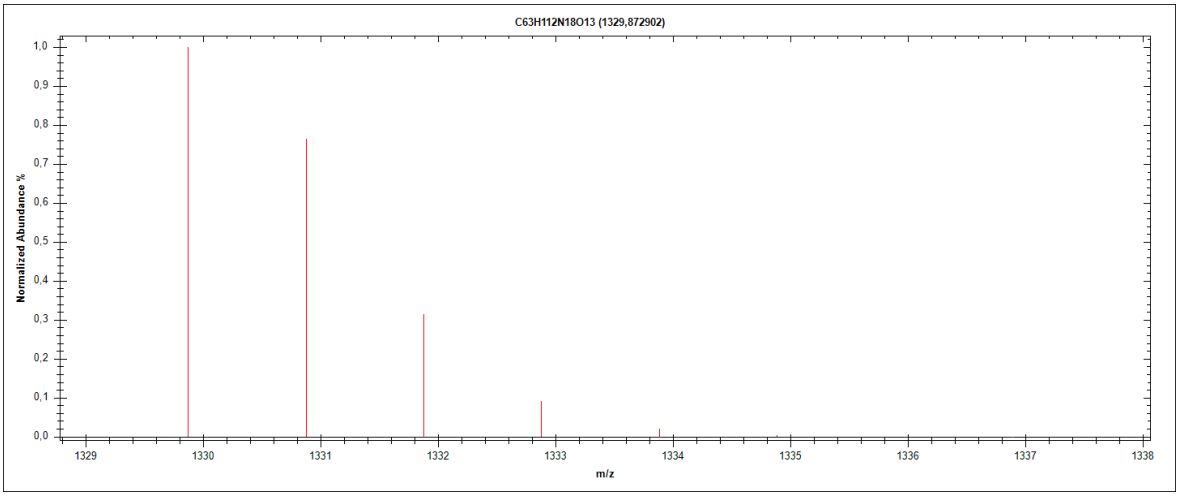

Figure S44: Calculated isotope distribution and mass intensity data for peptide **AbuK11.**

Table S3: Ion species $(M+H)^+$ calculated for peptide sequence **AbuK11**.

m/z **Ion species $(M+H)^+$**	**Abund** **(% largest)**
1329,8729	100
1330,8758	76,51
1331,8785	31,56
1332,8812	9,22

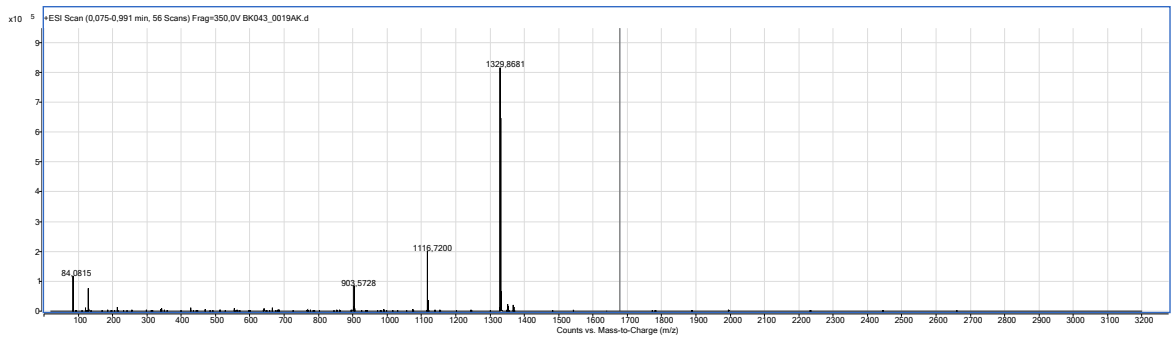

Figure 45: High resolution mass spectrometry (HRMS) spectrum of **AbuK11** in positive ionization mode (**unzoom**).

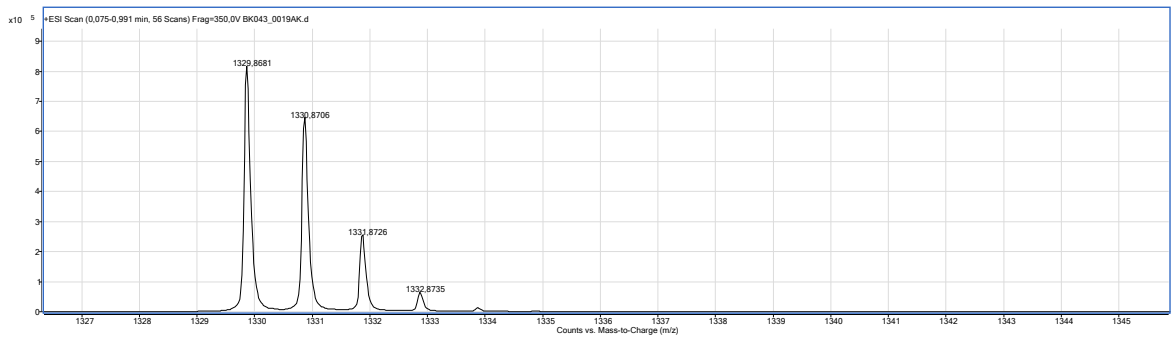

Figure S46: High resolution mass spectrometry (HRMS) spectrum of **AbuK11** in positive ionization mode (**zoom**).

Table S4: Comparison of ion species $(M+H)^+$ both calc. and detected **- AbuK11**.

Ion species $(M+H)^+$ (calc.)	**Ion species $(M+H)^+$ (detected)**
1329,8729	1329,9691
1330,8758	1330,9706
1331,8785	1331,9726
1332,8812	1332,9735

4.3 Peptide sequence: AbuK12

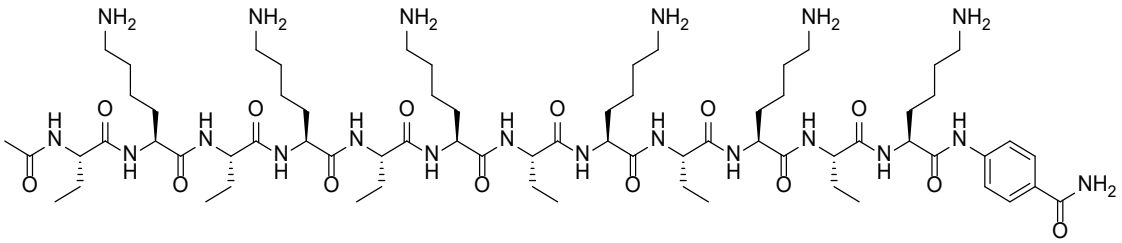

Figure S47: Chemical structure of peptide **AbuK12**.

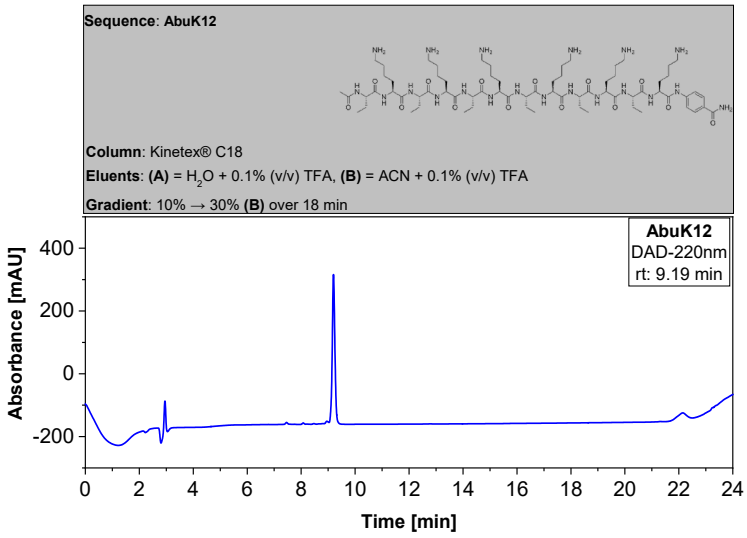

Figure S48: Analytical HPLC chromatogram of pure peptide **AbuK12. HPLC:** VWR Chromaster 600 bar.

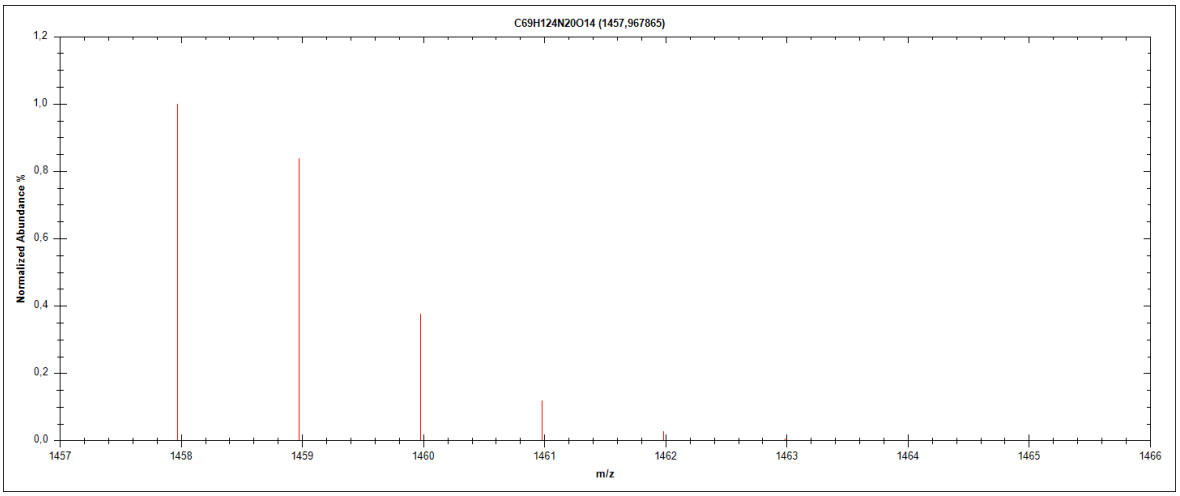

Figure S49: Calculated isotope distribution and mass intensity data for peptide **AbuK12.**

Table S5: Ion species $(M+H)^+$ calculated for peptide sequence **AbuK12**.

m/z **Ion species** $(M+H)^+$	Abund (% largest)
1457,9679	100
1458,9707	83,91
1459,9735	37,66
1460,9761	11,91

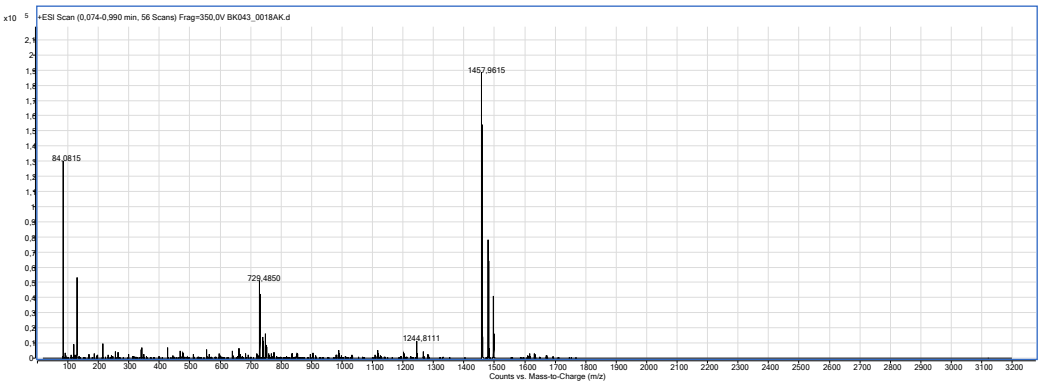

Figure S50: High resolution mass spectrometry (HRMS) spectrum of **AbuK12** in positive ionization mode (**unzoom**).

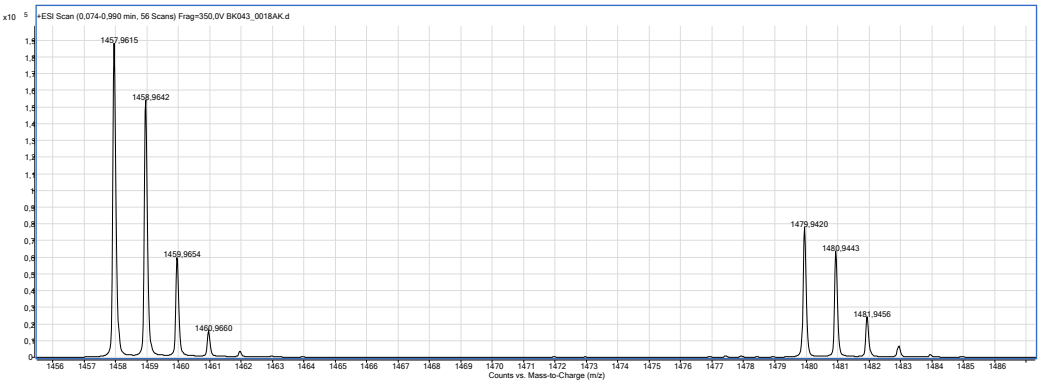

Figure S51: High resolution mass spectrometry (HRMS) spectrum of **AbuK12** in positive ionization mode (**zoom**).

Table S6: Comparison of ion species $(M+H)^+$ both calc. and detected **- AbuK12**.

Ion species $(M+H)^+$ **(calc.)**	**Ion species** $(M+H)^+$ **(detected)**
1457,9679	1457,9615
1458,9707	1458,9642
1459,9735	1459,9654
1460,9761	1460,9660

4.4 Peptide sequence: AbuK13

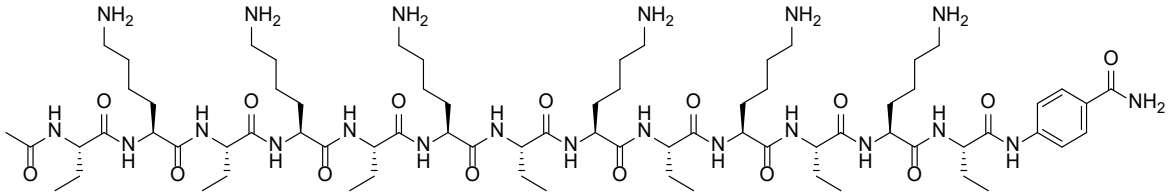

Figure S52: Chemical structure of peptide **AbuK13**.

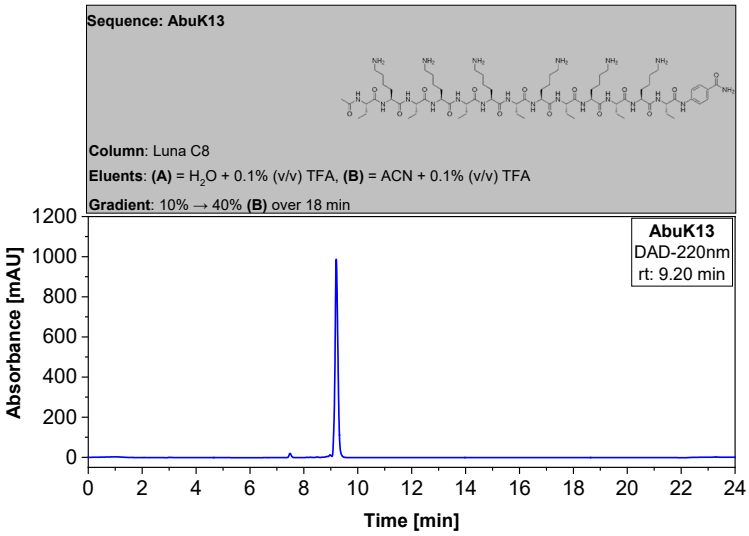

Figure S53: Analytical HPLC chromatogram of pure peptide **AbuK13. HPLC:** Hitachi Primaide.

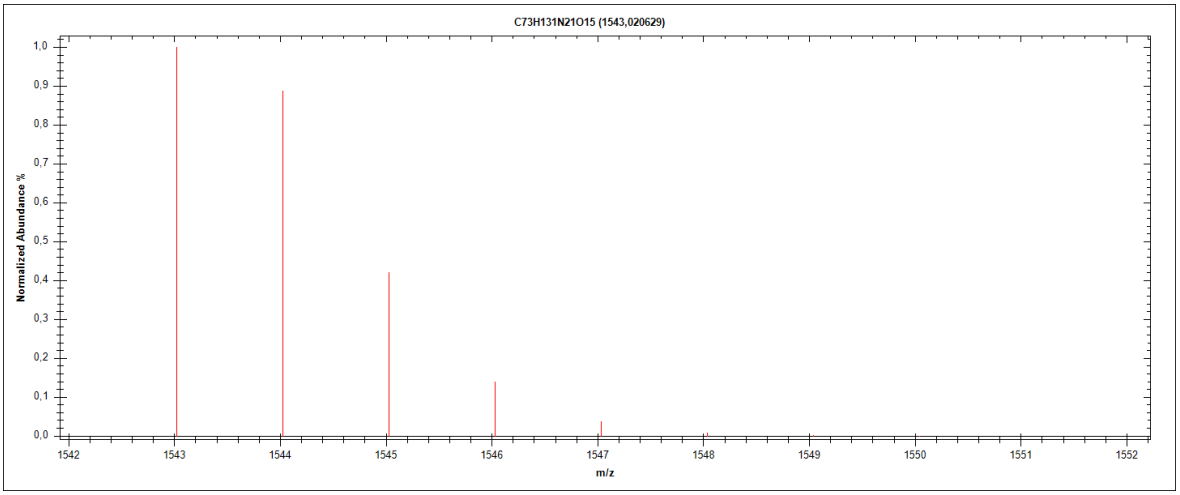

Figure S54: Calculated isotope distribution and mass intensity data for peptide **AbuK13.**

Table S7: Ion species $(M+H)^+$ calculated for peptide sequence **AbuK13**.

m/z **Ion species $(M+H)^+$**	**Abund** **(% largest)**
1543,0206	100
1544,0235	88,72
1545,0262	41,99
1546,0289	13,98

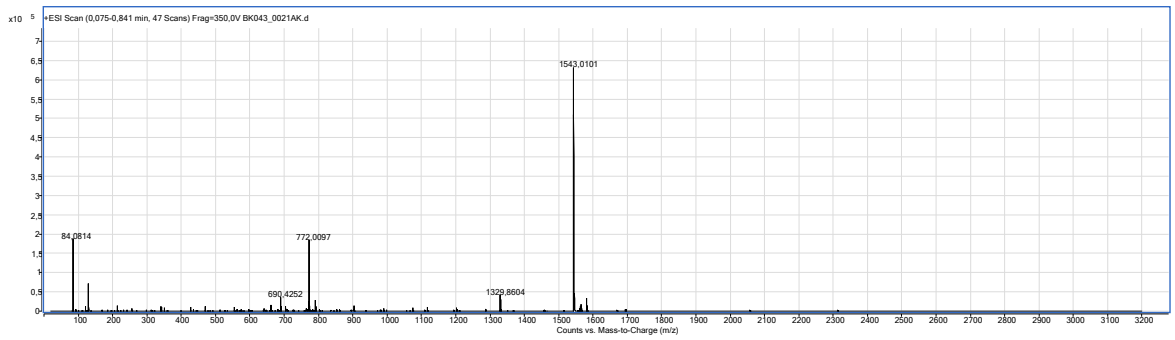

Figure S55: High resolution mass spectrometry (HRMS) spectrum of **AbuK13** in positive ionization mode (**unzoom**).

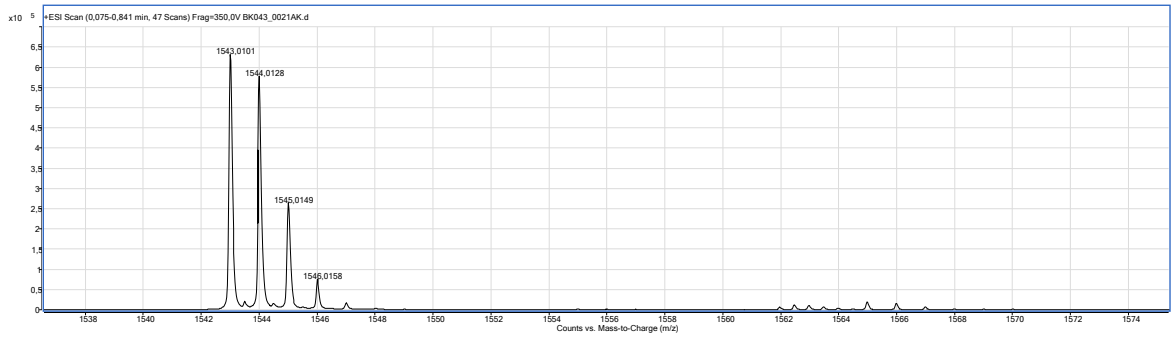

Figure S56: High resolution mass spectrometry (HRMS) spectrum of **AbuK13** in positive ionization mode (**zoom**).

Table S8: Comparison of ion species $(M+H)^+$ both calc. and detected **- AbuK13**.

Ion species $(M+H)^+$ (calc.)	**Ion species $(M+H)^+$ (detected)**
1543,0206	1543,0101
1544,0235	1544,0128
1545,0262	1545,0149
1546,0289	1546,0158

4.5 Peptide sequence: AbuK14

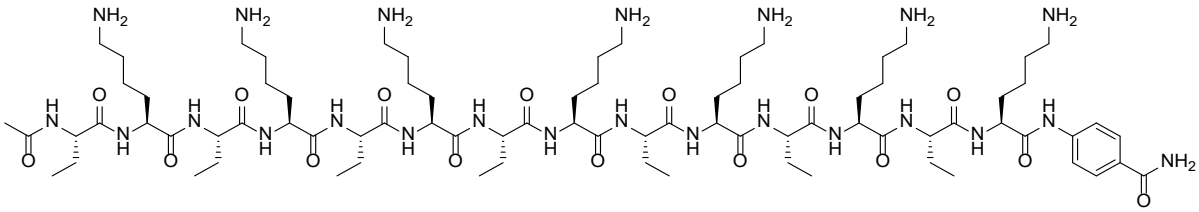

Figure S57: Chemical structure of peptide **AbuK14**.

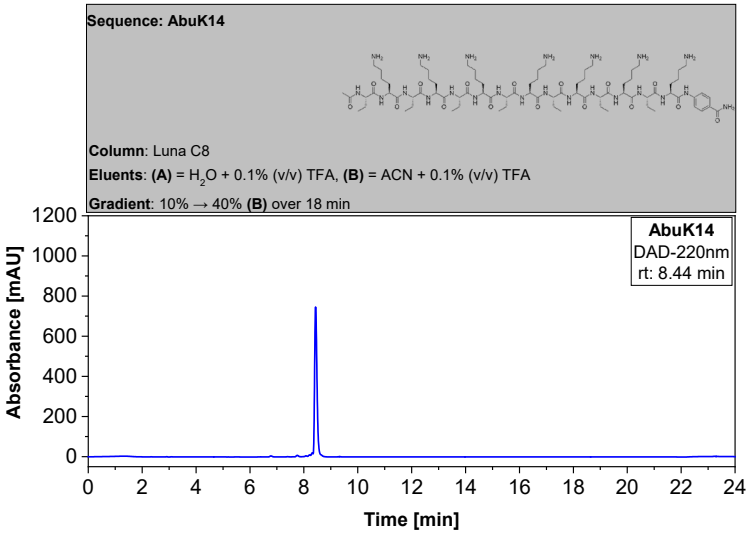

Figure S58: Analytical HPLC chromatogram of pure peptide **AbuK14. HPLC:** Hitachi Primaide

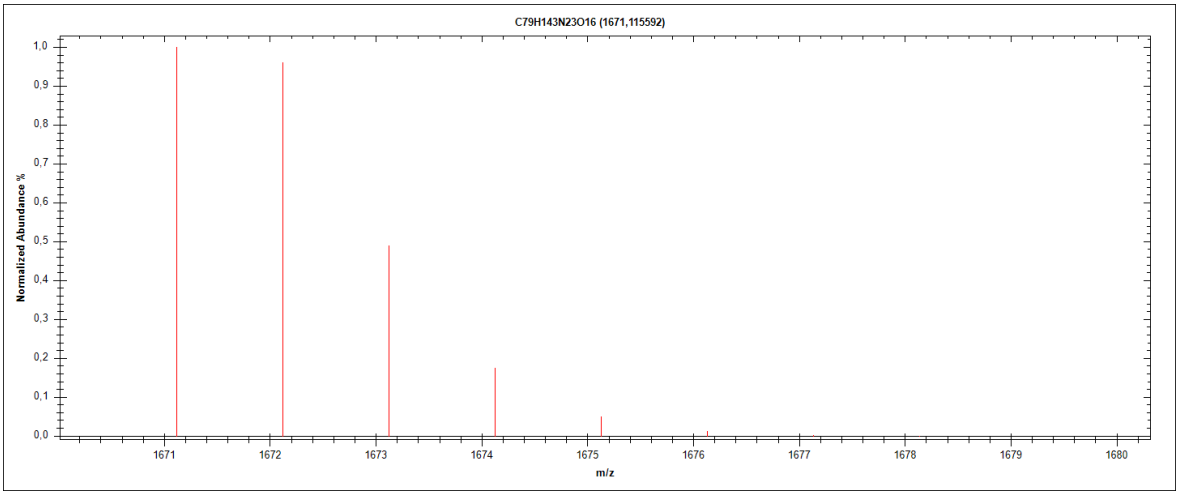

Figure S59: Calculated isotope distribution and mass intensity data for peptide **AbuK14.**

Table S9: Ion species $(M+H)^+$ calculated for peptide sequence **AbuK14**.

m/z **Ion species** $(M+H)^+$	Abund (% largest)
1671,1156	100
1672,1185	96,11
1673,1212	49
1674,1239	17,5

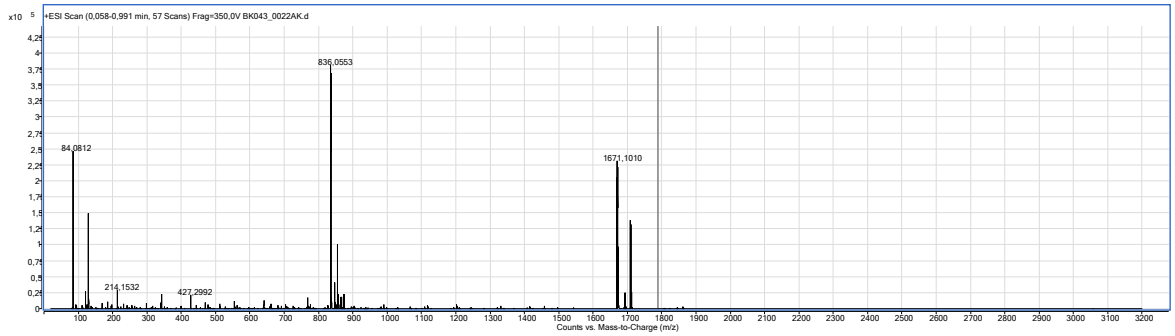

Figure S60: High resolution mass spectrometry (HRMS) spectrum of **AbuK14** in positive ionization mode (**unzoom**).

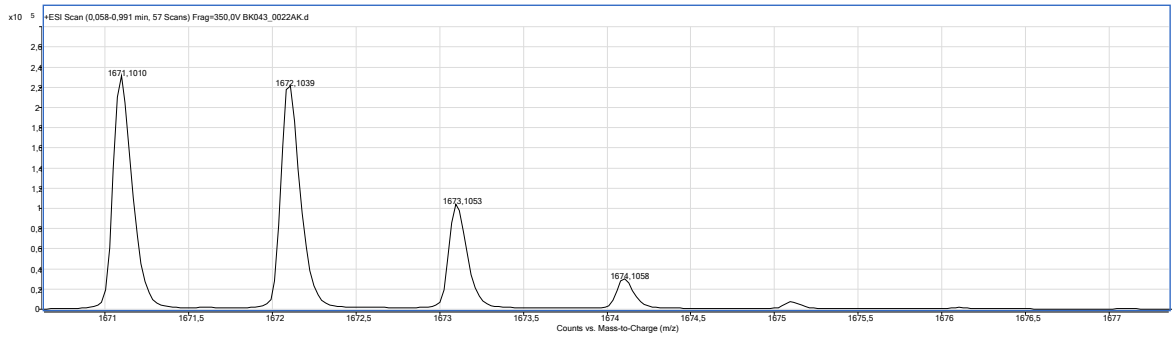

Figure S61: High resolution mass spectrometry (HRMS) spectrum of **AbuK14** in positive ionization mode (**zoom**).

Table S10: Comparison of ion species $(M+H)^+$ both calc. and detected **- AbuK14**.

Ion species $(M+H)^+$ **(calc.)**	**Ion species** $(M+H)^+$ **(detected)**
1671,1156	1671,1010
1672,1185	1672,1039
1673,1212	1673,1053
1674,1239	1674,1058

4.6 Peptide sequence: AbuK15

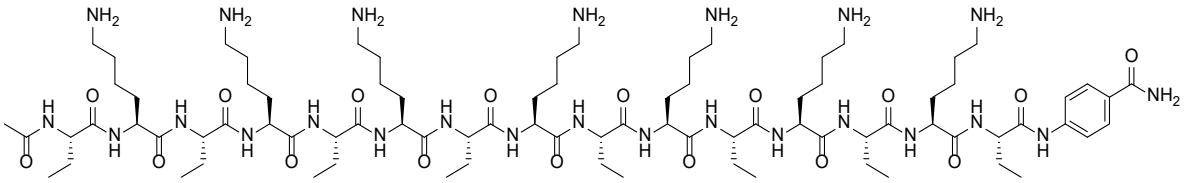

Figure S62: Chemical structure of peptide **AbuK15**.

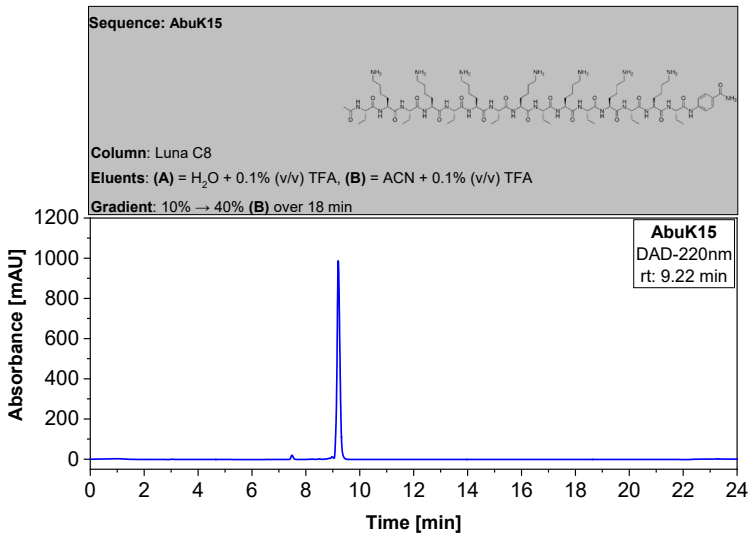

Figure S63: Analytical HPLC chromatogram of pure peptide **AbuK15. HPLC:** Hitachi Primaide

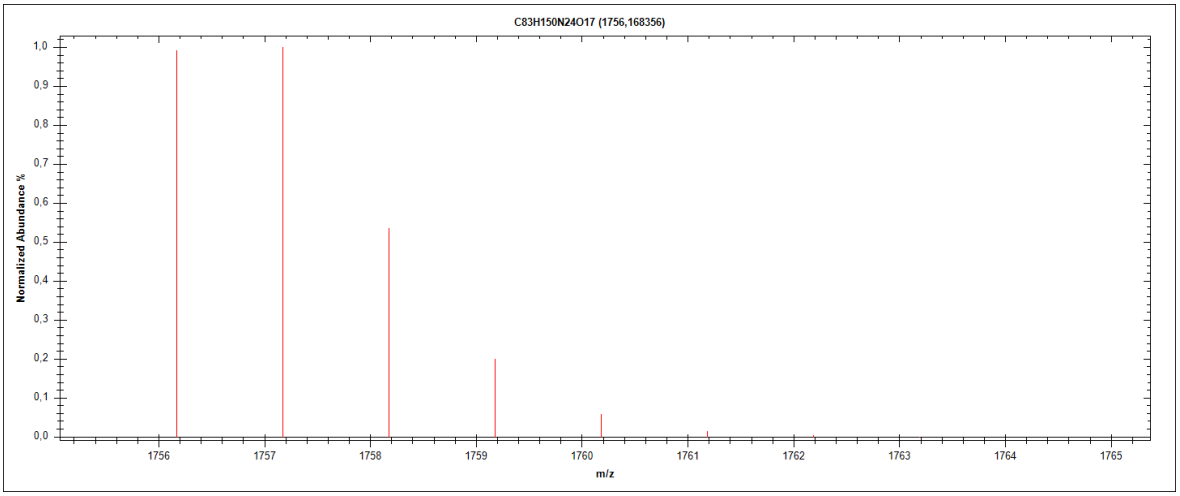

Figure S64: Calculated isotope distribution and mass intensity data for peptide **AbuK15.**

Table S11: Ion species $(M+H)^+$ calculated for peptide sequence **AbuK15**.

m/z Ion species $(M+H)^+$	Abund (% largest)
1756,1684	99,09
1757,1712	100
1758,1740	53,43
1759,1767	19,97

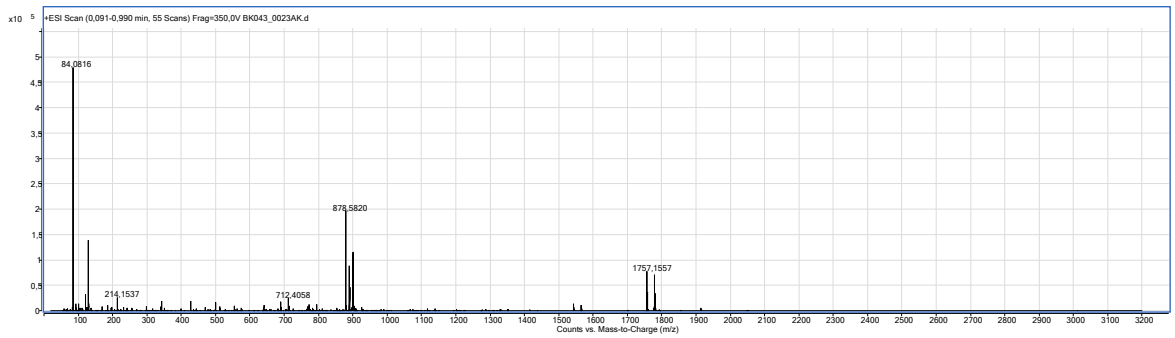

Figure S65: High resolution mass spectrometry (HRMS) spectrum of **AbuK15** in positive ionization mode (**unzoom**).

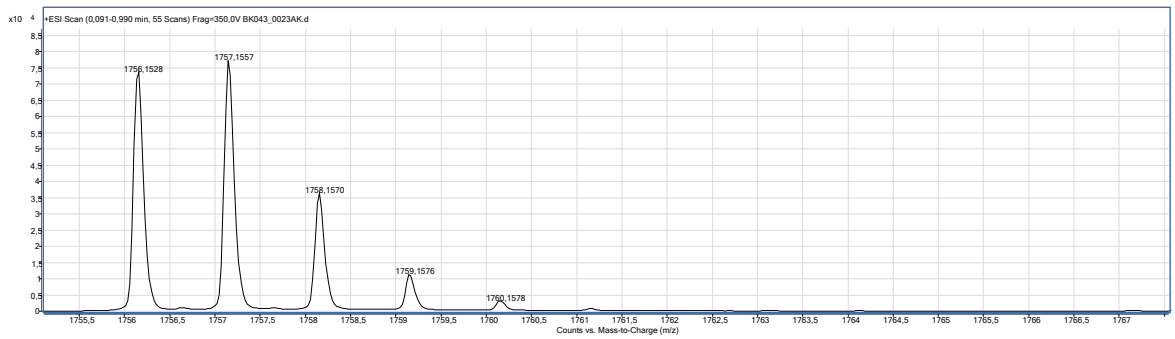

Figure S66: High resolution mass spectrometry (HRMS) spectrum of **AbuK15** in positive ionization mode (**zoom**).

Table 12: Comparison of ion species $(M+H)^+$ both calc. and detected **- AbuK15**.

Ion species $(M+H)^+$ (calc.)	Ion species $(M+H)^+$ (detected)
1756,1684	1756,1528
1757,1712	1757,1557
1758,1740	1758,1570
1759,1767	1759,1576

4.7 Peptide sequence: AbuK16

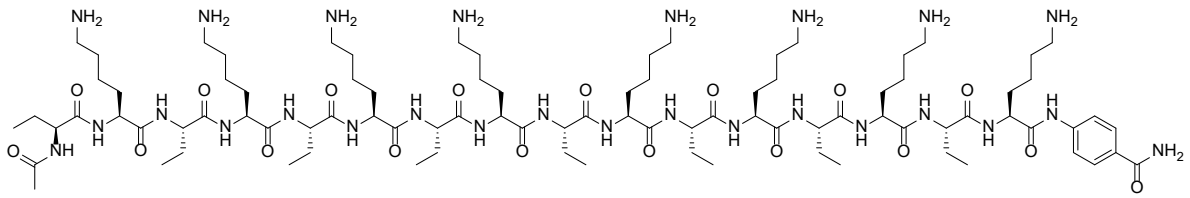

Figure S67: Chemical structure of peptide **AbuK16**.

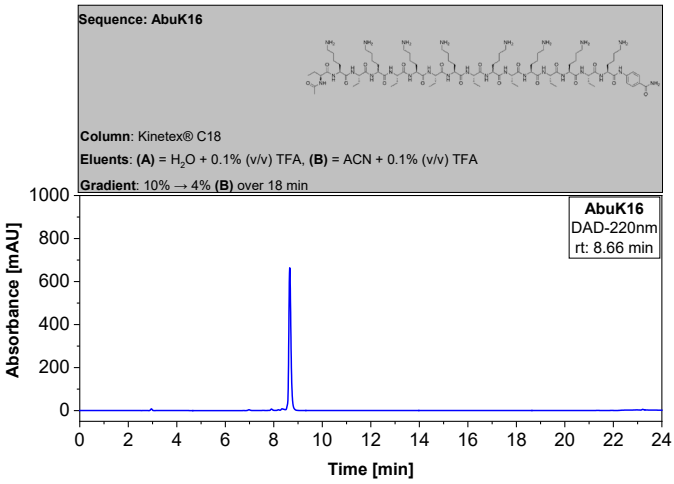

Figure S68: Analytical HPLC chromatogram of pure peptide **AbuK16. HPLC:** VWR Chromaster 600 bar.

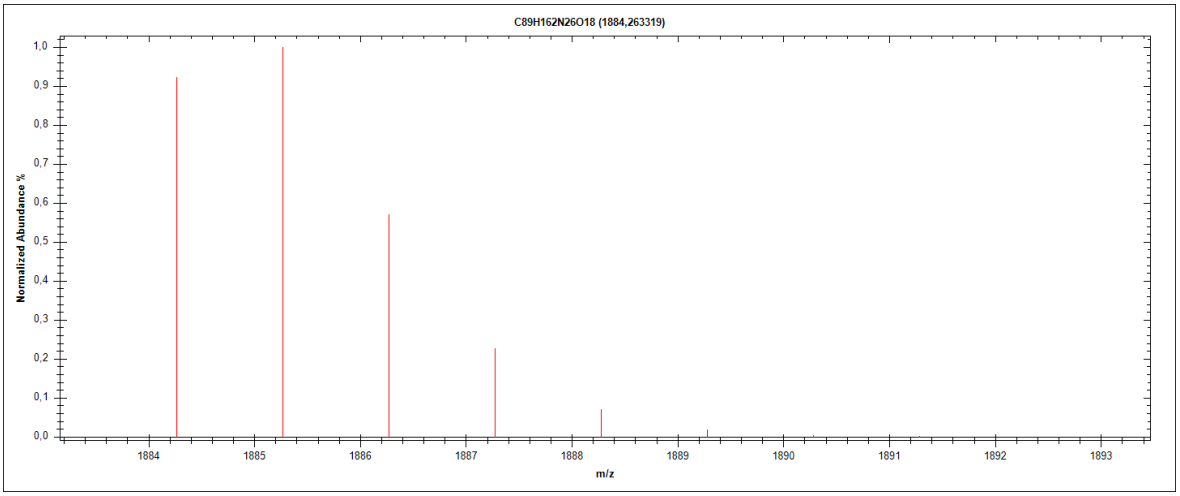

Figure S69: Calculated isotope distribution and mass intensity data for peptide **AbuK16.**

Table S13: Ion species $(M+H)^+$ calculated for peptide sequence **AbuK16**.

m/z **Ion species** $(M+H)^+$	Abund (% largest)
1884,2633	92,32
1885,2662	100
1886,2689	57,08
1887,2716	22,72

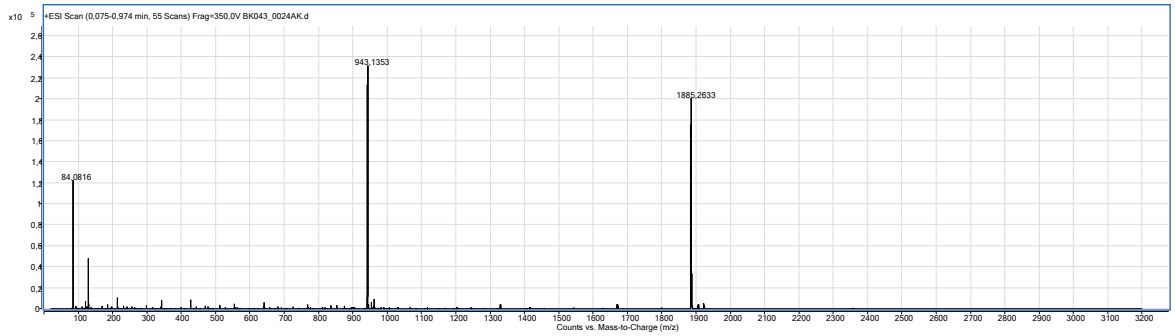

Figure S70: High resolution mass spectrometry (HRMS) spectrum of **AbuK16** in positive ionization mode (**unzoom**).

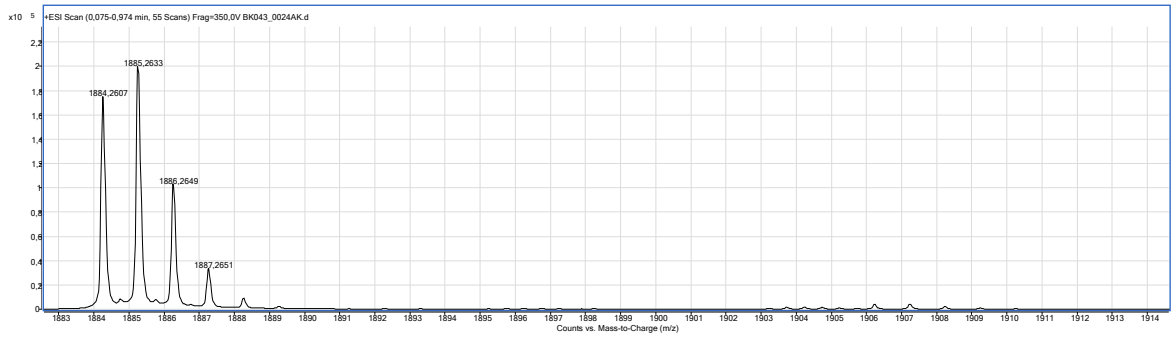

Figure S71: High resolution mass spectrometry (HRMS) spectrum of **AbuK16** in positive ionization mode (**zoom**).

Table S14: Comparison of ion species $(M+H)^+$ both calc. and detected **- AbuK16**.

Ion species $(M+H)^+$ **(calc.)**	**Ion species** $(M+H)^+$ **(detected)**
1884,2633	1884,2607
1885,2662	1885,2633
1886,2689	1886,2649
1887,2716	1887,2681

4.8 Peptide sequence: MfeGlyK16

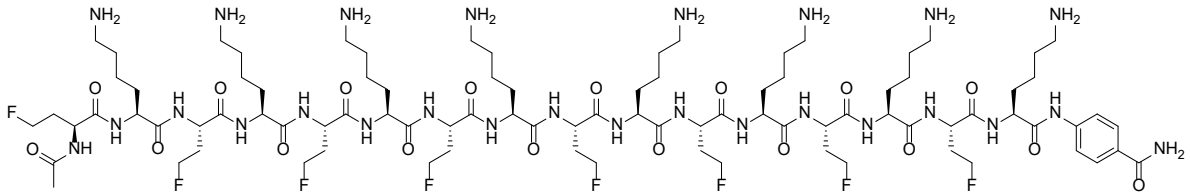

Figure S72: Chemical structure of peptide **MfeGlyK16**.

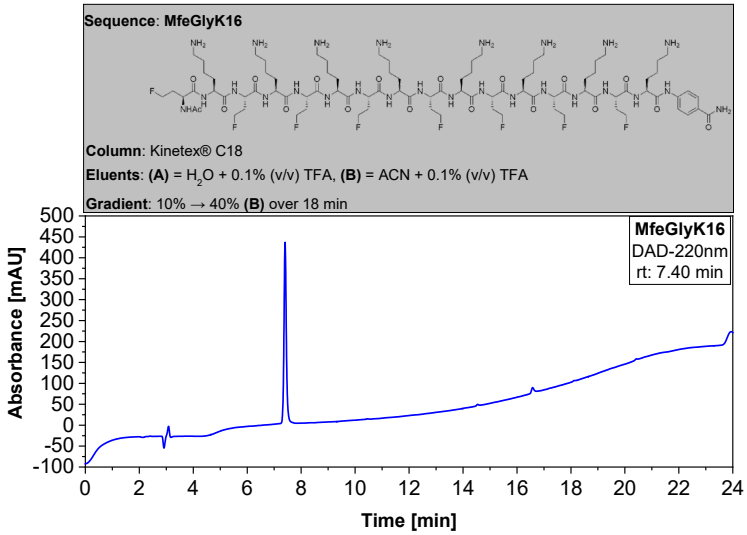

Figure S73: Analytical HPLC chromatogram of pure peptide **MfeGlyK16. HPLC:** VWR Chromaster 600 bar.

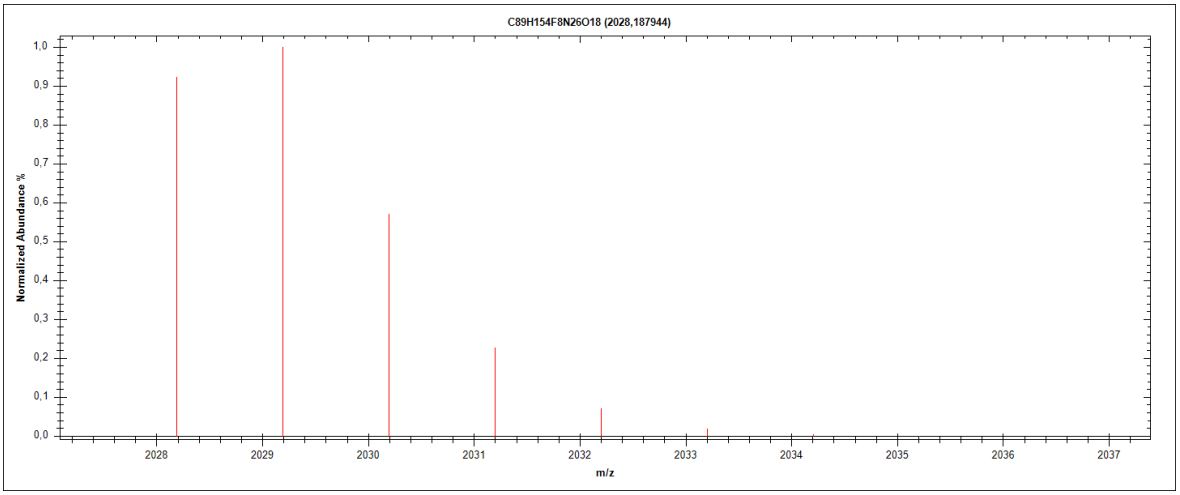

Figure S74: Calculated isotope distribution and mass intensity data for peptide **MfeGlyK16.**

Table S15: Ion species $(M+H)^+$ calculated for peptide sequence **MfeGlyK16**.

m/z Ion species $(M+H)^+$	Abund (% largest)
2028,1879	92,40
2029,1908	100
2030,1936	57,03
2031,1963	22,68

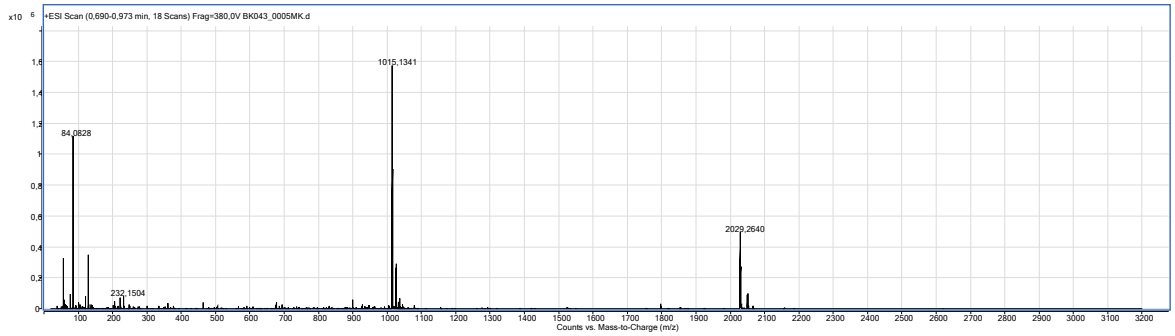

Figure S75: High resolution mass spectrometry (HRMS) spectrum of **MfeGlyK16** in positive ionization mode (**unzoom**).

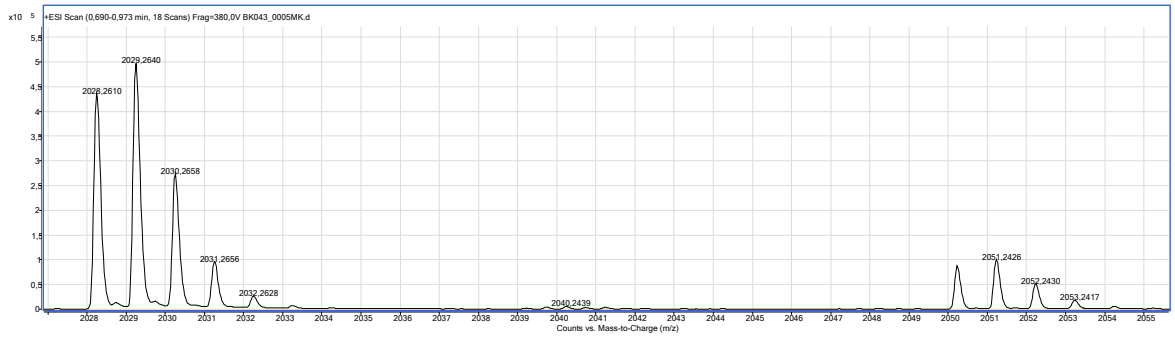

Figure S76: High resolution mass spectrometry (HRMS) spectrum of **MfeGlyK16** in positive ionization mode (**zoom**).

Table S16: Comparison of ion species $(M+H)^+$ both calc. and detected **- MfeGlyK16**.

Ion species $(M+H)^+$ (calc.)	Ion species $(M+H)^+$ (detected)
2028,1879	2028,2610
2029,1908	2029,2640
2030,1936	2030,2658
2031,1963	2031,2656

4.9 Peptide sequence: DfeGlyK16

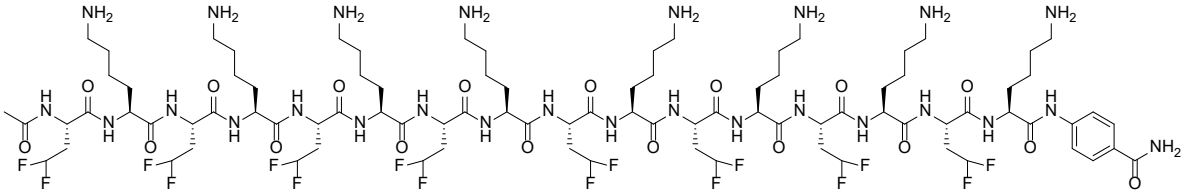

Figure S77: Chemical structure of peptide **DfeGlyK16**.

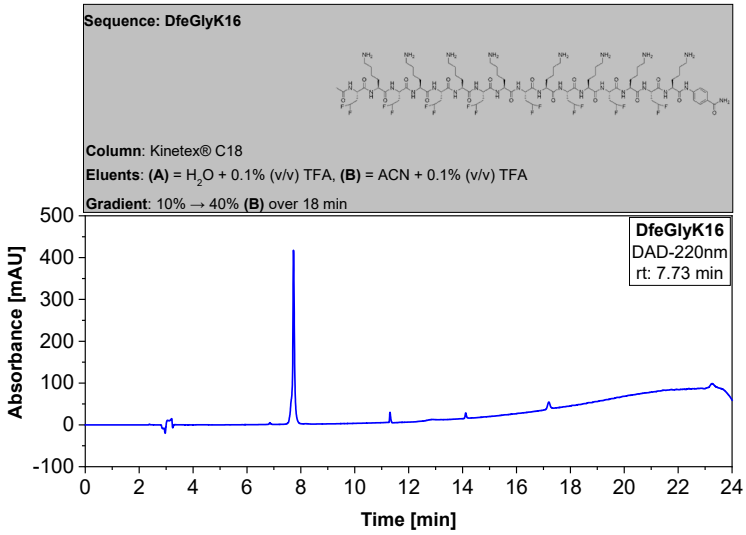

Figure S78: Analytical HPLC chromatogram of pure peptide **DfeGlyK16. HPLC:** VWR Chromaster 600 bar.

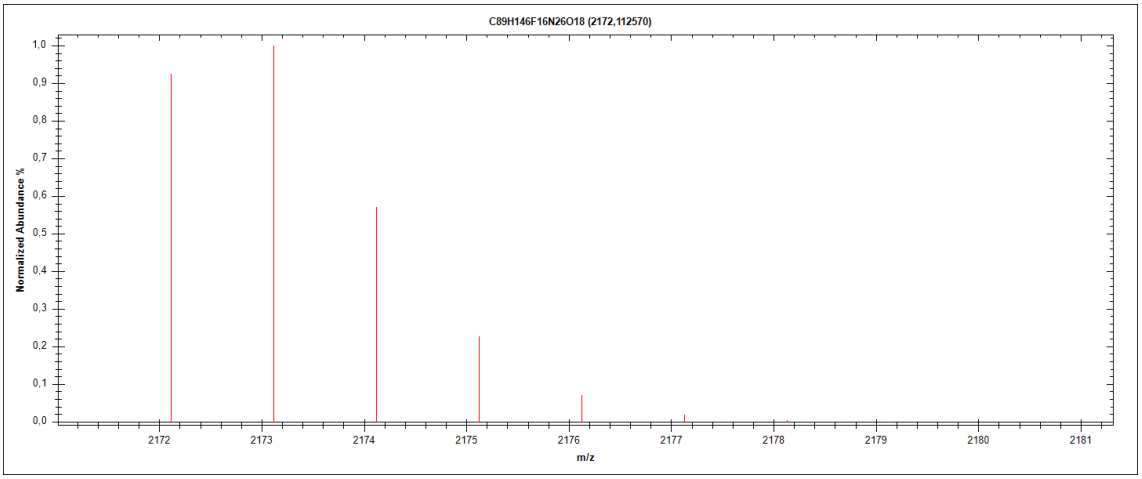

Figure S79: Calculated isotope distribution and mass intensity data for peptide **DfeGlyK16.**

Table S17: Ion species $(M+H)^+$ calculated for peptide sequence **DfeGlyK16**.

m/z **Ion species $(M+H)^+$**	**Abund** **(% largest)**
2172,1126	92,48
2173,1154	100
2174,1182	56,99
2175,1209	22,65

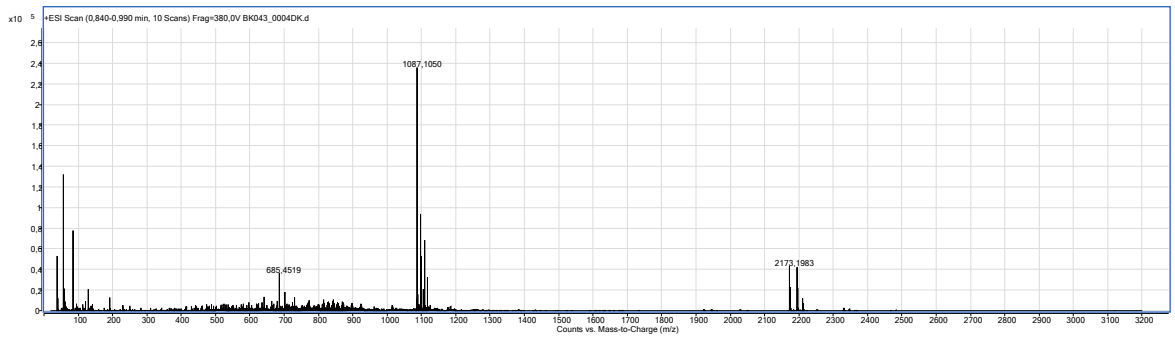

Figure S80: High resolution mass spectrometry (HRMS) spectrum of **DfeGlyK16** in positive ionization mode (**unzoom**).

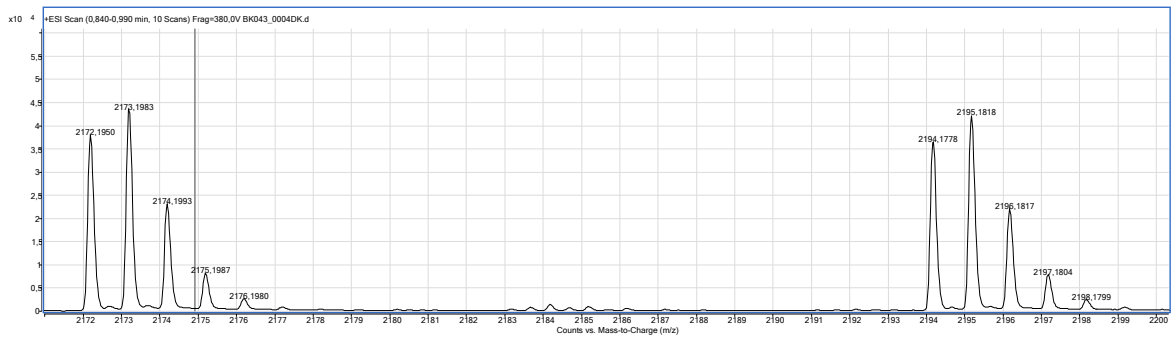

Figure S81: High resolution mass spectrometry (HRMS) spectrum of **DfeGlyK16** in positive ionization mode (**zoom**).

Table 18: Comparison of ion species $(M+H)^+$ both calc. and detected **– DfeGlyK16**.

Ion species $(M+H)^+$ (calc.)	**Ion species $(M+H)^+$ (detected)**
2172,1126	2172,1950
2173,1154	2173,1983
2174,1182	2174,1993
2175,1209	2175,1987

4.10 Peptide sequence: TfeGlyK16

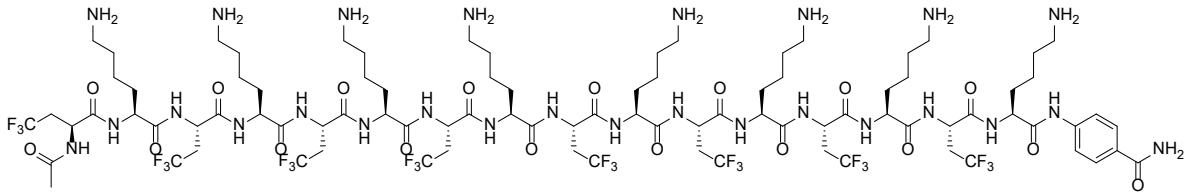

Figure S82: Chemical structure of peptide **TfeGlyK16**.

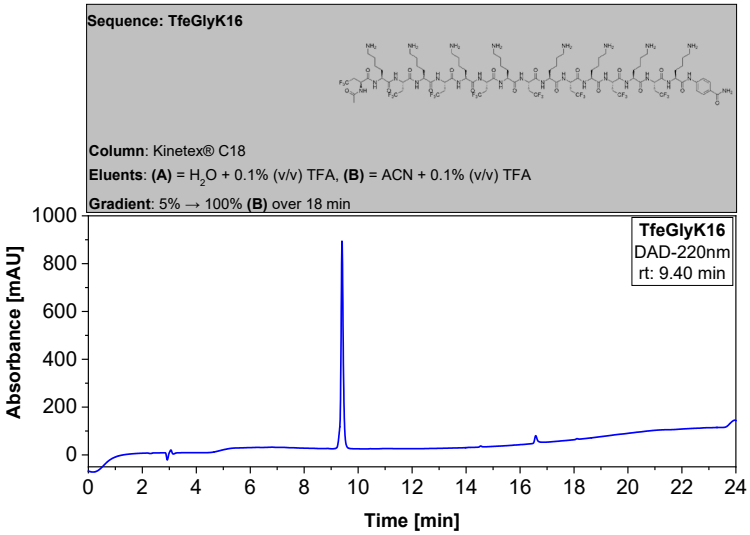

Figure S83: Analytical HPLC chromatogram of pure peptide **TfeGlyK16. HPLC:** VWR Chromaster 600 bar.

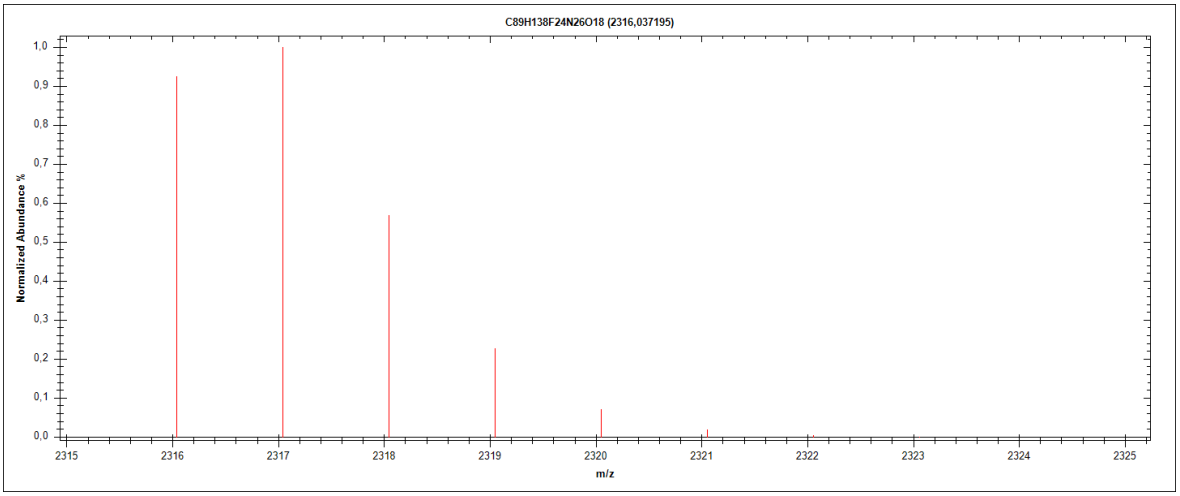

Figure S84: Calculated isotope distribution and mass intensity data for peptide **TfeGlyK16.**

Table S19: Ion species $(M+H)^+$ calculated for peptide sequence **TfeGlyK16**.

m/z **Ion species $(M+H)^+$**	**Abund** **(% largest)**
2316,0372	92,56
2317,0400	100
2318,0428	56,95
2319,0455	22,62

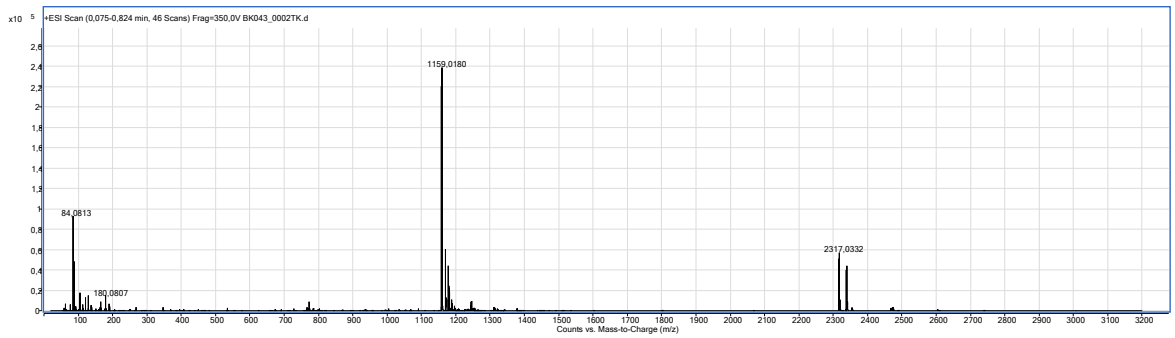

Figure S85: High resolution mass spectrometry (HRMS) spectrum of **TfeGlyK16** in positive ionization mode (**unzoom**).

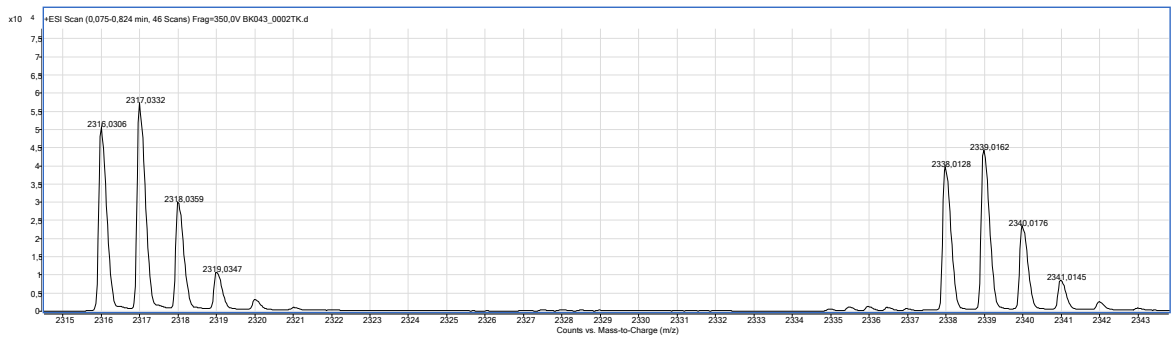

Figure S86: High resolution mass spectrometry (HRMS) spectrum of **TfeGlyK16** in positive ionization mode (**zoom**).

Table S20: Comparison of ion species $(M+H)^+$ both calc. and detected **– TfeGlyK16**.

Ion species $(M+H)^+$ (calc.)	**Ion species $(M+H)^+$ (detected)**
2316,0372	2316,0306
2317,0400	2317,0332
2318,0428	2318,0359
2319,0455	2319,0347

4.11 Peptide sequence: LeuK16

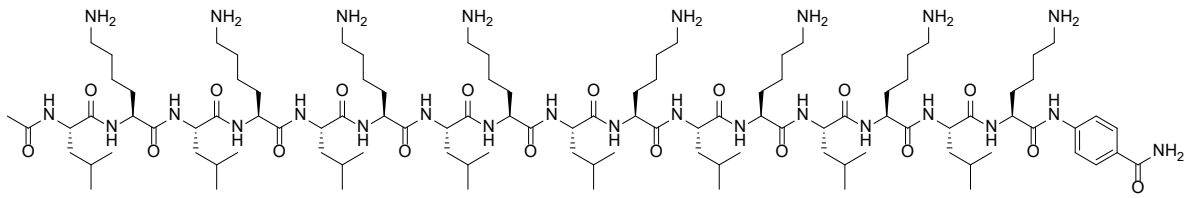

Figure S87: Chemical structure of peptide **LeuK16**.

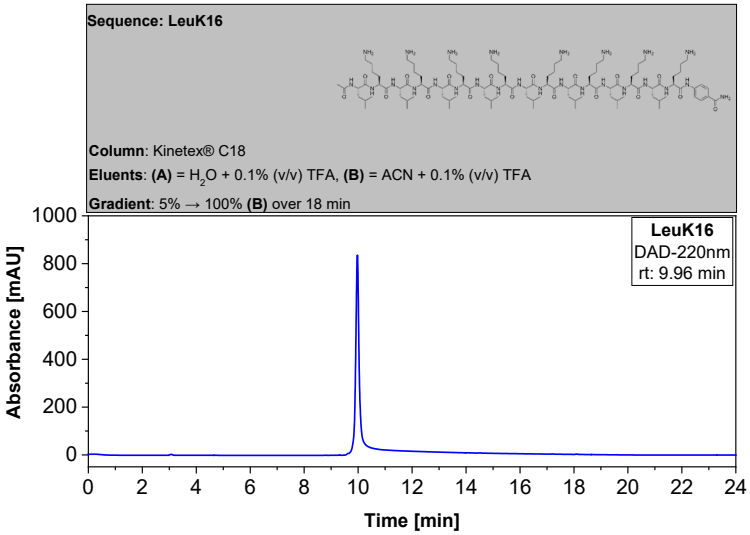

Figure S88: Analytical HPLC chromatogram of pure peptide **LeuK16. HPLC:** VWR Chromaster 600 bar.

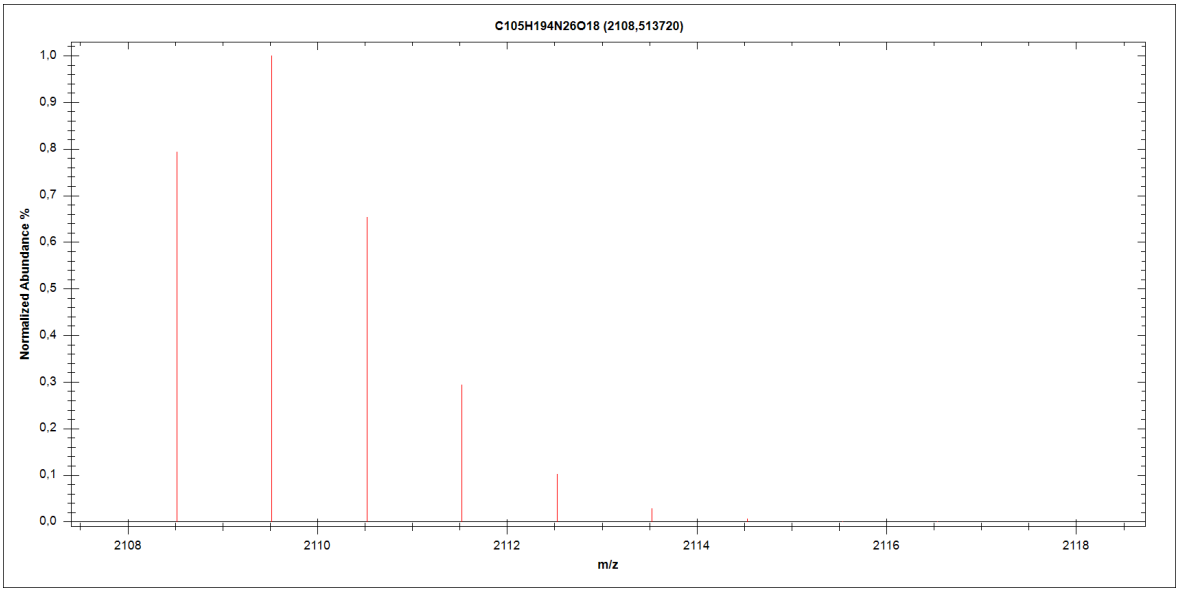

Figure S89: Calculated isotope distribution and mass intensity data for peptide **LeuK16.**

Table S21: Ion species $(M+H)^+$ calculated for peptide sequence **LeuK16**.

m/z **Ion species** $(M+H)^+$	Abund (% largest)
2108,5137	79,37
2109,5167	100
2110,5195	65.43
2111,5223	29,53

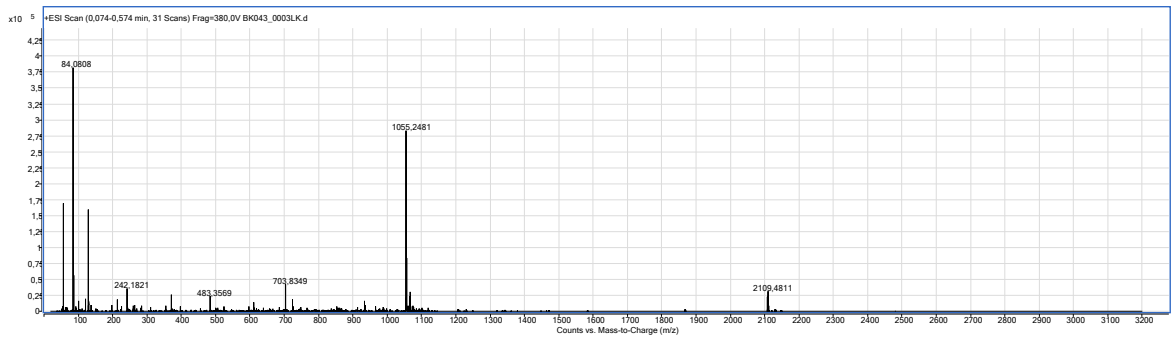

Figure S90: High resolution mass spectrometry (HRMS) spectrum of **LeuK16** in positive ionization mode (**unzoom**).

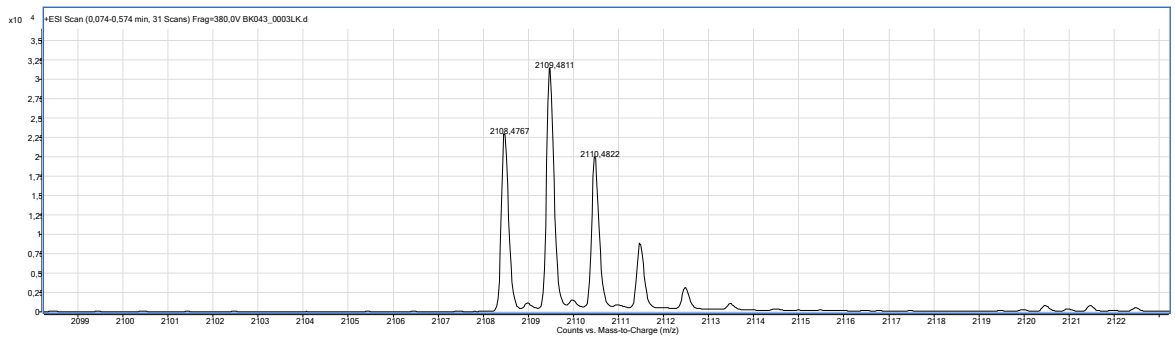

Figure S91: High resolution mass spectrometry (HRMS) spectrum of **LeuK16** in positive ionization mode (**zoom**).

Table S22: Comparison of ion species $(M+H)^+$ both calc. and detected **- LeuK16**.

Ion species $(M+H)^+$ **(calc.)**	**Ion species** $(M+H)^+$ **(detected)**
2108,5137	2108,4767
2109,5167	2109,4811
2110,5195	2110,4822

5. Determination of peptide stock concentrations

To determine the concentration of each peptide stock in a reproducible and precise manner, we established a protocol for this purpose based on UV spectroscopy. Therefore, the commercially available dipeptide **H_2N-[4]Abz-Gly-OH** / *para*-aminohippuric acid (**PAH**) (Fluorochem, salt-free) was utilized as reference sample. This protocol is based on previous attempts by our group.[12]

PAH was dissolved in a 6M guanidinium hydrochloride solution, pH 7.4 and prepared in different concentrations (5 µM, 15 µM, 30 µM, 50 µM, 100 µM, 150 µM). A calibration curve was determined by measuring the UV absorbance (BioPhotometer plus photometer from Eppendorf, Hamburg, Germany) of each sample at 280 nm. Disposable PMMA cuvettes (Eppendorf, Hamburg, Germany) with path lengths of 10 mm were used.

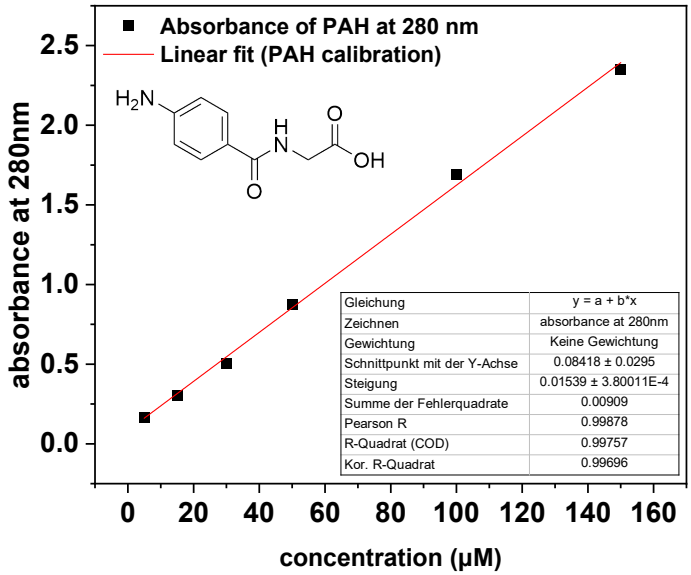

Figure S92: Calibration curve of **PAH** for the determination of peptide concentration stocks. UV absorbance was recorded at room temperature.

Then, aliquots (10 µL) of respective peptide stocks (dissolved in HFIP) were taken and the solvent was evaporated using a gentle stream of N_2. The dried peptide film was redissolved in in a 6M guanidinium hydrochloride solution, pH 7.4 to achieve an overall peptide solution (1000 µL) with a dilution factor (DL) of 100. UV absorbance was recorded at 280 nm and taken as mean value from three independent measurements. The concentration was calculated based on the equation y = a + b*x derived from a linear fit. (x = concentration in µM)

6. CD spectroscopy: Further results

In this chapter, further CD spectra of this publication are presented and discussed.

6.1 CD Spectroscopy: AbuK10-16 – water / BTP buffer pH 9 – concentration: 2 wt%

We were surprised by the exclusive ability of **AbuK14** and **AbuK16** to undergo β-sheet formation which lacked for the truncated variants and **AbuK15**. So, we examined these peptides in only aqueous solutions (**Figure S93, a-b**), but also in buffered conditions with a more basic environment (pH 9) (**Figure S93,c-d**) to promote saturation of the positively charged lysine residues. CD spectra in water revealed the formation of PPII helices for all peptides, caused as expected by electrostatic and steric interactions of charged Lys side chains. Thus, adjustment of the buffer into more basic conditions enabled the conversion of helical structures into β-sheets for **AbuK12**, **AbuK14** and **AbuK16**, whereas **AbuK11**, **AbuK13** and **AbuK15** revealed indeterminable CD spectra. In consequence, the structural pattern given by an odd amount of amino acid residues of **AbuK11**, **AbuK13** and **AbuK15** has revealed to disrupt structure assembly in basic buffered environments, whereas we propose for **AbuK10** the truncated chain length as cause to withhold β-sheet formation.

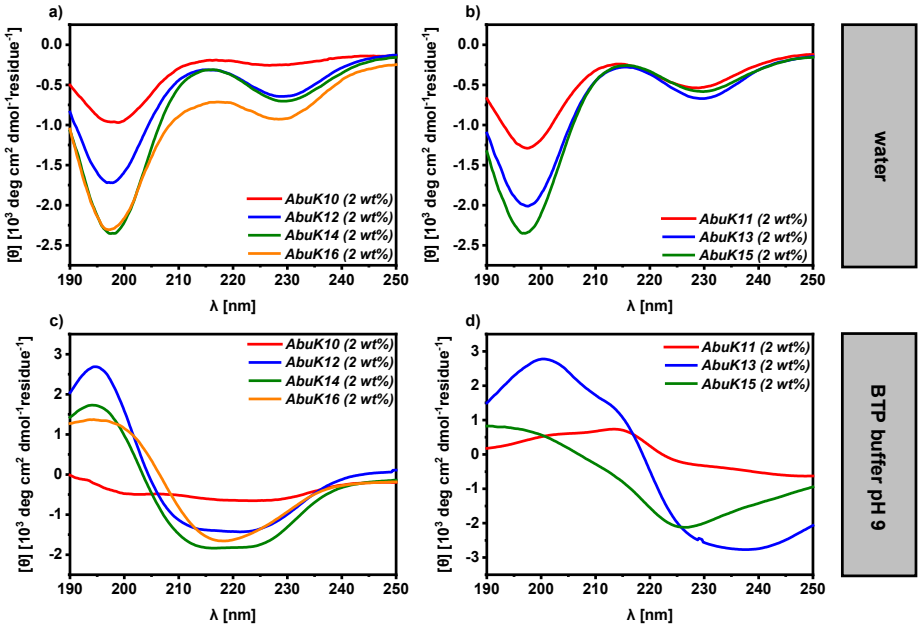

Figure S93: CD spectra of 2 wt% **AbuK10-AbuK16** in **a)** water and **b)** 50 mM Bis-tris propane + 150 mM NaCl, pH 9 recorded at 37 °C.

6.2 CD Spectroscopy: Salt effects and valency on secondary structure formation (AbuK16, MfeGlyK16, DfeGlyK16, TfeGlyK16)

To test the stability of secondary structure formation with regards to **AbuK16**, **MfeGlyK16**, **DfeGlyK16** and **TfeGlyK16** towards several types of salts, especially with respect to mono-/divalent cationic species, CD measurements were performed with different types of buffered conditions (**Figure S94**).

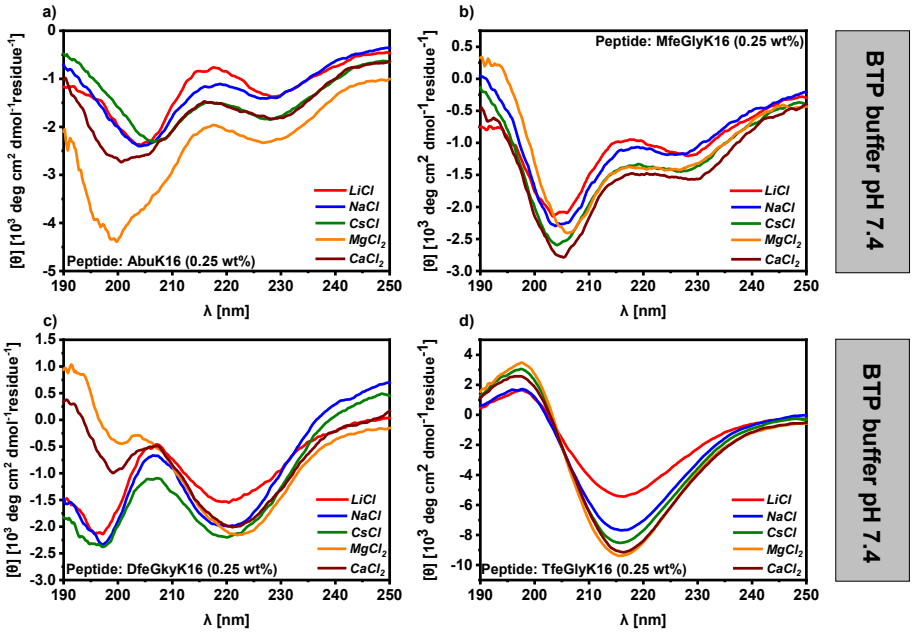

Figure S94: CD spectra of 0.25 wt% **a) AbuK16; b) MfeGlyK16; c) DfeGlyK16; d) TfeGlyK16** in 50 mM Bis-tris propane with 150 mM LiCl, NaCl, CsCl, $MgCl_2$ or $CaCl_2$, pH 7,4 recorded at 37 °C.

It was found that the CD signal intensity increased when rising the valency of salt as seen for LiCl compared to $MgCl_2$ and $CaCl_2$. Beside this finding, we conclude that all selected sequences were capable to undergo peptide folding despite selected cationic source.

6.3 CD Spectroscopy: Impact of non-aqueous solvents on secondary structure formation (AbuK16, MfeGlyK16, DfeGlyK16, TfeGlyK16)

We aimed to study peptide folding of synthetic oligopeptides (**AbuK16**, **MfeGlyK16**, **DfeGlyK16**, **TfeGlyK16**) dissolved in a polar protic (MeOH), aprotic (ACN) and fluorinated (TFE) solvent. Examination of secondary structures were executed to provide an overview about the structural potentials of these novel systems (see **Figure S95**).

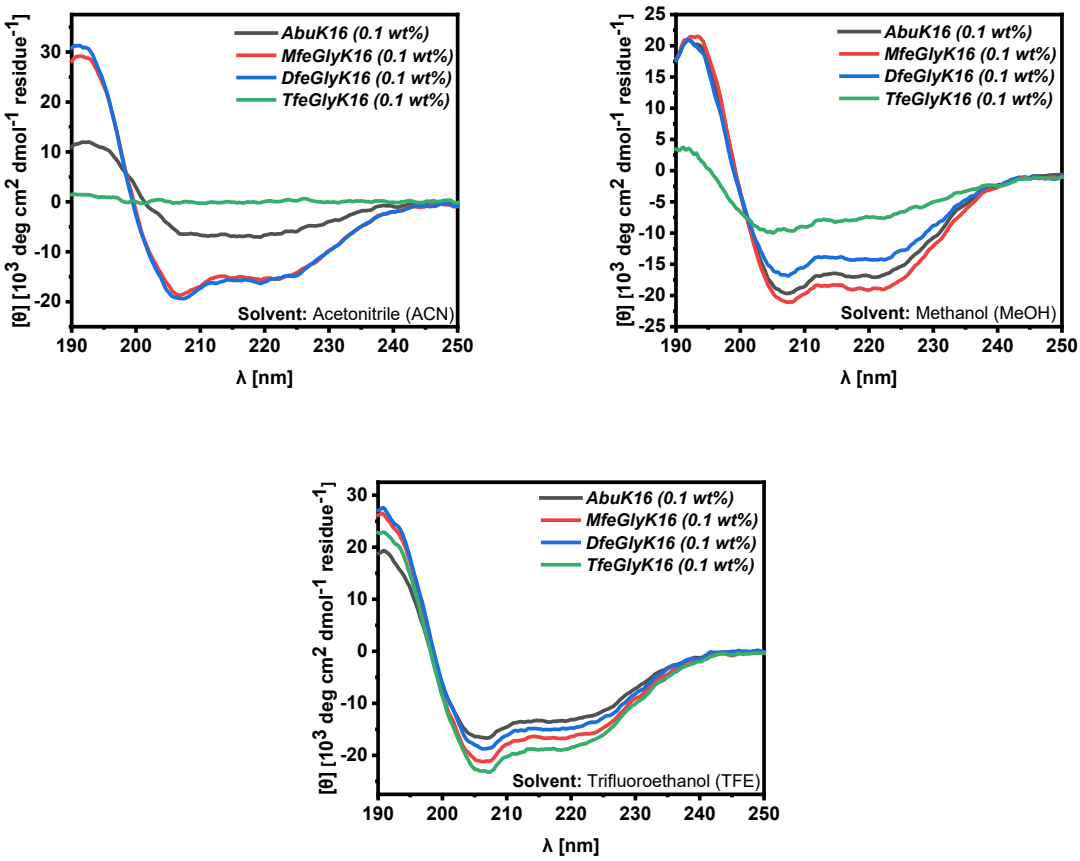

Figure S95: CD spectra of 0.1 wt% **AbuK16; MfeGlyK16; DfeGlyK16; TfeGlyK16** in Acetonitrile (ACN), methanol (MeOH) or 2,2,2-trifluoroethanol (TFE) recorded at 37 °C.

For most cases, the formation of α-helical structures was observed. With respect to selected solvents, these findings are in accordance with previous reports, highlighting stabilizing hydrogen bonding between the peptide-backbones and, simultaneously, weakening hydrophobic interactions as cause for helical assemblies.[13-16] As PPII helices were observed for **AbuK16** and **MfeGlyK16** in aqueous buffered conditions, we propose an enhancement in peptide-peptide hydrogen bonding due to MeOH, ACN and TFE. In pure ACN, we observed precipitation of the peptide **TfeGlyK16** as represented by a lack of a defined CD spectrum. Similar results were described by Shen *et al.* by exposing an enhanced fibril growth for the β-amyloid peptide by an increased amount of ACN in water.[17]

7. Characterization of reference sequence LeuK16

The aliphatic oligopeptide **LeuK16** was synthesized to distinguish between hydrophobic effects and fluorine-specific interactions. Therefore, the *Leu-Lys* repeating unit was reported as a core segment to produce comparably stiff hydrogel matrices.[18] We also characterized this peptide trough CD spectroscopy and estimated its hydrophobic properties (RP-HPLC assay) (**Figure S96**).

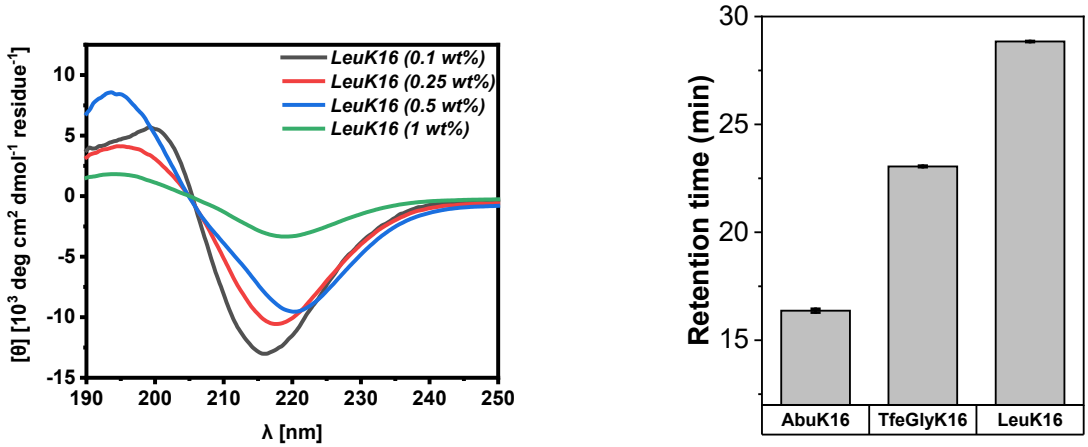

Figure S96: (left) CD spectra of 0.1- 1 wt% **LeuK16** in in 50 mM Bis-tris propane + 150 mM NaCl, pH 7,4 recorded at 37 °C; **(right)** Estimation of hydrophobicity of **LeuK16** (28.842 ± 0.025 min) in comparison to **AbuK16** (16.368 ± 0.087min) and **TfeGlyK16** (23.054 ± 0.031 min) [RP-HPLC assay].

The peptide **LeuK16** formed β-sheets in selected buffered system but was found to be significantly more hydrophobic than **TfeGlyK16** as determined through a RP-HPLC assay. This outcome it not surprising due to the larger size and branched pattern of the aliphatic side chain of Leu as compared to **TfeGly**.[19] Obviously, the enhanced hydrophobicity in combination to the side chain of leucine led to the formation to comparably stiffer hydrogel matrices than for **TfeGlyK16** at pH 7.4.

8. Detection of amyloid-like fibrils: Congo red (CR) UV-spectroscopy

To further confirm the presence of amyloid-like fibrils, we applied congo red (CR) UV-spectroscopy to **AbuK16**, **MfeGlyK16**, **DfeGlyK16** and **TfeGlyK16**. As shown in **Figure S97**, the binding of CR to amyloid-like fibrils leads to an increase in UV intensity (550 - 450 nm) of this dye. Hence, we observed an overall increase in CR-derived UV absorbance only for **DfeGlyK16** & **TfeGlyK16** at a concentration of 0.5 wt% (pH 7.4), resembling their ability to form β-sheets at given conditions. For **AbuK16** and **MfeGlyK16**, the detected values of UV absorbance equaled to the spectra obtained for the buffer sorely containing CR (black line). Consequently, an intercalation of this dye in fibrillar assemblies was not found. To disclaim any influence of the peptide's nature on determined UV signal intensity, we also measured UV spectra of these peptide only in BTP buffer. The slight increase in UV absorbance at 300 nm is derived from the C-terminal **[4]Abz** label.

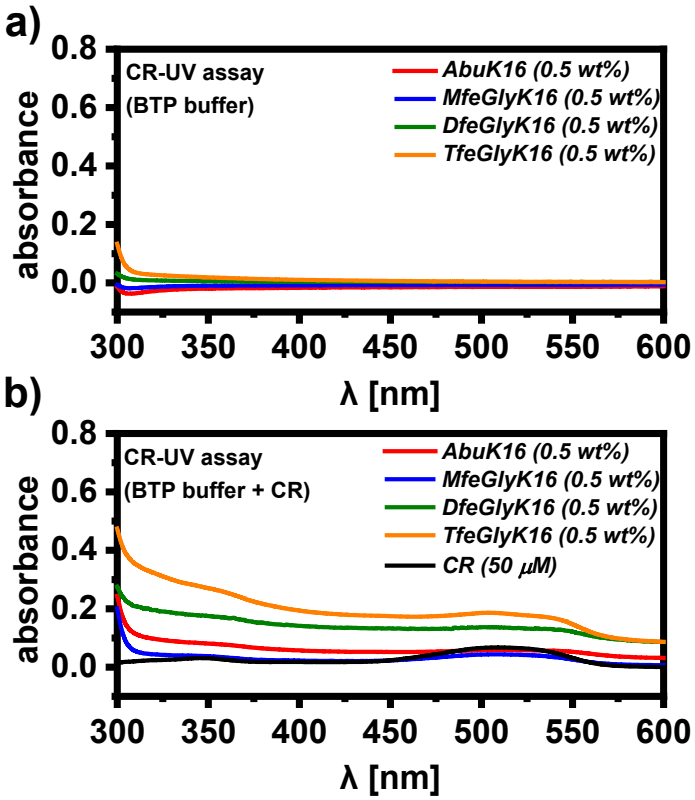

Figure S97: UV spectra (600 - 300 nm) of amphipathic peptides incubated in **a)** 50 mM bis-tris propane + 150 mM NaCl, pH 7,4 and **b)** in 50 mM bis-tris propane + 150 mM NaCl, pH 7,4 + 50 µM CR. Additionally, a blank sample only containing buffer and congo red was recorded as reference (black line). All samples were measured after prior incubation at 37°C overnight (minimum 15 h).

9. Further cryoEM micrographs (AbuK14, AbuK16, MfeGlyK16, DfeGlyK16, TfeGlyK16)

AbuK14 – 2 wt% (10-fold dilution)

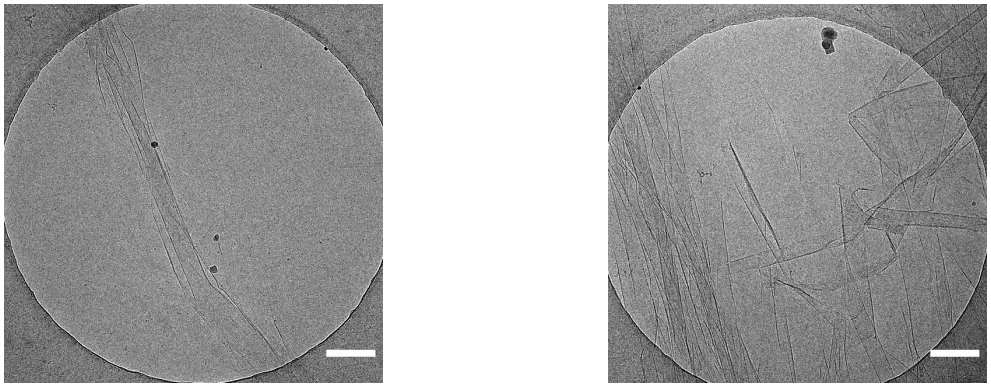

Figure S98: Cryo-EM micrographs of **AbuK14** (2 wt% (10-fold dilution)) dissolved in 50 mM Bis-tris propane + 150 mM NaCl, pH 7.4. The sample was prepared in a concentration of 2 wt% to trigger β-sheet formation and then diluted to 0.2 wt%. The scale bar denotes 200 nm each

AbuK16 - 0.25 wt% + 2 wt% (10-fold dilution)

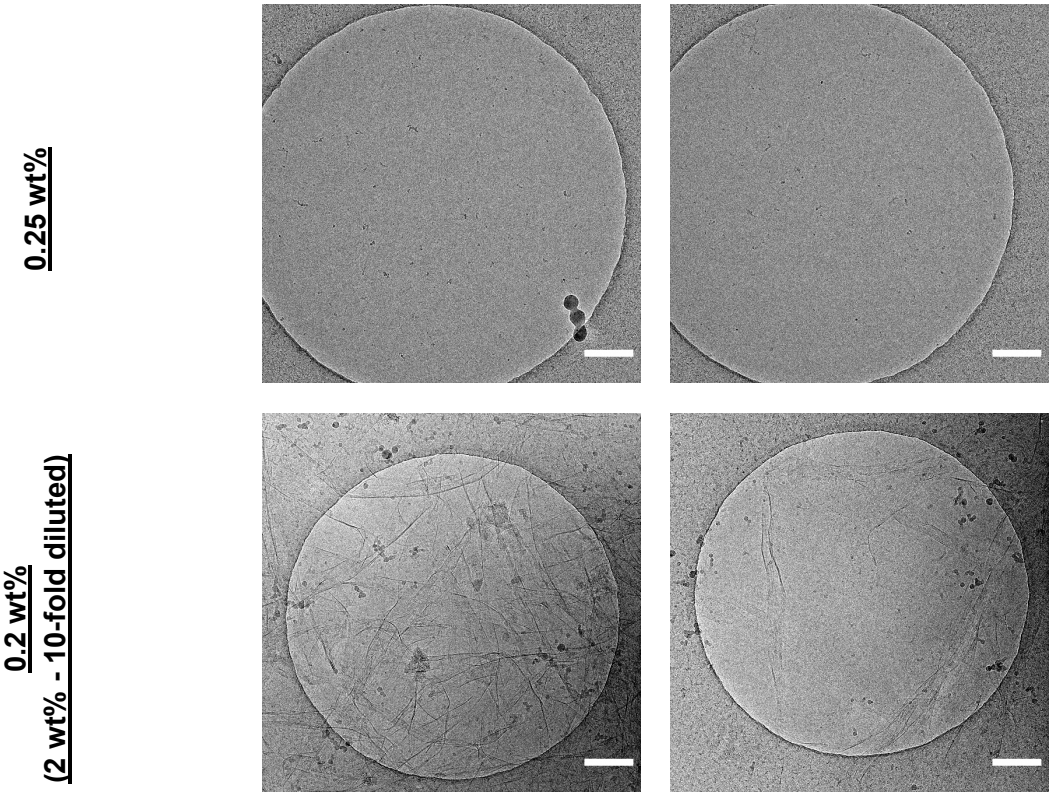

Figure S99: Cryo-EM micrographs of **AbuK16** (0.25 wt%) & (2 wt% (10-fold dilution)) dissolved in 50 mM Bis-tris propane + 150 mM NaCl, pH 7.4. The scale bar denotes 200 nm each.

MfeGlyK16 – (0.25 wt%)

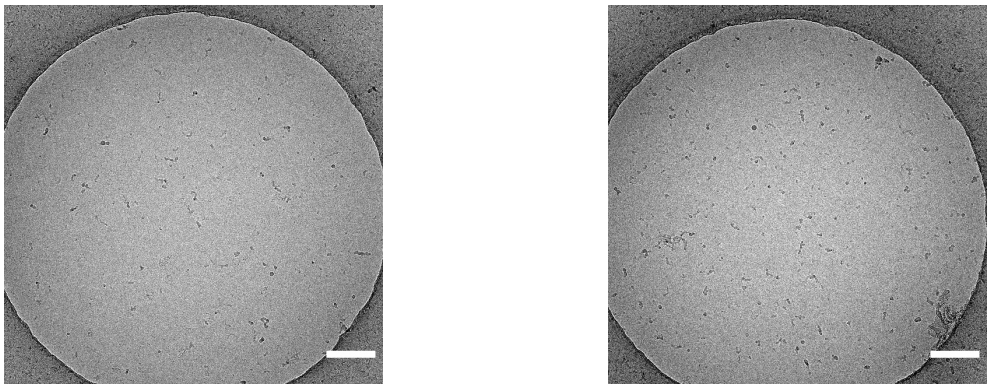

Figure S100: Cryo-EM micrographs of **MfeGlyK16** (0.25 wt%) dissolved in 50 mM Bis-tris propane + 150 mM NaCl, pH 7.4. The scale bar denotes 200 nm each.

DfeGlyK16 – (0.25 wt%)

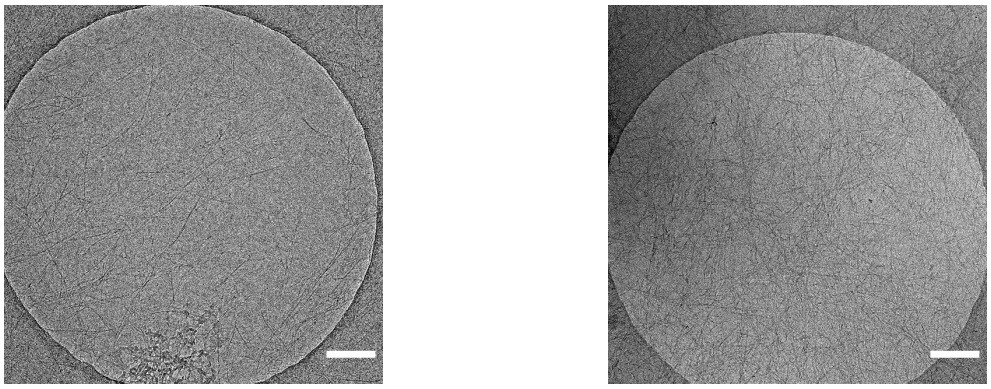

Figure S101: Cryo-EM micrographs of **DfeGlyK16** (0.25 wt%) dissolved in 50 mM Bis-tris propane + 150 mM NaCl, pH 7.4. The scale bar denotes 200 nm each.

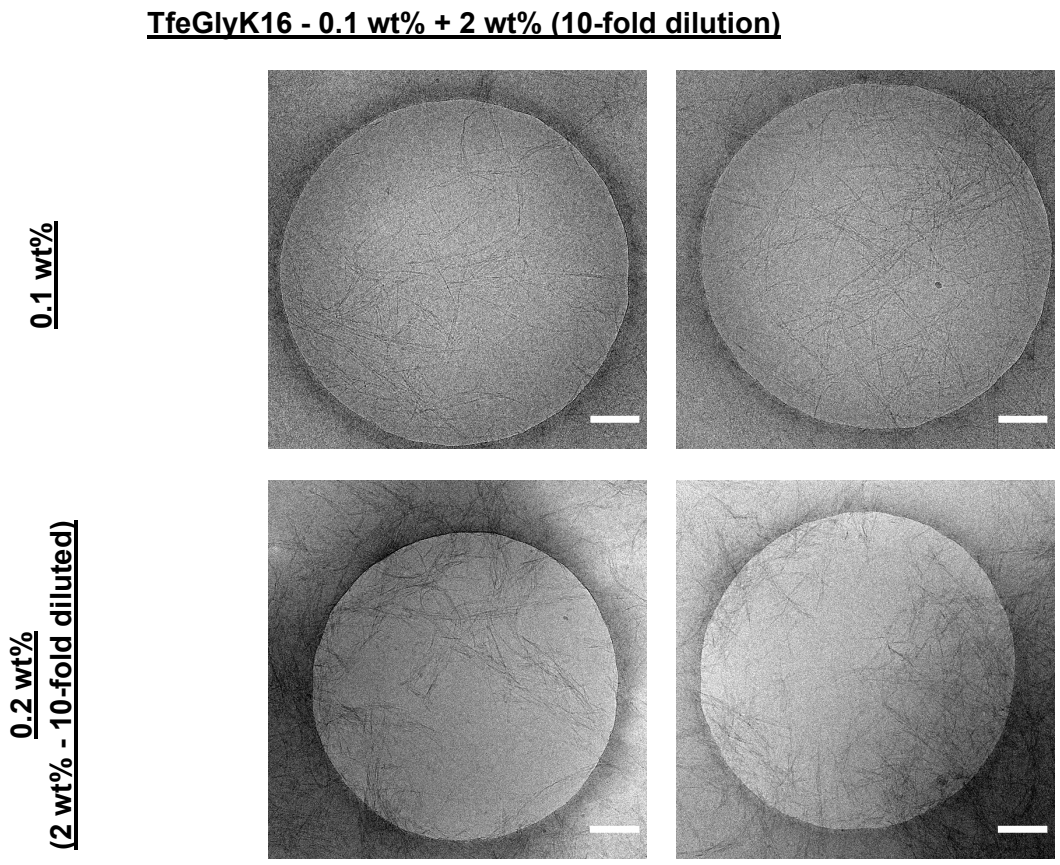

Figure S102: Cryo-EM micrographs of **TfeGlyK16** (0.1 wt%) & (2 wt% (10-fold dilution)) dissolved in 50 mM Bis-tris propane + 150 mM NaCl, pH 7.4. The scale bar denotes 200 nm each.

10. Inversion tests of peptide-based hydrogels

A protocol for the inversion test was previously reported by our group.[20] Peptide hydrogels composing of lyophilized samples **AbuK16**, **DfeGlyK16**, **TfeGlyK16** and **LeuK16** were dissolved in glass vial, mixed for 30 s to obtain a homogeneous mixture and incubated overnight with gentle shaking. It was avoided to implement any mechanical stress (e.g. centrifugation) in order to inhibit disruption in hydrogel formation. On the next day, sample vials were inverted for 24 h at room temperature. This was done to initially gain an idea about potential rigidity of resulting fibril matrices (**Figure S103**).

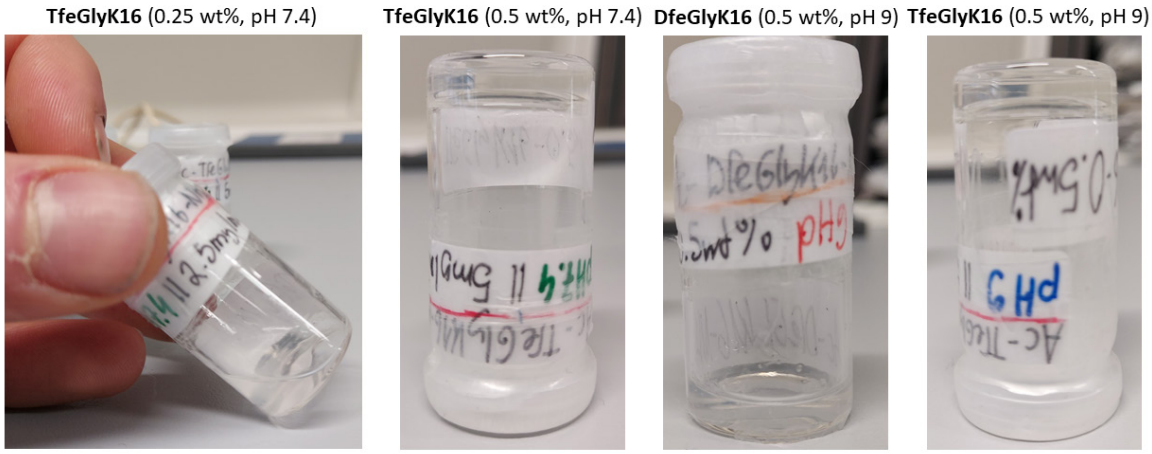

Figure S103: Selected photographs of hydrogel samples consisting of the peptide sequences **DfeGlyK16** & **TfeGlyK16.** The diameter of each glass vial was **10 mm**.

11. Rheological characterization of aliphatic oligopeptides – Further data

To determine the optimal deformation for oscillatory rheology experiments, amplitude sweeps are performed prior to each experiment. The frequency is fixed at 1 Hz and the strain γ is varied from 0.01 to 10%. The linear viscoelastic regime (LVE) is limited by the critical deformation γ^*. For $\gamma < \gamma^*$, we observe a plateau. To measure the linear response in oscillatory measurements without irreversibly breaking the three-dimensional network, the strain should be chosen such that it is smaller than γ^*. For all oscillatory measurements, γ was set to 0.1%, which is within the LVE.

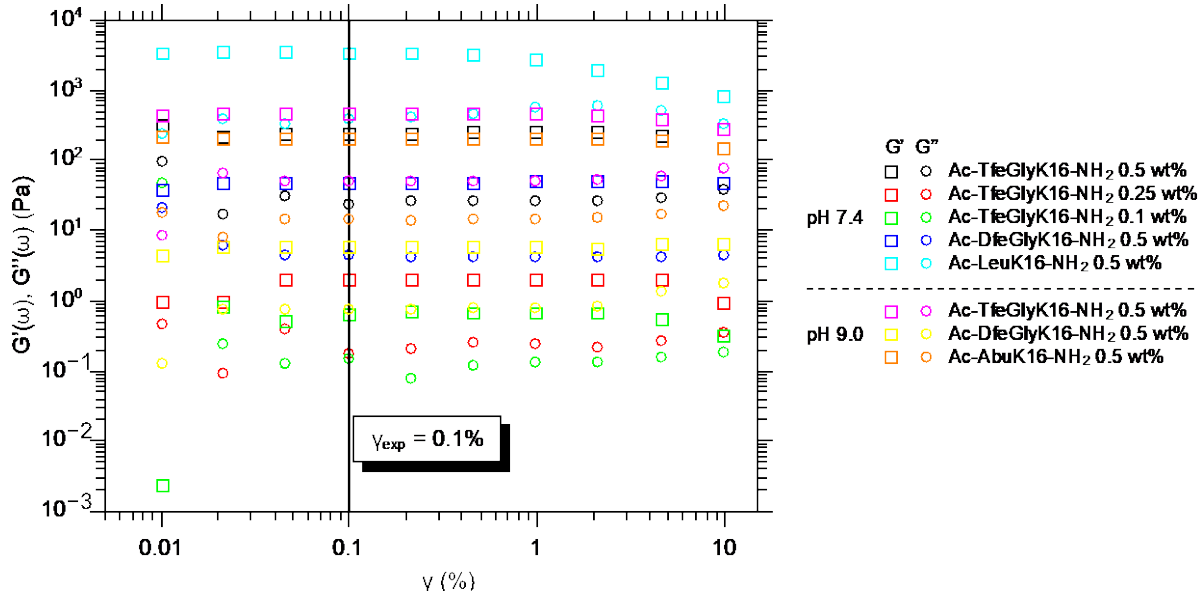

Figure S104: Amplitude sweeps for all measured samples, performed at T = 37°C and at constant angular frequency ω = 0.628 rad/s. To stay in the linear viscoelastic regime (LVE), the strain γ for all subsequent oscillatory measurements was set to γ_{exp} = 0.1%.

To confirm the surprising findings about the behavior of **TfeGlyK16** [Ac-TfeGlyK16-NH_2] in relation to **DfeGlyK16** [Ac-DfeGlyK16-NH_2] upon increasing the pH, the measurements were repeated with newly prepared samples. The results of the frequency sweeps are shown in **Figure S105**. The absolute values differ significantly, most likely due to small irregularities in concentration and/or time between preparation and measurement. The principle finding concerning the reversal in the trend of the plateau modulus G_0 however remains the same. For a detailed representation, we plotted the plateau modulus and mesh size as a function of the number of fluorine atoms on the peptide side chain at pH 9 (**Figure S106**).

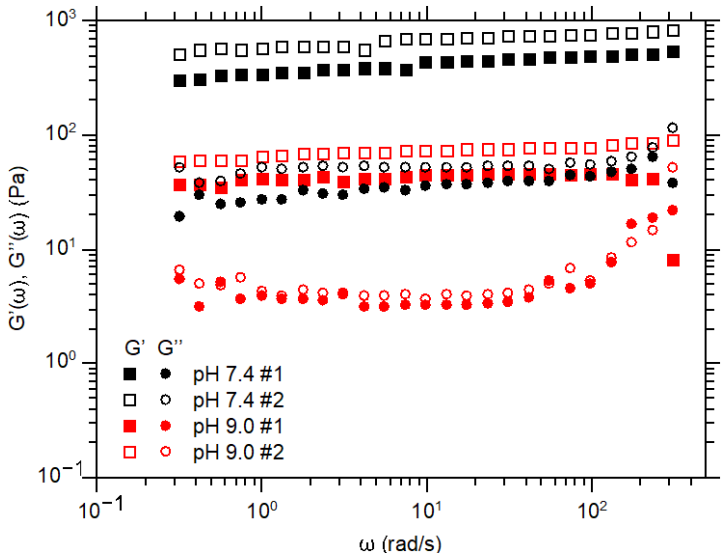

Figure S105: Repeated frequency sweeps for **TfeGlyK16** [Ac-TfeGlyK16-NH_2] at pH 7.4 and 9.0. The absolute values differ substantially, but the trends remain unchanged.

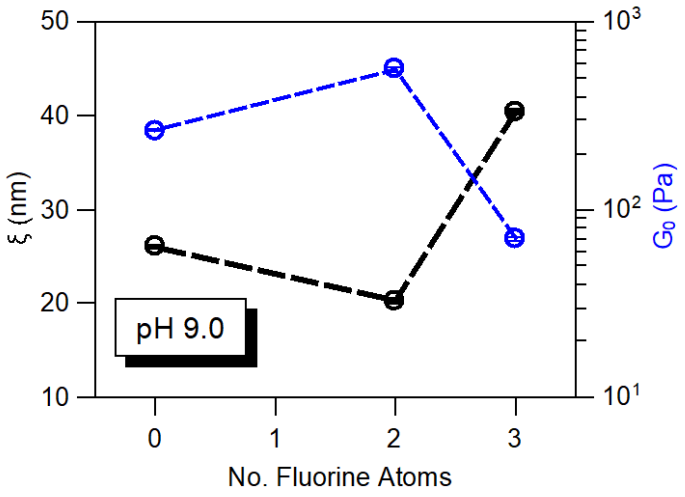

Figure S106: Plateau moduli G_0 (blue symbols) and mesh sizes ξ (black symbols) for the **GlyK16** peptides (**0-AbuK16**, **2-DfeGlyK16**, **3-TfeGlyK16**) shown as a function of the number of fluorine atoms on the side chain.

12. MD simulations of (polyfluorinated) amphipathic peptides

Here, we present atom names , atom types (derived from the parameter sets of CHARMM36m and CGenFF), optimized partial atomic charges, and topologies of **Abu**, **MfeGly**, **DfeGly**, and **TfeGly**. For optimization, partial charges on the protein backbone atoms (top and bottom groups) are fixed to that given in the CHARMM36m force field, to be consistent with other amino acids, and partial charges on the side chain atoms (the middle group) are varied to reproduce the QM water interaction energy.

12.1 Optimized partial charges on Abu

```
RESI ABU           0.000
GROUP
ATOM N     NH1    -0.47  !      |
ATOM HN    H       0.31  !   HN-N
ATOM CA    CT1     0.07  !      |    HB1 HG1
ATOM HA    HB1     0.09  !      |    |   |
GROUP                    !   HA-CA--CB--CG-HG3
ATOM CB    CT2    -0.162 !      |    |   |
ATOM HB1   HA2     0.09  !      |    HB2 HG2
ATOM HB2   HA2     0.09  !    O=C
ATOM CG    CT3    -0.288 !      |
ATOM HG1   HA3     0.09
ATOM HG2   HA3     0.09
ATOM HG3   HA3     0.09
GROUP
ATOM C     C       0.51
ATOM O     O      -0.51
```

12.2 Optimized partial charges on MfeGly

```
RESI MFA           0.000
GROUP
ATOM N     NH1    -0.47  !      |
ATOM HN    H       0.31  !   HN-N
ATOM CA    CT1     0.07  !      |    HB1 HG1
ATOM HA    HB1     0.09  !      |    |   |
GROUP                    !   HA-CA--CB--CG-FG1
ATOM CB    CT2    -0.120 !      |    |   |
ATOM HB1   HA2     0.090 !      |    HB2 HG2
ATOM HB2   HA2     0.090 !    O=C
ATOM CG  CG322    -0.063 !      |
ATOM HG1  HGA6     0.111
ATOM HG2  HGA6     0.111
ATOM FG1  FGA1    -0.219
GROUP
ATOM C     C       0.51
ATOM O     O      -0.51
```

12.3 Optimized partial charges on DfeGly

```
RESI DFA            0.000
GROUP
ATOM N      NH1    -0.47  !       |
ATOM HN     H       0.31  !   HN-N
ATOM CA     CT1     0.07  !      |    HB1 HG1
ATOM HA     HB1     0.09  !      |    |   |
GROUP                     !   HA-CA--CB--CG-FG2
ATOM CB     CT2    -0.127 !      |    |   |
ATOM HB1    HA2     0.090 !      |    HB2 FG1
ATOM HB2    HA2     0.090 !    O=C
ATOM CG   CG312     0.228 !      |
ATOM HG1   HGA7     0.101
ATOM FG1   FGA2    -0.191
ATOM FG2   FGA2    -0.191
GROUP
ATOM C      C       0.51
ATOM O      O      -0.51
```

12.4 Optimized partial charges on TfeGly

```
RESI TFA            0.000
GROUP
ATOM N     NH1     -0.47  !      |
ATOM HN    H        0.31  !   HN-N
ATOM CA    CT1      0.07  !      |    HB1 FG1
ATOM HA    HB1      0.09  !      |    |   |
GROUP                     !   HA-CA--CB--CG-FG3
ATOM CB    CT2     -0.093 !      |    |   |
ATOM HB1   HA2      0.090 !      |    HB2 FG2
ATOM HB2   HA2      0.090 !    O=C
ATOM CG  CG302      0.333 !      |
ATOM FG1  FGA3     -0.140
ATOM FG2  FGA3     -0.140
ATOM FG3  FGA3     -0.140
GROUP
ATOM C     C        0.51
ATOM O     O       -0.51
```

12.5 MD simulations – further data

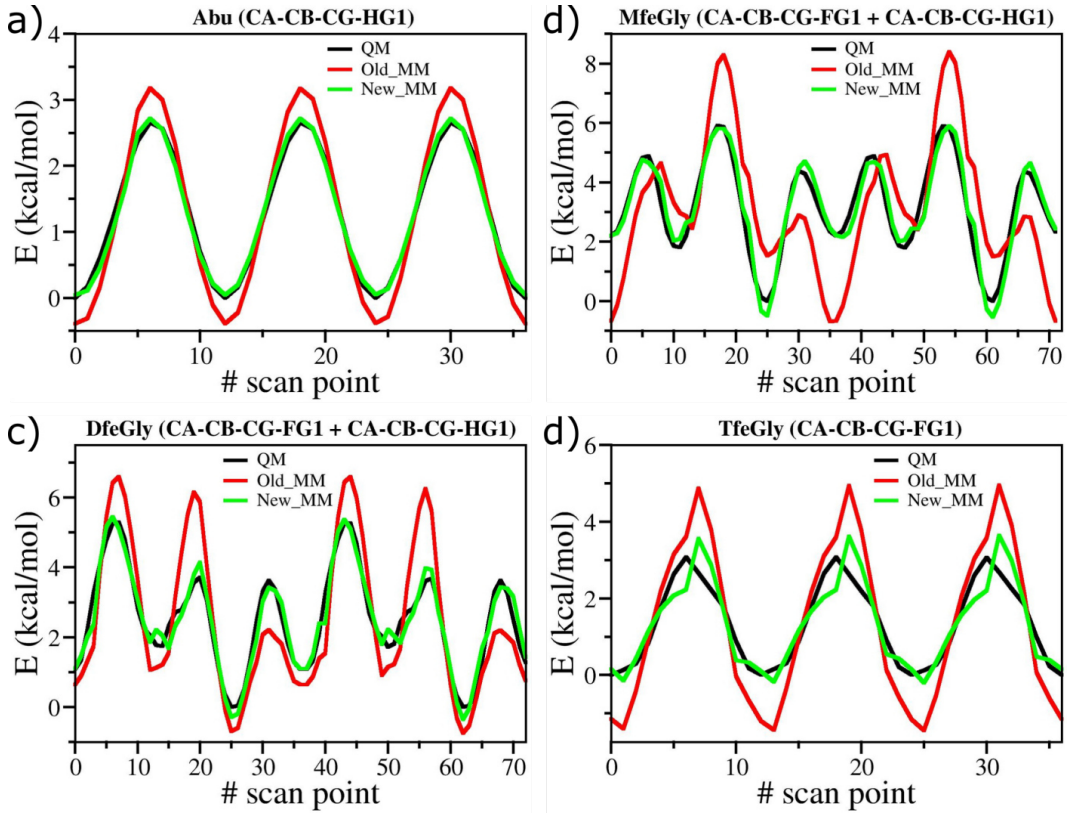

Figure S107: Optimization of dihedral angle(s) for **a**) **Abu**, **b**) **MfeGly**, **c**) **DfeGly**, and **d**) **TfeGly**. Atoms defining a dihedral angle are listed at the top of each plot. For **MfeGly**, **DfeGly**, and **TfeGly**, two dihedral angles (C_α–C_β–C_γ–F and C_α–C_β–C_γ–H) are simultaneously optimized. For each dihedral angle, a total 36 QM energy scans, at intervals of 10º, are performed. Energies obtained from QM calculations are shown as black lines. Energies obtained from classical molecular mechanics using the force field parameters initially obtained from the CGenFF program are shown as red lines (Old_MM), whereas those using the optimized force field parameters are shown as green lines (New_MM). The optimized dihedral angle parameters are given in previous chapter.

Table S23: Optimized parameters for CHARMM dihedral energy function: $V_\varphi = k_\varphi[1 + \cos(n\varphi - \delta)]$. Note that the Einstein summation convention is used.

Amino Acid	Dihedral	k_φ	n	δ
Abu	CA-CB-CG-HG1	0.4599	3	180.00
MfeGly	CA-CB-CG-FG1	2.1197	1	180.00
		0.1785	2	0.00
		2.6341	3	0.00
		0.3909	4	180.00
		0.2995	5	180.00
	CA-CB-CG-HG1	0.1418	1	0.00
		0.8202	2	180.00
		2.7214	3	180.00
		0.2611	5	0.00
DfeGly	CA-CB-CG-FG1	0.3960	1	0.00
		1.3667	3	180.00
		0.3155	4	0.00
		0.5123	6	0.00
	CA-CB-CG-HG1	1.0158	1	0.00
		0.6083	2	0.00
		0.6043	3	0.00
		0.7729	4	0.00
		0.5764	6	180.00
TfeGly	CA-CB-CG-FG1	1.3606	3	180.00

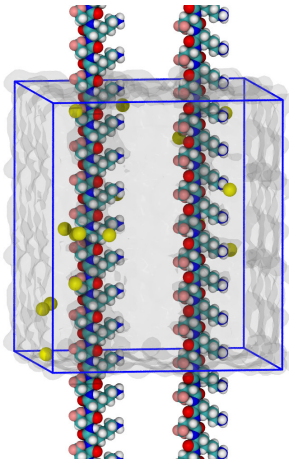

Figure S108: Simulation box (blue rectangle) containing two periodic **TfeGlyK16** strands, shown in the space-filling representation, colored according to the atom type: H (white), C (cyan), N (blue), F (pink). Cl^- counterions are shown as yellow spheres, whereas water is shown as semi-transparent, continuum for clarity.

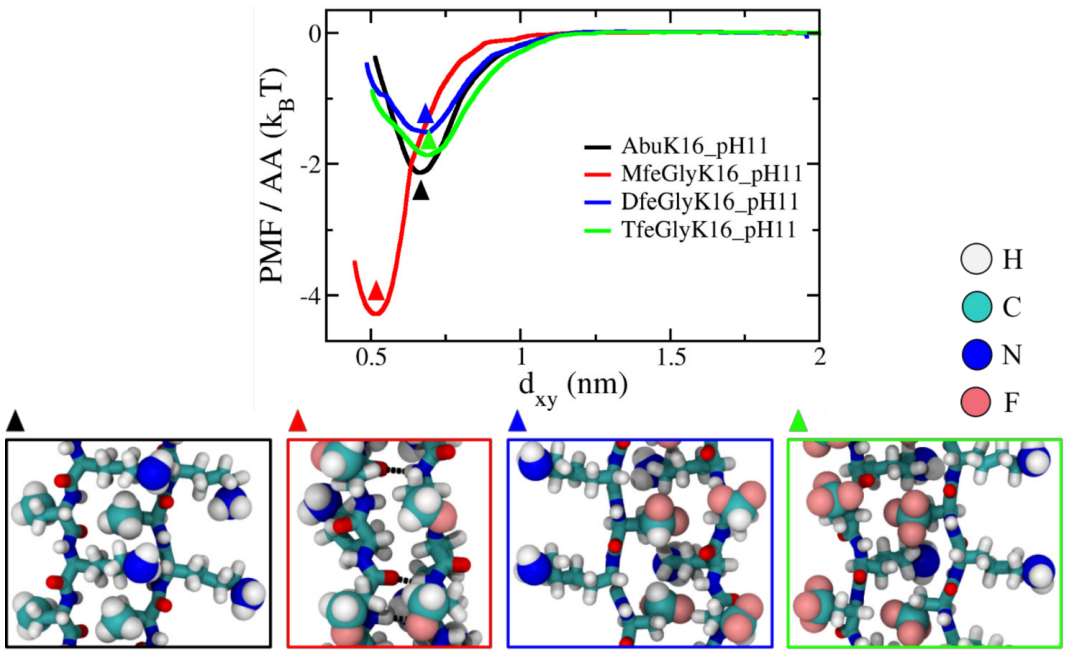

Figure S109: **a**) The potential of mean force (PMF) per amino acid (AA) as a function of inter-strand separation d_{xy} at pH11 (charge neutral Lys), depicting the free energy profile of interaction between two peptide strands for side chains with different degrees of fluorination. The free-energy minimum for each case is marked by a triangle. **b**) Structures corresponding to the free energy minimum for each case are shown in the ball-stick representation; the terminal group of each side chain is highlighted in the space-filling representation. Atom are colored as: H (white), C (cyan), N (blue), O (red), F (pink). Colors of enclosing boxes are the same as colors of the PMF profiles in **a**. Backbone-backbone hydrogen bonds observed for **MfeGlyK16** are shown as black, dashed lines.

13. Small-angle X-ray scattering (SAXS)

Time-resolved SAXS measurements were employed to provide information on changes of the fibril cross-section dimension and shape. For this purpose, SAXS measurements of samples **AbuK16**, **MfeGlyK16**, **DfeGlyK16** and **TfeGlyK16** with peptide concentrations of 0.1, 0.5, 1 and 2 wt% were performed. The measurements were started immediately after sample preparation by mixing freeze-dried peptide powders with buffer solution. At the lowest concentration of 0.1 wt%, none of the samples display a significant SAXS intensity within 12 h. At the next higher concentration of 0.5%, the scattering intensity of **TfeGlyK16** was sufficiently high to obtain a reasonable SAXS pattern while the intensity of **DfeGlyK16** was only slightly larger than that of the buffer, and the intensities of **MfeGlyK16** and **AbuK16** were approximately the same as the buffer solution. For illustration, examples of raw SAXS data of **AbuK16**, **MfeGlyK16**, **DfeGlyK16** and **TfeGlyK16** (each at a concentration of 0.5%, measurement time of 5 min, and total incubation time of 50 min), the scattering of the buffer and the difference between raw data and buffer are provided in **figure S110** (panels in rows one and two). Much larger are the scattering intensities of the corresponding data for **DfeGlyK16** and **TfeGlyK16** at concentrations of 1 wt% and 2 wt% (see panels in rows three and four). Here, the measurement time for a data frame was set to 1 min to get insight in the kinetics of fibril formation.

The scattering contrast, defined here as the difference between the scattering length density of amyloid fibrils[21] (ρ_2 = 12.7 ± 10^{10} cm^{-2}) and the scattering length density of buffer (ρ_1=9.37 ± 10^{10} cm^{-2}), is ρ_2-ρ_1 =3.33 ± 10^{10} cm^{-2}. This low value makes it plausible that a relatively high peptide concentration is necessary to detect the fibrils with SAXS. For the higher concentrations, reasonable signal-to-noise ratios were observed between a minimum and a maximum q-value of q_{min} = 0.08 nm^{-1} and q_{max} = 4.0 nm^{-1}, respectively. Therefore, the SAXS data of the present study allow to obtain information in the size range of about π/q_{max} = 0.8 nm to π/q_{min} = 40 nm.

No Guinier region[22] is visible in the SAXS curves at low q-values as was expected for fibrils much longer than our upper size detection limit. Since the overall fibril length $l \gg q_{min}^{-1}$, the SAXS form factor $P(q)$ can be factorized into a product of an axial form factor $P_a(q)$ (factors the length of the filaments) and a cross-section form factor $P_c(q)$ (factors the fiber cross-section). The model for interpretation of the SAXS pattern can be written as[23]

$$I(q) = N(\rho_2 - \rho_1)^2 V^2 P_a(q) P_c(q)$$

where *N* is the number density of the fibrils (in fibers per cm^3) and *V* the volume of a fibril (in nm^3). The scattering intensities scale approximately with q^{-1} for **TfeGlyK16** and with q^{-2} for **DfeGlyK16** at low *q*-values (indicated as straight lines in **figure S111** and **figure S112**). These scaling behavior hints to a more circular cross-section for the fibrils of **TfeGlyK16** and a flat cross-section for **DfeGlyK16**. Therefore, we started data evaluation with the model of a circular cylinder[23] for interpretation of the scattering data of **TfeGlyK16** and an extended parallelepiped[24] for **DfeGlyK16**, respectively (not shown). An alternative model is a long cylinder with an elliptical cross-section. Indeed, the elliptical cylinder model was applicable for all scattering curves and provides statistically better curve fits than our first approach as indicated by lower χ-values. The axial form factor in the chosen model is

$$\mathrm{P_a(q)} = \left[\frac{2\mathrm{Si}(ql)}{ql} - \frac{4\,sin^2(ql/2)}{q^2\,l^2}\right]$$

with the sine integral $\mathrm{Si(x)} = \int_0^{\mathrm{x}} \mathrm{t}^{-1}\sin(\mathrm{t})\,\mathrm{dt}$. The cross-section form factor is

$$\mathrm{P_c(q)} = \frac{2}{\pi}\int_0^{\pi/2}\left(\frac{2\mathrm{J_1}\left(\mathrm{q}\sqrt{(\mathrm{a}\,\sin\phi)^2 + (\mathrm{b}\,\cos\phi)^2}\right)}{\mathrm{q}\sqrt{(\mathrm{a}\,\sin\phi)^2 + (\mathrm{b}\,\cos\phi)^2}}\right)^2 d\phi$$

where $\mathrm{J_1(x)}$ is the first order Bessel function, *a* is the major semiaxis of the elliptical cross section and *b* is the minor semiaxis. The fibril's cross-section area is $A = \pi a\,b$ and the fibril volume is $V = \mathrm{A}\,l$. It should be noted that this model was employed recently by Lattanzi *et al.*[23] for interpretation of SAXS data of the fibril structure of amyloid ß 42 and by Schmitt *et al.* for interpretation of the SAXS data from gelation of cellulose nanofibrils.[25]

When employing this model, the data were represented sufficiently by the curve fits as shown in Figure **figure S111** (symbols and solid line) for **TfeGlyK16** at 0.5%. Therein a true to scale sketch of the fiber model is provided with a length of *l* = 200 nm and a cross-section with a major axis of a = 3.7 nm and a minor axis of b = 0.95 nm (see inset). For clarity, *l* and *b* were held constant at all curve fittings to avoid ambiguous results.

Next, in the time-resolved experiments of **DfeGlyK16** and **TfeGlyK16**, we found an increase in the scattering intensities and a slight change of the curve shape as a function of time. Examples for data and corresponding curve fits of measurement frames *n* = 1 (recorded ca. 120 s after sample preparation) and *n* = 50 (recorded 3000 s after sample preparation), are shown in Figure **figure S112** (symbols and solid lines, respectively). We found an increase of the major semi axis from *a* = 2.7 nm to 11.0 nm for sample **DfeGlyK16** at a concentration of 1% and from 2.9 nm to 4.4 nm at 2%. In contrast, the short semi-axis of the cross section is constant at *b* = 0.85 nm. An increase of the *a*-axis from 2.8 nm to 3.2 nm was determined for

sample **TfeGlyK16** at 1% and from 2.8 nm to 3.1 nm at 2%. Here, the short semi-axis of the cross section is constant at *b* = 0.95 nm. An overview on the differences of the cross-sections between data frame 1 and 50 is provided as sketch in **figure 4f** in the main paper.

In the following we tentatively try to quantify the time-dependency of the major semi axis $a(t)$, the fibril cross-section area $A(t)$, the fibril number density $N(t)$ and the weight concentration $c(t)$ with the exponential functions

$$a(t) = a_\infty\left[1 - e^{-k_a(t-t_a)}\right]$$
$$A(t) = A_\infty\left[1 - e^{-k_A(t-t_A)}\right]$$
$$N(t) = N_\infty\left[1 - e^{-k_N(t-t_N)}\right]$$
$$c(t) = c_\infty\left[1 - e^{-k_c(t-t_c)}\right]$$

Were a_∞, A_∞, $N_\infty$and c_∞ are the parameter values extrapolated to infinite incubation times, k_a, k_A, k_N and $k_c$are rate constants of the parameters and t_a, t_A, t_N and t_c are delay times.

First, we applied $a(t)$ for quantification of the changes of the major semiaxis (see **figure S114**). For **DfeGlyK16** the curve fits provide $a_\infty = 10.5$ nm and 4.3 nm, k_b = 1.5 × 10^{-3} s^{-1} and 2.7 × 10^{-3} s^{-1} at concentrations of 1% and 2%, respectively. For **TfeGlyK16** the fits provide $a_\infty = 3.1$ nm and 3.0 nm, k_b = 12.9 × 10^{-3} s^{-1} and 12.8 × 10^{-3} s^{-1} at concentrations of 1wt% and 2wt%, respectively. The t_a were zero for all samples, indicating that fibril formation starts immediately at time of sample preparation.

The data for the cross-section area are calculated by $A(t) = \pi\, \boldsymbol{b}\, a(t)$ with constant values of *b* = 0.85 nm (**DfeGlyK16**) and 0.95 nm (**TfeGlyK16**) providing A_∞-values of 28.1 nm^2 (1wt% **DfeGlyK16**), 11.6 nm^2 (2wt% **DfeGlyK16**), 9.4 nm^2 (1wt% **TfeGlyK16**) and 9.0 nm^2 (2wt% **TfeGlyK16**). The k_A- and t_A-values are obviously the same as the k_a- and t_a-values because *b* is time independent.

The fibril number density kinetics is described by N_∞- and k_N-values of 0.8 × 10^{15} cm^{-3} and 4.7 × 10^{-3} s^{-1} (1% **DfeGlyK16**), N_∞= 5.2 × 10^{15} cm^{-3} and k_N=4.7 × 10^{-3} s^{-1} (2% **DfeGlyK16**), N_∞= 4.2 × 10^{15} cm^{-3} and k_N=11.2 × 10^{-3} s^{-1} (1% **TfeGlyK16**) and N_∞= 7.4 × 10^{15} cm^{-3} and k_N=9.7 × 10^{-3} s^{-1} (2% **TfeGlyK16**). It should be noted here that the values of N_∞- and k_N-values must be considered as apparent values because the $N(t)$ data were calculated under the assumption of a constant fibril length of 200 nm. Sine the fibrils are longer, the values for $N(t)$ are most likely too high, as $N(t)$ scales inverse with the length of the fibrils.

The data of the weight concentration of the fibrils were calculated by

$$c(t) = \rho N(t) A(t) l$$

where ρ is the density of the fibrils for which a value of 1.45 g cm^{-3} is used.[21] The kinetics of the fibril weight concentration is described by c_∞- and k_c-values of 6.4 mg ml^{-1} and 1.9 × 10^{-3} s^{-1} (1% **DfeGlyK16**), c_∞= 17.7 mg ml^{-1} and k_c=2.0 × 10^{-3} s^{-1} (2% **DfeGlyK16**), c_∞= 11.3 mg ml^{-1} and k_c=11.2 × 10^{-3} s^{-1} (1% **TfeGlyK16**) and c_∞= 18.9 mg ml^{-1} and k_c=14.5 × 10^{-3} s^{-1} (2% **TfeGlyK16**). The weight concentration does in contrast to the number density not dependent on a correct value of the fibril length because for a given SAXS intensity the $N(t) \sim l^{-1}$ and $c(t) \sim l$, which means that *l* cancels out in determination of the weight concentration.

Of interest is a comparison of the calculated values c_∞ with the weighed-in peptide concentrations to estimate the amount of conversion of monomeric to fibrillar peptide. Conversions of 0.65% of 1.0% and 1.77% of 2.0% were found for **DfeGlyK16**. For these differences it can be assumed that 0.35% and 0.22% of the peptide are still present in form of monomer.

Conversions of 1.13% of 1.0% and 1.89% of 2.0% were found for **TfeGlyK16**. These values indicate a complete conversion of monomeric peptide to fibrils for **TfeGlyK16**. It should be noted that the uncertainty in determination of the SAXS-intensity[26] and therefore the concentration determination of peptides with SAXS is in the order of ±10%.

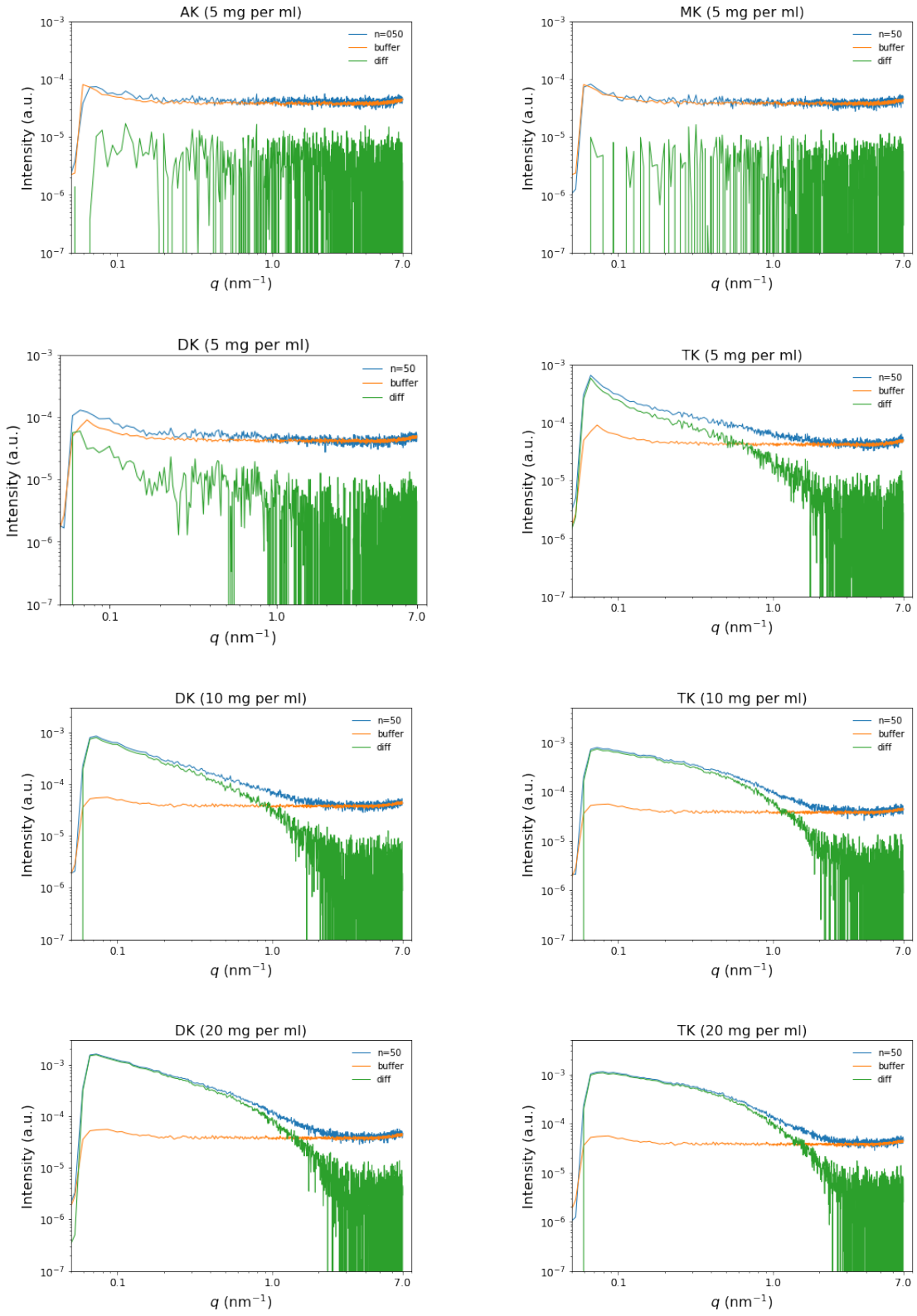

Figure S110: (First two rows) SAXS raw data of **AK (AbuK16)**, **MK (MfeGlyK16)**, **DK (DfeGlyK16)** and **TK (TfeGlyK16)** at a concentration of 5 mg per ml (0.5 wt%) (blue curves), SAXS of the buffer solution (orange) and the differences between raw data and buffer (green). (Third and fourth row) Corresponding data of **DK (DfeGlyK16)** and **TK (TfeGlyK16)** at concentration of 10 mg (1 wt%) and 20 mg (2 wt%) per ml, respectively.

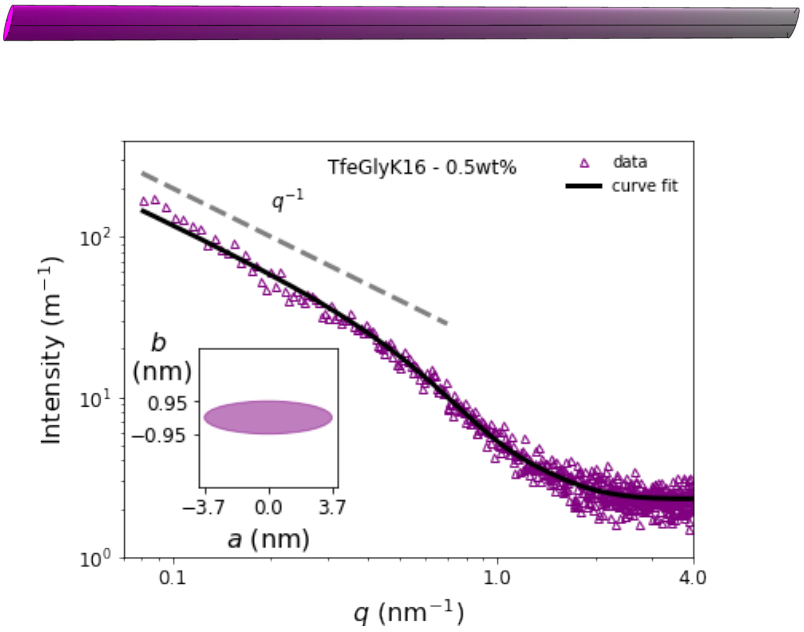

Figure S111: (top) true to scale model used for **TfeGlyK16**. (bottom) SAXS data and model curve for **TfeGlyK16** at a concentration of 0.5 wt% (symbols and line, respectively). Scaling of the intensity proportional to q^{-1} is indicted as straight line. (Inset) cross-section of the fibril.

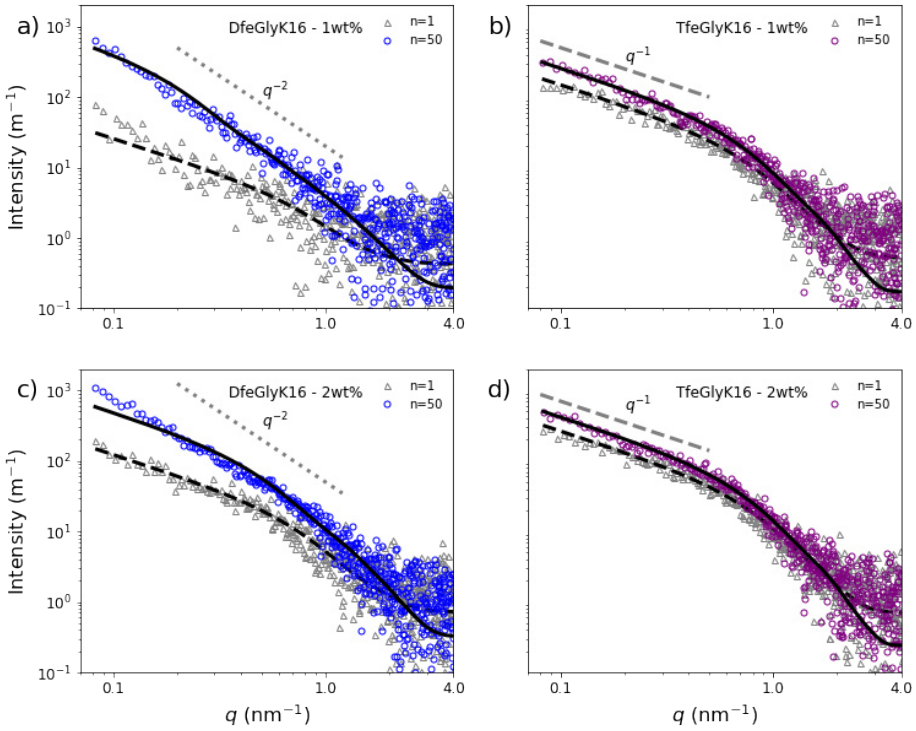

Figure S112: SAXS data and model curves for samples of **DfeGlyK16** and **TfeGlyK16** (symbols and lines, respectively). Data were from measurements directly after mixing (data frame n=1) and after about 3000 s (n=50). Scaling of the intensity proportional to q^{-2} (panel a and c) and proportional to q^{-2} (panel b and d) are indicted as straight lines.

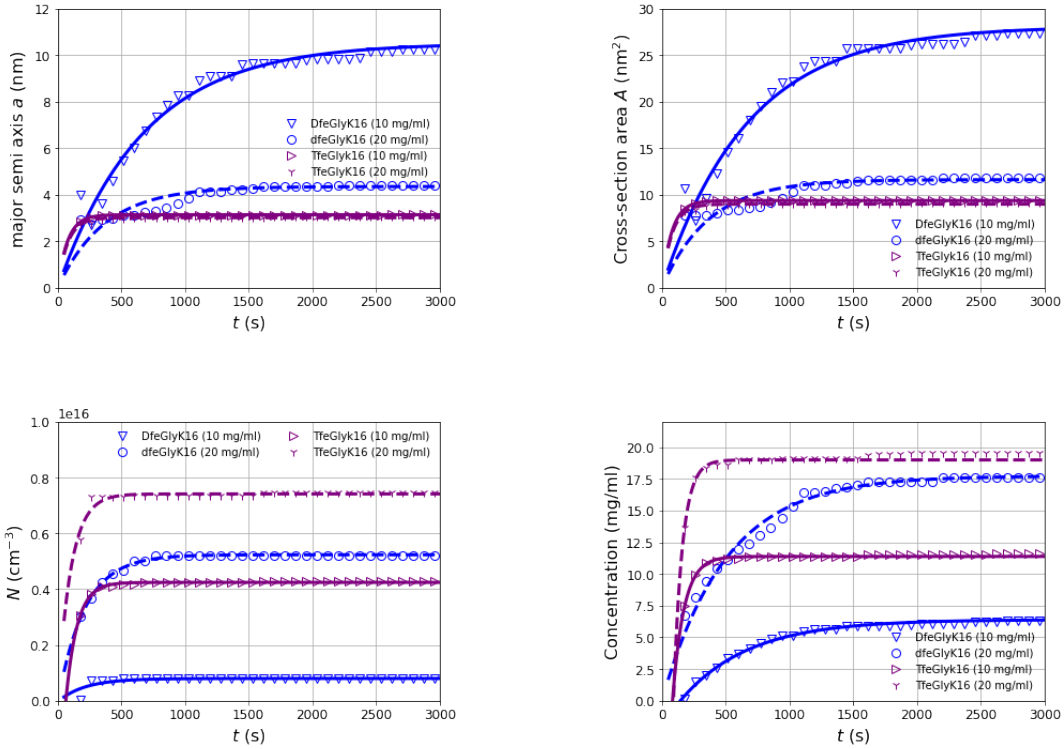

Figure S113: Kinetics of fibril formation. (top) Changes of the major semi axis and the cross-section area. (bottom) Number density and weight concentration of the fibrils.

14. References

1. V. A. Soloshonok, T. K. Ellis, H. Ueki and T. Ono, *Journal of the American Chemical Society*, 2009, **131**, 7208-7209.
2. A. E. Sorochinsky, H. Ueki, J. L. Aceña, T. K. Ellis, H. Moriwaki, T. Sato and V. A. Soloshonok, *Journal of Fluorine Chemistry*, 2013, **152**, 114-118.
3. J. Wang, M. Sánchez-Roselló, J. L. Aceña, C. del Pozo, A. E. Sorochinsky, S. Fustero, V. A. Soloshonok and H. Liu, *Chemical Reviews*, 2014, **114**, 2432-2506.
4. S. Zhou, J. Wang, X. Chen, J. L. Aceña, V. A. Soloshonok and H. Liu, 2014, **53**, 7883-7886.
5. Y. Nian, J. Wang, S. Zhou, S. Wang, H. Moriwaki, A. Kawashima, V. A. Soloshonok and H. Liu, 2015, **54**, 12918-12922.
6. T. T. Romoff, A. B. Palmer, N. Mansour, C. J. Creighton, T. Miwa, Y. Ejima, H. Moriwaki and V. A. Soloshonok, *Organic Process Research & Development*, 2017, **21**, 732-739.
7. Y. Nian, J. Wang, H. Moriwaki, V. A. Soloshonok and H. Liu, *Dalton Transactions*, 2017, **46**, 4191-4198.
8. J. Han, R. Takeda, X. Liu, H. Konno, H. Abe, T. Hiramatsu, H. Moriwaki and V. A. Soloshonok, *Molecules (Basel, Switzerland)*, 2019, **24**, 4521.
9. H. Mei, T. Hiramatsu, R. Takeda, H. Moriwaki, H. Abe, J. Han and V. A. Soloshonok, *Organic Process Research & Development*, 2019, **23**, 629-634.
10. J. Bandekar, D. J. Evans, S. Krimm, S. J. Leach, S. Lee, J. R. McQuie, E. Minasian, G. Némethy, M. S. Pottle, H. A. Scheraga, E. R. Stimson and R. W. Woody, *Int J Pept Protein Res*, 1982, **19**, 187-205.
11. J. Leppkes, T. Hohmann and B. Koksch, *Journal of Fluorine Chemistry*, 2020, **232**, 109453.
12. M. Salwiczek, S. Samsonov, T. Vagt, E. Nyakatura, E. Fleige, J. Numata, H. Cölfen, M. T. Pisabarro and B. Koksch, *Chemistry – A European Journal*, 2009, **15**, 7628-7636.
13. N. Hirota, K. Mizuno and Y. Goto, *Journal of molecular biology*, 1998, **275**, 365-378.
14. A. I. Arunkumar, T. K. Kumar, T. Sivaraman and C. Yu, *Int J Biol Macromol*, 1997, **21**, 299-305.
15. R. Gambaretto, L. Tonin, C. Di Bello and M. Dettin, 2008, **89**, 906-915.
16. G. D'Auria, M. Vacatello, L. Falcigno, L. Paduano, G. Mangiapia, L. Calvanese, R. Gambaretto, M. Dettin and L. Paolillo, *Journal of Peptide Science*, 2009, **15**, 210-219.
17. C. L. Shen and R. M. Murphy, *Biophysical journal*, 1995, **69**, 640-651.
18. I. M. Geisler and J. P. Schneider, *Advanced Functional Materials*, 2012, **22**, 529-537.
19. U. I. M. Gerling, M. Salwiczek, C. D. Cadicamo, H. Erdbrink, C. Czekelius, S. L. Grage, P. Wadhwani, A. S. Ulrich, M. Behrends, G. Haufe and B. Koksch, *Chemical Science*, 2014, **5**, 819-830.
20. K. S. Hellmund, B. von Lospichl, C. Böttcher, K. Ludwig, U. Keiderling, L. Noirez, A. Weiß, D. J. Mikolajczak, M. Gradzielski and B. Koksch, *Peptide Science*, 2021, **113**, e24201.
21. V. Lattanzi, I. Andre, U. Gasser, M. Dubackic, U. Olsson and S. Linse, *Proceedings of the National Academy of Sciences of the United States of America*, 2021, **118**.
22. A. Guinier and G. Fournet, *Small-Angle Scattering of X-Rays*, John Wiley & Sons, Inc., New York, 1955.
23. O. Glatter, *Scattering Methods and their Application in Colloid and Interface Science*, Elsevier, Amsterdam, 2018.
24. S. Chowdhary, J. Moschner, D. J. Mikolajczak, M. Becker, A. F. Thünemann, C. Kästner, D. Klemczak, A.-K. Stegemann, C. Böttcher, P. Metrangolo, R. R. Netz and B. Koksch, *ChemBioChem*, 2020, **21**, 3544-3554.
25. J. Schmitt, V. Calabrese, M. A. da Silva, S. Lindhoud, V. Alfredsson, J. L. Scott and K. J. Edler, *Physical Chemistry Chemical Physics*, 2018, **20**, 16012-16020.

26. D. Orthaber, A. Bergmann and O. Glatter, *Journal of Applied Crystallography*, 2000, **33**, 218-225.